Experimental study of complex pipe flows

by

Sohrab Sattarzadeh Shirvan

June 2011
Technical Reports from
Royal Institute of Technology
KTH Mechanics
SE-100 44 Stockholm, Sweden

Sohrab Sattarzadeh Shirvan, **Experimental study of complex pipe flows**
Linné Flow Centre, KTH Mechanics, Royal Institute of Technology
SE–100 44 Stockholm, Sweden

Abstract

Turbulent pipe flows are prevalent in industrial applications. Despite a large body of experimental and more recently numerical investigations there are still unresolved fundamental issues. Among those are the scaling of the mean velocity profile or the question whether the near-wall peak in the variance profile is Reynolds number invariant. The situation is even more vague when it comes to non-canonical turbulent pipe flows, such as flows in bend pipe sections or swirling flows. One reason for the controversial views is due to insufficient insight into the limitations of state-of-the art measurement techniques employed in these studies. Pitot tube and hot-wire measurements have been employed for almost a century now, however, there is a renewed interest in their calibration at low velocities, their spatial and temporal resolution as well as their correction schemes.

In the present thesis hot-wire measurements were performed in swirling and non-swirling turbulent flows through straight and 90° pipe bends in a Reynolds number range from 13000 – 34000 by keeping the viscous scaled wire length small and constant thereby avoiding ambiguity between Reynolds number and spatial resolution effects. Additionally, spatial resolution effects were studied by repeating measurements at the same Reynolds number with four different wire length. Besides the non-swirling pipe flows, various swirl strength in the range S =0–0.5 have been imparted on the fully developed turbulent flow pipe to study the effect of rotation on the flow in straight and bend pipe flows. Special attention was also paid to the calibration of hot-wire probes at low velocities. In particular a number of cylinder wake measurements were performed to expand the classical vortex shedding calibration of hot-wire probes.

Results indicate that the near-wall peak of the streamwise variance profile increases with Reynolds number, when keeping the wire length constants in viscous units; a result that confirms similar findings in channel and turbulent boundary layer flows, but contradicts recent findings from the Princeton Superpipe.

A superposition of weak degree of swirl up to S=0.1 has been found to have negligible effects on the statistical quantities, while with further increase the flow approaches its laminar profile, i.e. a higher mean velocity and a lower turbulence intensity in the central region of the pipe. In bend pipe flows the addition of swirl has a stabilizing effect on the flow after the bend, i.e. a shorter development length is needed to recover from the bend.

Descriptors: Hot-wire measurements, Fully developed turbulent pipe flow, Flow through circular bend pipes, Swirling flows through circular pipes and bend pipes, Low velocity hot-wire calibration.

Contents

CHAPTER 1

Introduction

1.1. Background and motivation

Pipe flows can be encountered in a variety of technical application, of which two examples are given here. The transport of natural gases and for instance the Yamal to Europe pipe line which is 4200 km long consisting of pipe segments of a diameter of 1.42 m. This particular pipe lines transfers 33 billion cubic meters of natural gas per year. In addition, more complex geometries involving bends and swirl can for instance be encountered in exhaust manifolds, which are studied intensively at *KTH Mechanics* within CICERO. The work has been initiated to experimentally study turbulent pipe flows in straight and 90 pipe bends. In particular, we were interested in Reynolds number and swirl number effects on the flow evolution. However, once started, we got dragged into two new topics. One of these topics is the near-wall region in fully developed turbulent pipe flows, due to some very recent controversies which have attracted us. Another topic, which arose from this new side-project is related to the fact that near-wall measurements in our Reynolds number range made it necessary to look at low velocity calibration issues for hot-wires. These two side-projects actually took most of the time and will therefore also be presented in thesis.

1.2. Layout of the thesis

The present study is divided into different parts that are discussed in the following chapters of this thesis report. The layout of these chapters are shortly presented in this section. In chapter 2, the theoretical background of the needed quantities in turbulence (i.e. statistical properties) and pipe flow (wall-bounded shear flows) investigations is stated. Chapter 3 is dedicated to the review of the previous studies performed on the main subject of the present study that are flow in curved circular-pipe, swirling flow in pipes in straight pipes, and swirling flow in curved circular-pipes. The experimental setup and the measurement techniques are presented in chapter 4. Also, the second excursus of the thesis, low velocity hot-wire calibration, is concluded as a calibration method in the related section of this chapter. Chapter 5 and 6 are presenting the results of the conducted measurements for straight and bend turbulent pipe flows respectively. In addition, the results of the fully developed straight turbulent pipe flow in viscous inner-scaling are included in appendix A.

CHAPTER 2

Theoretical background

2.1. Turbulence

Most flows that exist in nature or are utilized in applied sciences and engineering are turbulent. A turbulent flow is a time dependent chaotic three dimensional flow which can be divided into a mean and fluctuating part. British fluid dynamist Osborne Reynolds (1842-1912) studied the transition conditions of laminar to turbulent flow in pipes, and the experiments he did led to formation of the famous dimensionless fluid mechanical *Reynolds number*, *Re*. The Reynolds number is defined as the ratio between inertial and viscous forces in the flow, and is generally written as

$$Re = \frac{UL}{\nu}\,, \tag{2.1}$$

where U and L are characteristic velocity and length scales respectively, and ν is the kinematic viscosity of the fluid. According to Reynold's investigations, there exists a critical Reynolds number, depending on the conditions of each particular setup, above which the flow becomes turbulent.

In turbulent flows the inertia forces dominate the flow behavior compared to viscous forces. Turbulent flow consists of different length scale eddies. Large scale eddies are associated with the velocity and length scales of the order of mean flow and geometry of the facility respectively that are characterized by the particular flow setup, and have the most turbulent kinetic energy. The large eddies take the energy from the mean flow and transfer it to smaller eddies by the means of breaking down into smaller vortices. This transferring of energy, *energy cascade*, goes on until the length scale of the eddies are small enough for the viscous dissipation. Small eddies when not affected by the boundary conditions of the particular setup have a universal and isotropic character. The range between large energy bearing eddies and small eddies (dissipative range) which is governed only by inertial forces is called inertial subrange, where the transfer of energy from large to small eddies takes place. Production of energy is mainly taking place in the energy containing range (large eddies), and the dissipation of energy happens in dissipative range (small viscous eddies). The main role of viscous forces is to dissipate turbulent kinetic energy into heat.

2.2. Statistical Principles

In order to study turbulent flows, instantaneous velocity of the fluid is divided into mean and fluctuating parts, $u = U + u'$ (Reynolds decomposition), and due to irregularity of the fluctuating part, statistical analysis should be used in order to find properties of the flow.[1]

2.2.1. *Probability Density Function (PDF)*

In order to get the concept of *probability density function, PDF*, thoroughly, the *cumulative distribution function*, $F_u(\mathbf{U})$, has to be introduced first. Having a random variable $u(i)$, the cumulative distribution function is defined as the probability of $u(i)$ satisfying $u(i) \leq \mathbf{U}$ at each point i when $\mathbf{U}$ is an invariant value, i.e.

$$F_u(\mathbf{U}) = P[u(i) \leq \mathbf{U}]\,. \tag{2.2}$$

One can easily comprehend that $F(-\infty) = 0$ and $F(+\infty) = 1$ for any set of random variables. $\mathbf{U}$ can vary between $-\infty$ and $+\infty$ and $F(\mathbf{U})$ can form a diagram which is related to the PDF.

The probability density function (PDF), $f(\mathbf{U})$, is related to the cumulative distribution function, $F(\mathbf{U})$, and is defined as

$$f(\mathbf{U}) = \lim_{\triangle\mathbf{U}\to 0}\left\{\frac{P[\mathbf{U} \leq u(i) \leq \mathbf{U} + \triangle\mathbf{U}]}{\triangle\mathbf{U}}\right\}. \tag{2.3}$$

Following perceptions can be derived from the definition,

$$f(\mathbf{U}) \geq 0\,, \tag{2.4}$$

$$\int_{-\infty}^{+\infty} f(\mathbf{U})\,\mathrm{d}\mathbf{U} = 1\,, \tag{2.5}$$

$$F(\mathbf{U}) = \int_{-\infty}^{\mathbf{U}} f(\zeta)\,\mathrm{d}\zeta\,, \tag{2.6}$$

$$\frac{\mathrm{d}F(\mathbf{U})}{\mathrm{d}\mathbf{U}} = f(\mathbf{U})\,. \tag{2.7}$$

For the case of turbulent flow studies, random variable $u(i)$ is $u(t)$, where $u(t)$ is the time series of the instantaneous velocity at a point in the flow. Also as the probability density function, $f(\mathbf{U})$, is only non-zero for $f(\mathbf{U})$ between $u(t)_{min}$ and $u(t)_{max}$, $\mathbf{U}$ can be denoted as $u(t)$ since $f(\mathbf{U})$ is demonstrating the

[1] The contents of the following section is implied from text books of Pope (2000) and Kundu & Cohen (2004).

probability density function of $u(t)$ for all the values bound between $u(t)_{min}$ and $u(t)_{max}$. For simplicity, $u(t)$ is denoted as u here after.

2.2.2. *Moments of the fluctuations*

With a given PDF the *mean* value, *first moment* of fluctuations, of the velocity time series u is obtained as

$$U = u_{mean} =< u >= \int u f(u)\,\mathrm{d}u\,, \tag{2.8}$$

where $< X(i) >$ is the mean-average value of the random variable $X(i)$. Now fluctuations can be defined as

$$u' = u - U\,. \tag{2.9}$$

The *variance* is the *second moment* of the fluctuations

$$\sigma_u^2 =< u'^2 >= \int (u-U)^2 f(u)\,\mathrm{d}u\,. \tag{2.10}$$

The *standard deviation*, σ_u, or *root mean square* value of fluctuations, u_{rms}, is obtained by taking the root mean square of the variance as

$$\sigma_u = u_{rms} = \sqrt{< u'^2 >}\,. \tag{2.11}$$

The *third moment* of fluctuations of u is the *skewness* of the probability density function and is obtained as

$$S = \frac{< u'^3 >}{\sigma_u^3} = \frac{\int (u-U)^3 f(u)\,\mathrm{d}u}{\sigma_u^3}\,, \tag{2.12}$$

and similarly, the *flatness* or *kurtosis* of the probability density function is obtained from the *forth moment* of the fluctuations as

$$F = \frac{< u'^4 >}{\sigma_u^4} = \frac{\int (u-U)^4 f(u)\,\mathrm{d}u}{\sigma_u^4}\,. \tag{2.13}$$

In order to further describe the aforementioned definitions, a velocity time series as well as statistical values of turbulence measurements of turbulent pipe flow is depicted in figure 2.1 for a point near the pipe wall. The skewness is a measure of asymmetry of the probability density function, and this concept is apparent in figure 2.1. The value of skewness for a normal distribution (e.g. *Gaussian* distribution) is equal to zero which shows the symmetry of the distribution. But for the distribution in figure 2.1 the skewness is not equal to zero since it is not symmetric, and has a positive value. The positive value shows that the tale of the PDF is toward the higher velocities. The kurtosis or flatness is a measure of the peakedness of the distributed amplitude of the

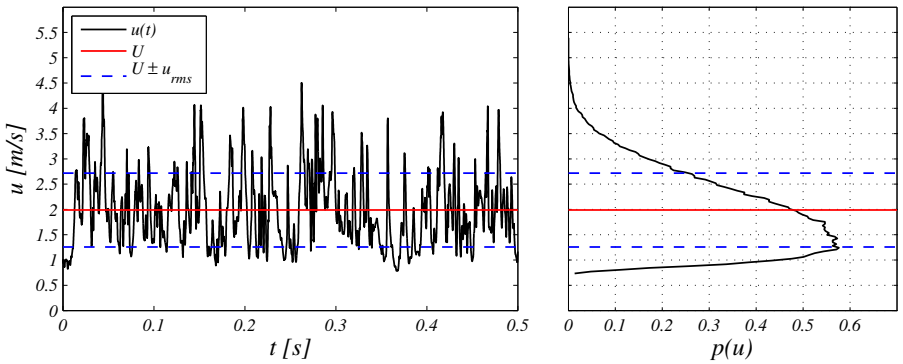

FIGURE 2.1. The distribution of velocity with respect to time for turbulent pipe flow hot-wire measurements at near the pipe wall position, $r/R = 0.992$, as well as U and u_{rms} in (a), and the probability distribution function of the same time series in (b) are presented.

time series here. This value is 3 for a *Gaussian* distribution. For the depicted time series in figure 2.1, the mean and rms values of velocity are 1.93 and 0.70 while the skewness and flatness are 0.70 and 3.09 respectively.

2.2.3. *Correlation*

A phenomenon is called a *random process* when the random variable of interest X is a function of time, e.g, time series of the velocity field $u(t)$ of a turbulent flow. If different samples of time series are in hand for the repetition of same experiment, the PDF of the values in different samples for each specified time in the time series (i.e., the one-time PDFs) completely characterizes $u(t)$ at that point of time. But these PDFs of different points in the time series do not give any joint information about $u(t)$ at two or more different times. On the other hand, different random processes can have the same probability density function although they represent different phenomena. This illustrates the fact that aiming to fully analyze a random process, the PDF of $u(t)$ does not give the complete information about the characteristics of the phenomenon.

If the process is *statistically stationary* a simplification can be used to overcome the mentioned problem and analyze the characteristics of the random process completely. A *statistically stationary* process is a process in which the statistical properties (e.g., u_{mean}, u_{rms}, etc.) are independent of time. In most turbulent flows, after passing the transient state, the statistical properties of the flow do not vary with time, even though the flow variables are strongly

time dependent (e.g., $u(t)$).

The *auto-covariance* for the statistically stationary processes is the simplest considered multi-time statistical property that gives additional information about the process with respect to PDF which is defined as

$$R(\tau) \equiv < u'(t)u'(t+\tau) > , \tag{2.14}$$

and could be normalized to *autocorrelation* function as

$$\rho(\tau) \equiv < u'(t)u'(t+\tau) > / < u'(t)^2 > , \tag{2.15}$$

where τ here is the time lag to demonstrate the time difference. Similar to U and u_{rms}, $R(\tau)$ and $\rho(\tau)$ are independent of time. The correlation between the random variable at time t and $t+\tau$ is shown by autocorrelation. Hence,

$$\rho(0) = 1 , \tag{2.16}$$

$$\mid \rho(\tau) \mid \leq 1 . \tag{2.17}$$

Knowing that $\rho(\tau)$ is independent of time t, one obtains that $\rho(\tau)$ is an even function by putting $t' = t + \tau$,

$$\rho(\tau) = < u'(t'-\tau)u'(t') > / < u'^2 > = \rho(-\tau) . \tag{2.18}$$

Figure 2.2 shows the streamwise autocorrelation function, R_{uu}, diagram for the time series of streamwise velocity which has been shown in figure 2.1. As can be observed from figure 2.2, for turbulent flows, the correlation is expected to diminish rapidly as the lag time τ increases. Therefore, a time scale can be defined and considered as the memory of the random variable $u(t)$ such as

$$\Lambda_t \equiv \int_0^\infty \rho(\tau)\, \mathrm{d}\tau , \tag{2.19}$$

which is the so-called *integral timescale* of the process. For the case of figure 2.2, the integral timescale is around 3 ms.

In order to analyze the spatial structure, the covariance function could be written as

$$R_{ii}(r) \equiv < u_i'(x_i,t)u_i'(x_i+r,t) > . \tag{2.20}$$

This could be normalized to *spatial autocorrelation* as

$$\rho_{ii}(r) \equiv < u_i'(x_i,t)u_i'(x_i+r,t) > / < u_i'^2 > , \tag{2.21}$$

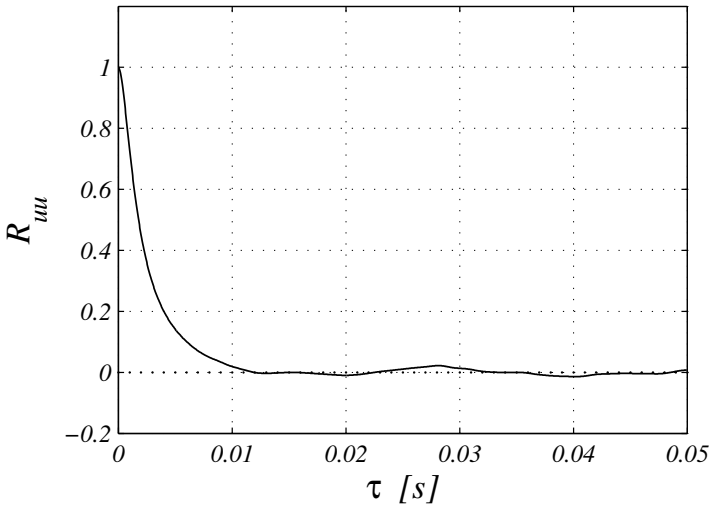

FIGURE 2.2. Autocorrelation for turbulent pipe flow hot-wire measurements at near the pipe wall position, $r/R = 0.992$

where r is the distance between two point of flow, and the i subscript refers to the direction of the coordinate system. In the written form here, the function is calculating the spatial autocorrelation (i.e. the correlation of a velocity component with itself at a constant time and different spatial positions). The correlation between different components of velocity (e.g. streamwise and spanwise) can be calculated similarly. If the distance vector r is parallel to u_i the autocorrelation function is *longitudinal* and if it is perpendicular to u_i it is *transverse*. The *integral length scale* can then be determined as

$$\Lambda \equiv \int_0^\infty \rho_{ii}(r,t)\,\mathrm{d}r\,. \tag{2.22}$$

According to equations (2.19) and (2.22), the integral should be taken over an infinite domain while the obtained data from experimental or numerical investigation is finite. O'Neill *et al.* (2004) compared different methods to overcome this problem among which there exists two methods that is acceptable each in its own condition. If the autocorrelation function has a negative region, the integrate can be taken to the minimum value of autocorrelation. In the case that the autocorrelation function does not have a negative region or minimum the integrate should be taken to the first zero value of the autocorrelation function. Integrating over the whole domain or to the value where the autocorrelation function falls to $(1/e)$ have disadvantages and are expected to overestimate and underestimate the integral time and length scales, respectively.

2.2.4. *Power Spectral Density, PSD*

If a function reduces to zero sufficiently rapid toward infinity, a *Fourier transform* can be defined for it. The auto-covariance function decays to zero fast enough so a Furier transform can be denoted for it as

$$E(\omega) \equiv \frac{1}{2\pi} \int_{-\infty}^{\infty} e^{-i\omega\tau} R(\tau)\, \mathrm{d}\tau\,, \tag{2.23}$$

which gives the *power spectral density* (PSD or spectrum) of the velocity fluctuations, and consequently to have a *Fourier transform pair* auto-covariane can be written as

$$R(\tau) \equiv \int_{-\infty}^{\infty} e^{i\omega\tau} E(\omega)\, \mathrm{d}\omega\,, \tag{2.24}$$

where ω is the angular frequency, i.e. $\omega = 2\pi f$. For $\tau = 0$ equation (2.24) gives

$$< u^{'2} >= \int_{-\infty}^{\infty} E(\omega)\, \mathrm{d}\omega\,. \tag{2.25}$$

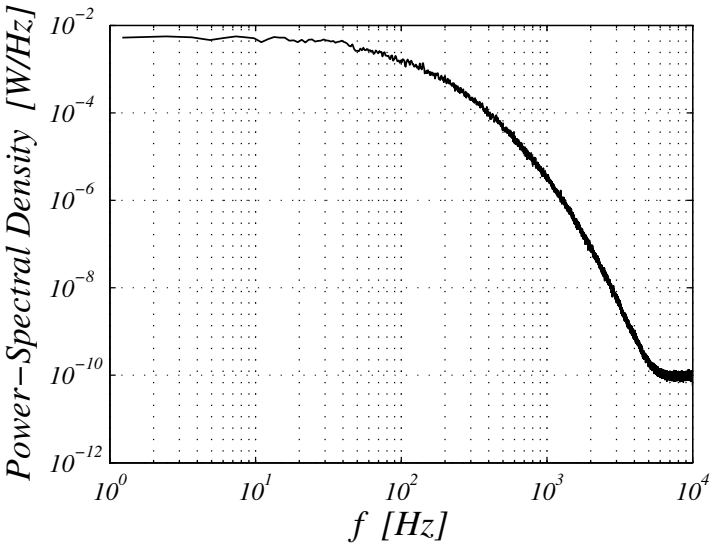

FIGURE 2.3. Smoothed Power-Spectral Density function by averaging overlapped spectra for discrete blocks using *Welch's* method.

It can be interpreted from equation (2.25) that $E(\omega)\,\mathrm{d}\omega$ is the variance (i.e., energy) in the frequency band $\mathrm{d}\omega$ centered at ω. Therefore, the function $E(\omega)$

is the *energy spectrum* and represents the way energy is distributed as a function of frequency ω. For $\omega = 0$ equation (2.23) gives

$$E(0) = \frac{1}{2\pi}\int_{-\infty}^{\infty} R(\tau)\,\mathrm{d}\tau = \frac{< u^{'2} >}{\pi}\int_{0}^{\infty} \rho(\tau)\,\mathrm{d}\tau = \frac{< u^{'2} > \Lambda_t}{\pi}\,. \qquad (2.26)$$

which is another definition for integral timescale, Λ_t.

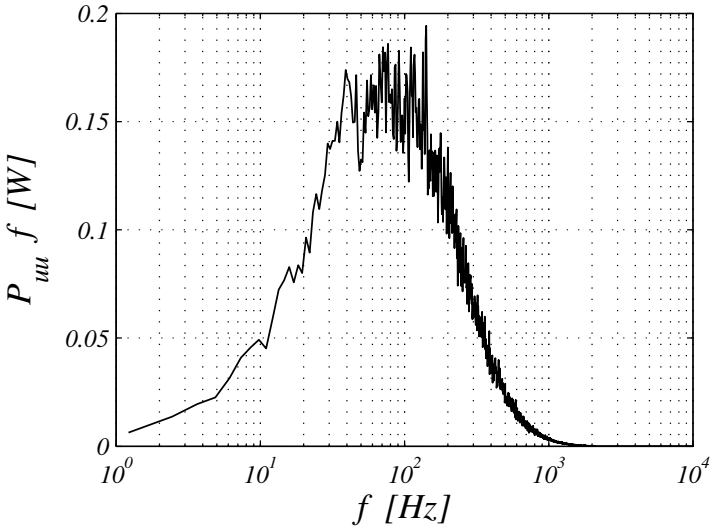

FIGURE 2.4. Pre-multiplied spectra with frequency for streamwise velocity fluctuations of turbulent pipe flow.

In figure 2.3, the power spectral density of the same case as figure 2.1 is presented. Since the error in the spectra is of the order of one, averaging overlapped spectra for discrete blocks is used to smooth the estimate for the power spectral density function (so-called *Welch's averages*). In order to observe the most energetic frequencies, the power spectral density function can be multiplied with the frequency, f, as it is illustrated in figure 2.4. The power spectral density is denoted as P_{uu} in figure 2.4 since it is for streamwise velocity fluctuations. The high peaks in the pre-multiplied spectra diagram illustrate the frequencies which have the highest energy. This information cannot be taken from the previous statistical properties.

2.3. Pipe flow

2.3.1. *Wall-bounded shear flows (Straight pipe flows)*

In order to analyze the axisymmetric fully developed turbulent pipe flow, Cartesian coordinates is utilized while x direction is aligned with the streamwise

direction of the pipe flow, and the radial, normal to pipe wall, direction of the pipe flow is denoted with y direction. The streamwise and normal to wall velocity components are respectively denoted with u and v. The streamwise Reynolds average Navier-Stokes (RANS) equation for fully developed turbulent pipe flow in Cartesian coordinates can then be simplified as

$$0 = -\frac{\partial}{\partial x}P + \frac{\partial}{\partial y}\tau\,, \tag{2.27}$$

in which the mean total shear stress, τ, for turbulent flow is

$$\tau = -\rho < u'v' > +\mu\frac{\partial U}{\partial y}\,, \tag{2.28}$$

The RANS equation for normal to wall direction gives

$$P + \rho < v'v' >= P_{wall}\,, \tag{2.29}$$

which after taking the derivative in streamwise direction, considering constant $\rho < v'v' >$ in x direction due to fully developed flow, gives

$$\frac{\partial P}{\partial x} + \frac{\partial \rho < v'v' >}{\partial x} = \frac{\partial P_{wall}}{\partial x} = \frac{\mathrm{d}P_{wall}}{\mathrm{d}x}\,, \tag{2.30}$$

where $\frac{\mathrm{d}P_{wall}}{\mathrm{d}x}$ is a constant that can be substitute instead of $\frac{\partial P}{\partial x}$ in equation (2.27). Substituting this in equation (2.27) and integrating in y direction from 0 to δ, one can find τ_{wall} as a function of wall pressure gradient in streamwise direction, $\frac{\mathrm{d}P_{wall}}{\mathrm{d}x}$, as

$$\tau_{wall} = -\delta\frac{\mathrm{d}P_{wall}}{\mathrm{d}x}\,, \tag{2.31}$$

in which δ is the pipe radius, R. One can find the relation between the turbulent mean total shear stress, τ, and wall shear stress, τ_{wall}, using equation (2.31) and integrating equation (2.27) again in y direction this time from 0 to an arbitrary y as

$$\tau = \tau_{wall}(1 - \frac{y}{R})\,, \tag{2.32}$$

which states a linear distribution of τ in y direction normal to wall, and also the assumption that, for $y << \delta$, the turbulent mean total shear stress is constant and equal to wall shear stress, which mainly is the viscous shear stress since the *Reynolds stress*, $- < u'v' >$, goes to zero in the vicinity of the wall. Figure 2.5 illustrates the behavior of viscous shear stress as well as Reynolds stress along

the radial direction of a turbulent pipe flow according to the direct numerical simulation (DNS) results of Wu & Moin (2008).

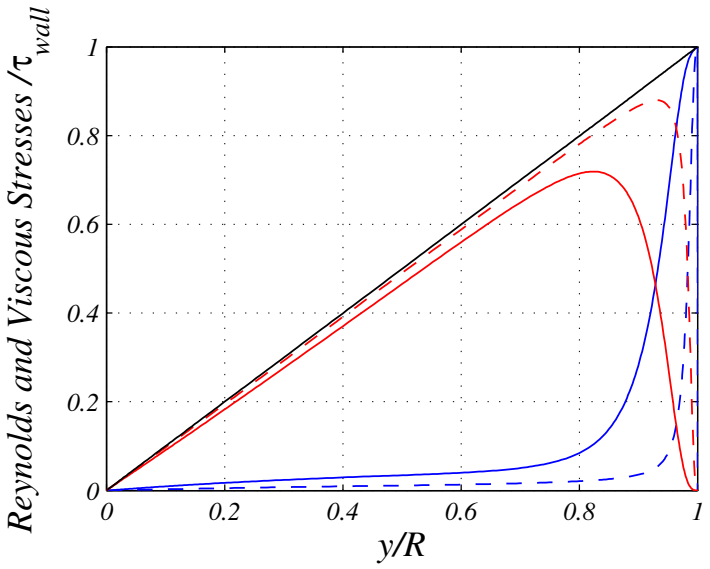

FIGURE 2.5. Reynolds and viscous shear stresses normalized by τ_{wall} along pipe radial direction. Color solid and dashed lines are representing $R^+ = 180$ and $R^+ = 680$, and the normalized Reynolds and viscous shear stresses are illustrated in red and blue respectively while the black solid line is normalized τ_{wall}; DNS data of Wu & Moin (2008).

Considering τ_{wall} as a constant term, according to equation (2.31) and since $\frac{\mathrm{d}P_{wall}}{\mathrm{d}x}$ is constant, one can define friction velocity, u_τ, and viscous length scale, ℓ_*, according to τ_{wall} as

$$u_\tau = \sqrt{\frac{\tau_{wall}}{\rho}}\,, \tag{2.33}$$

$$\ell_* = \frac{\nu}{u_\tau}\,. \tag{2.34}$$

The friction factor, λ, is then defined as

$$\lambda = \frac{4\tau_{wall}}{\frac{1}{2}\rho U^2} = 8\big(\frac{u_\tau}{U}\big)^2\,. \tag{2.35}$$

These scales play an important role in understanding different characteristics

of the flow such as velocity profile in different regions of the flow. One can also define the friction Reynolds number, Re_τ, as

$$Re_\tau = \frac{u_\tau \delta}{\nu} = \frac{R}{\ell_*} = R^+ \,, \tag{2.36}$$

by introducing u_τ and δ as characteristic velocity length scale respectively to equation (2.1). The friction Reynolds number is the ratio between the large (outer), δ, and small (inner), ℓ_*, length scales, and is equal to the so-called von Kármán number, δ^+.

Due to different characteristics of the flow in different regions, a composite profile for mean velocity of turbulent pipe flow can be used. This composite mean velocity profile mainly consist of the inner and outer regions and an overlap region which connects them. Due to near wall conditions, the inner region characteristics are only dependent on ν, y and u_τ. Introducing the normalized distance from the wall as $y^+ = y/\ell_*$, and the normalized velocity $U^+ = U/u_\tau$, for $y^+/\delta^+ << 1$,near wall region, the so-called law of the wall reported by Prandtl (1925) can then be used,

$$U^+ = \phi_1(y^+) \,. \tag{2.37}$$

The distance from the wall is compared and normalized by the outer length scale for the outer region which in the case of pipe flow is the pipe radius, $y/R = \eta$, which would then be of the order of 1. As reported by von Kárman (1931), the so-called velocity defect law can be used to describe the deviations from the centerline, $U^+_{cl} - U^+ = (U_{cl} - U)/u_\tau$, in the outer region,

$$U^+_{cl} - U^+ = \psi_1(\eta) \,, \tag{2.38}$$

where the centerline velocity, U_{cl}, is the mean velocity of the flow at the pipe centerline. The slopes of the profiles of the law of the wall for $y^+ \gg 1$ and the velocity defect law for $\eta \ll 1$ should agree in the so-called overlap region and the profiles should overlap for $\ell_* \ll y \ll \delta$ as Millikan (1938) reported,

$$y^+ \frac{\mathrm{d}\phi_1(y^+)}{\mathrm{d}y^+} = \eta \frac{\mathrm{d}\psi_1(\eta)}{\mathrm{d}\eta} = \frac{1}{\kappa} = constant \,. \tag{2.39}$$

Considering the first and second sentences of equation (2.39) to be only functions of y^+ and η respectively, they should both be equal to a constant which is the inverse of the so-called von Kármán constant, κ. Solving the equations separately gives the logarithmic velocity profiles for the law of the wall as

$$U^+ = \frac{1}{\kappa} \ln y^+ + B \,, \tag{2.40}$$

and the velocity defect law as

$$U_{cl}^+ - U^+ = -\frac{1}{\kappa} \ln \eta + C \,. \tag{2.41}$$

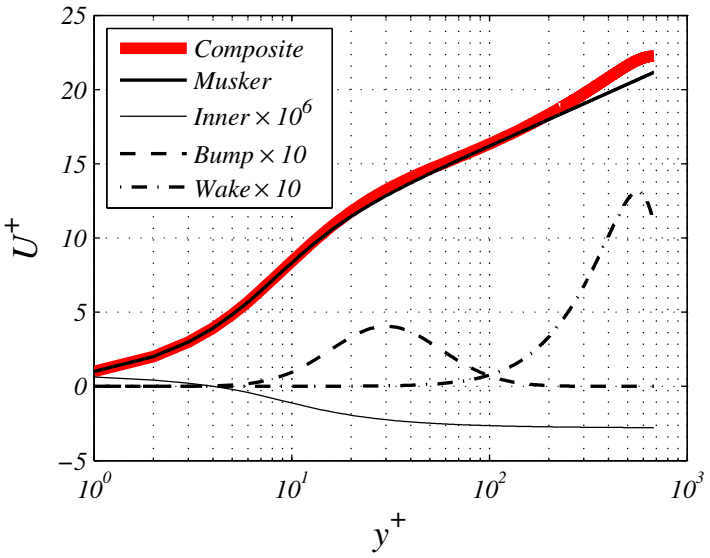

FIGURE 2.6. Composite profile of mean velocity in inner scaling as introduced by Nagib & Chauhan (2008)

According to Nagib & Chauhan (2008), the composite velocity profile can be considered as the summation of different profiles that each of them represents a characteristic of the flow. Figure 2.6 depicts the composite profile of mean velocity in inner scaling for pipe flow as well as its different components introduced by Nagib and Chauhan. For the inner region, they modified Musker (1979) profile which agrees with the linear law of the wall and adjust it self to meet the logarithmic region for higher y^+. At the beginning of the logarithmic profile both DNS and experiment data show an overshoot of U^+ above the log law. The effect of this overshoot was taken into consideration by adding an exponential additive term referred to as bump in figure 2.6. In addition, in the outer part a wake function was introduced to the main Musker profile. Figure 2.7 illustrates different regions of mean velocity profile in inner scaling for pipe flows.

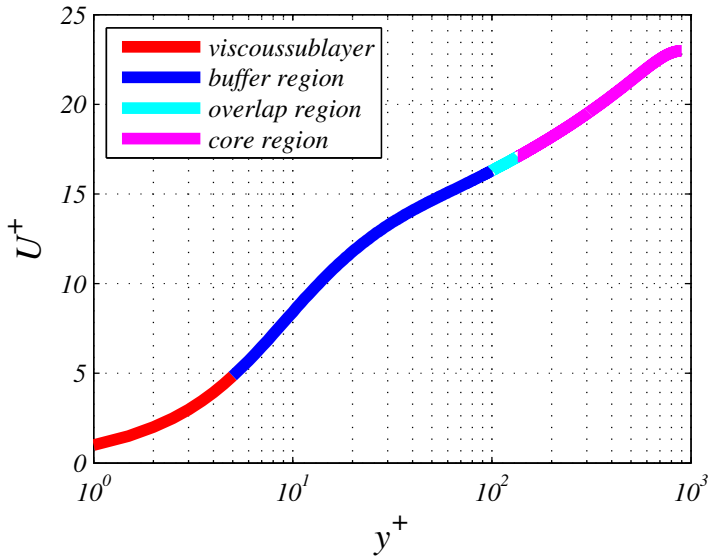

FIGURE 2.7. Typical mean velocity profile in inner scaling, illustrating different regions for $R^+ = 900$.

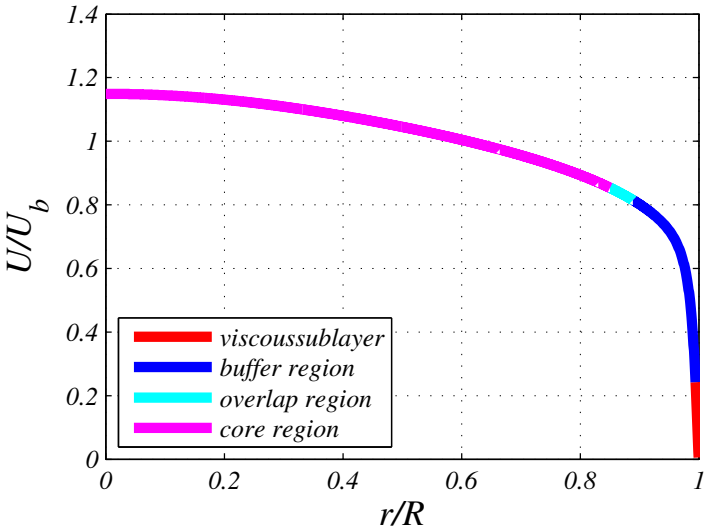

FIGURE 2.8. Composite profile of mean velocity in outer scaling for $R^+ = 900$ as introduced by Nagib & Chauhan (2008)

Knowing the composite velocity profile of the flow in the pipe, one can calculate the bulk velocity, U_b, of the pipe flow. The bulk velocity, U_b, of a pipe flow is the average velocity of the flow crossing the section normal to streamwise direction. The Reynolds number based on the bulk velocity and pipe diameter, Re_D, for pipe flows is then introduced as

$$Re_D = \frac{U_b D}{\nu}\,, \tag{2.42}$$

where D is the pipe diameter. Normalizing U_b with u_τ (i.e. $U_b^+ = U_b/u_\tau$), the relation between the bulk and friction Reynolds numbers, Re_D and Re_τ respectively, would be

$$Re_D = 2U_b^+ Re_\tau\,. \tag{2.43}$$

Figure 2.8 is showing mean velocity profile computed through Nagib & Chauhan (2008) in outer scaling. The mean velocity is normalized by bulk velocity, U_b.

The relation between viscous length scale, ℓ_*, and Re_τ can be derived from equation (2.36) as $\ell_* = R/Re_\tau$. According to this relation, increase in Re_D and hence in Re_τ reduces the viscous length scale, ℓ_*, as it is expected that by increasing the Reynolds number the viscous effects in the flow would reduce. But this reduction is linear as depicted in figure 2.9. The upper side of figure 2.9 shows the trend of changing of Re_τ with respect to Re_D, and the lower side shows the linear reduction in viscous length scales by increasing the Re_τ.

Using the length and the velocity scales of the viscous layer and the outer layer of the flow, one can estimate the viscous and integral time scales. The viscous time scale, t^+, is defined using viscous length and velocity scales, ℓ_* and u_τ respectively, as

$$t^+ = \frac{\ell_*}{u_\tau} = \frac{\nu}{u_\tau^2}\,. \tag{2.44}$$

It is used to normalize the measuring sample time interval, $\Delta t^+ = \Delta t/t^+$, where the sample time interval, Δt, is the inverse of the the sampling frequency, f_s. In order to ensure sufficient temporal resolution for spectral analysis or small scale statistics, Δt^+ should be smaller or at least of the order of 1. In the lower part of figure 2.10, variations in adequate sampling frequency with respect to the friction Reynolds number, Re_τ, is depicted for $\Delta t^+ = 1$. It can be seen that the viscous time scales are decreasing by Re_τ. The integral time scale, Λ_t, can for the case of pipe flow be estimated using the outer length and velocity scales, R and U_{CL}, that are mainly related to the characteristics of the facility setup, as

$$\Lambda_t \cong \frac{R}{U_{cl}}\,. \tag{2.45}$$

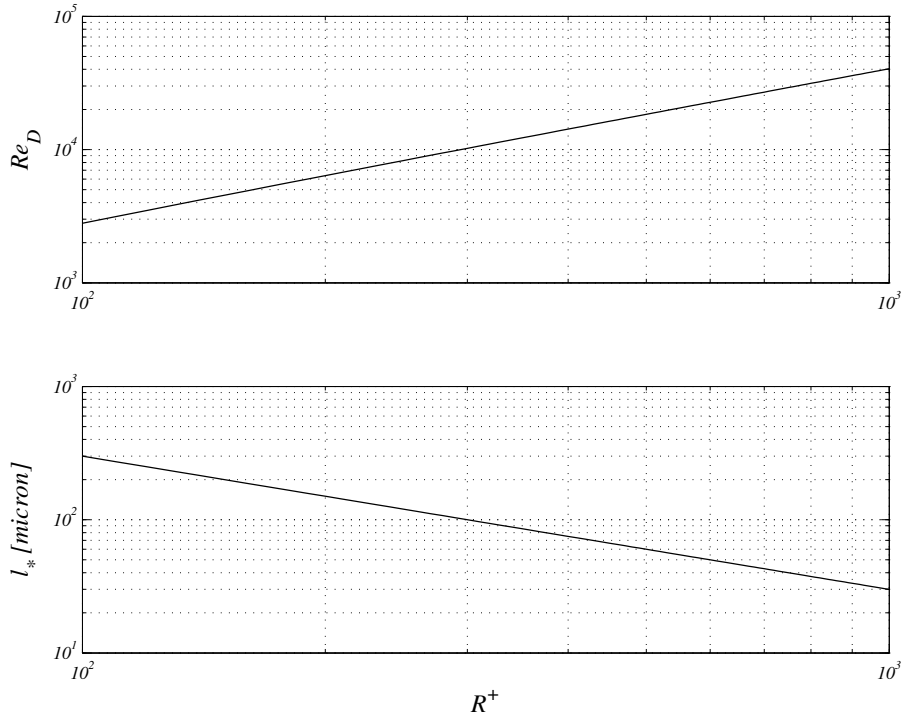

FIGURE 2.9. The Reynolds number based on bulk velocity (upper) and the viscous length scale (lower) with respect to R^+.

The total sampling time, T, is normalized by integral time scale, and the non-diamensional sampling time would then be $TU_{cl}/R = T/\Lambda_t$. The total sampling time affects the accuracy of the turbulent signal averaging. According to Alfredsson & Tillmark (2005), it can be shown that for a certain accuracy (error), ϵ, adequate total sampling time is calculated as

$$\epsilon = \left(2\frac{\Lambda_t}{T}\right)\frac{u_{rms}}{U}\,. \tag{2.46}$$

For a stochastic process, $x = X + x'$, the estimate of the average would be

$$\epsilon^2 = \frac{1}{N}\frac{var(x')}{X^2}\,, \tag{2.47}$$

where N is the total number of independent measurement values. In order

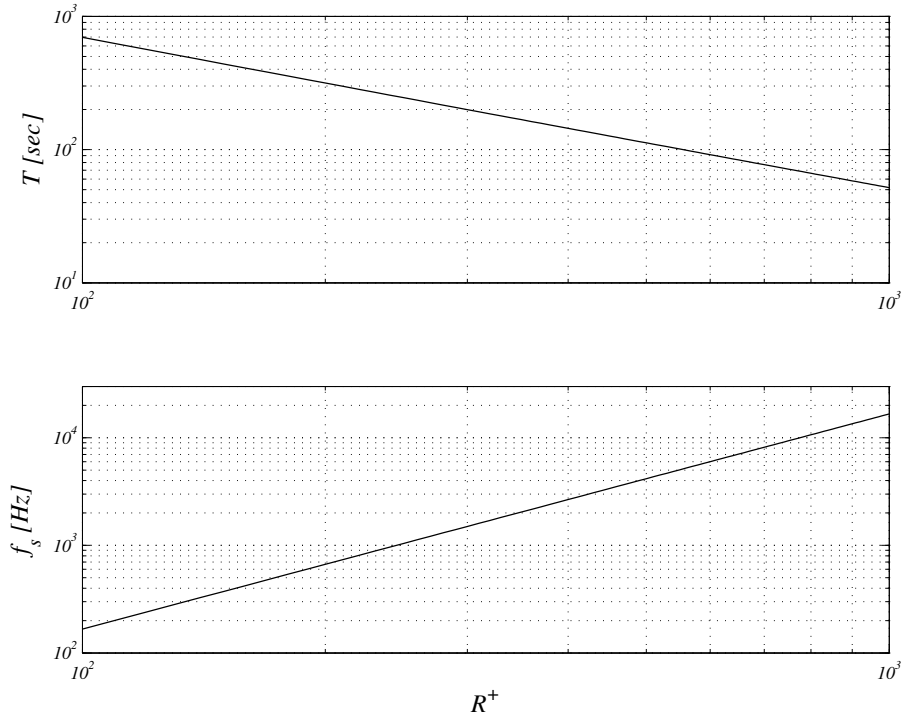

FIGURE 2.10. Required sampling time (upper) and sampling frequency (lower) for acquiring converged statistics with respect to R^+

to calculate the appropriate total sampling time for a certain accuracy in the higher moments, one can replace X with u'^n, and N with $T/2\Lambda_t$ in equation (2.47). As Klewicki & Falco (1990) reported, aiming to get converged statistics for higher order moments, the non-dimensional total sampling time should exceed several thousands. The upper part of figure 2.10 shows the variations of total sampling time with respect to Re_τ considering the non-dimensional total sampling time equal to 10^4.

2.3.2. *Pipe bend*

The flow in a straight pipe has a uniform cross-stream pressure gradient along the pipe, e.g. the cross-stream wall pressure gradient in each side of the pipe are equal. On the other hand, in curved pipe the pressure of the fluid act differently and responds to the centrifugal force applied to the flow by the pipe curvature through the bend. The pressure distribution, therefore, differs in the inner and outer sides of the pipe with respect to the bend, i.e. the flow near the

outer side that has the largest distance from the pipe curvature center gains the highest pressure and pressure decreases by going toward the inner side that is the closest point to the center of bend curvature. Figure 2.11 shows the lon-

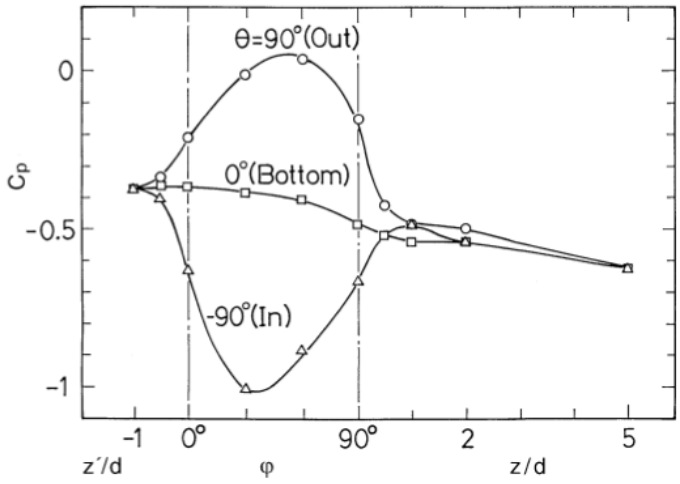

FIGURE 2.11. Longitudinal distribution of wall static pressure

gitudinal wall pressure coefficient distribution of the flow through a 90° bend pipe as well as upstream and downstream of the bend[2]. As depicted in figure 2.11 , in the inlet of the bend the outer side faces a positive local pressure gradient that decelerates the flow, and it is visa versa for the inner side. In the outlet of the bend the conditions are different as the pressure distribution should adjust itself to the uniform cross-stream pressure gradient of the downstream straight tangent pipe. Therefore, the opposite of the inlet of the bend takes place and the flow accelerates in the outer side and decelerates in the inner side. Due to this non-uniform behavior in the cross-stream section of the flow the radial equilibrium is not satisfied in the bend, and according to centrifugal forces the low velocity fluid is directed to the center of the curvature which results in the movement of the high velocity fluid to the outer parts consequently due to continuity. The result of the mentioned mechanism is the forming of the symmetric counter-rotating *Dean vortices* in bent pipes as the secondary flow in the cross-stream section. Affected by the Dean vortices, the region of the high velocity flow is driven from the center of pipe to the inner side at the beginning of the bend, and then to the outer side at the bend out let.

[2]The figure is taken from Sudo *et al.* (1998) in which $z^{'}$ and z are upstream and downstream of the bend longitudinal distances respectively, ϕ and θ are longitudinal and circumferential coordinates, and d is the pipe diameter.

The formation of secondary flow in the transverse section of the flow through curved channels and pipes was first discovered by British applied mathematician and fluid dynamicist Dean (1928). He simplified Navier-Stokes equations seeking solutions independent of longitudinal direction through the curvature of the bend for the flow driven by a pressure gradient in the same longitudinal direction, and introduced dimensionless *Dean number*, De, as a modification to *Reynolds number*, Re, for flow in curved pipes,

$$De = Re.\alpha^{\frac{1}{2}} , \tag{2.48}$$

in which $\alpha = \frac{D}{2R}$ is the pipe to mean-bend-curvature radius ratio, and D and R are pipe diameter and mean-bend-curvature radius respectively.

CHAPTER 3

Review of previous studies

3.1. Flow in curved circular-pipes

The formation of secondary pressure-driven flow in curved pipes and channels that had been studied and solved by British applied mathematician and fluid dynamicist W. R. Dean in 1920's has brought the interest of latter fluid dynamists to study different aspects of this phenomena both in experimentally measuring the fluid characteristics and mathematically or numerically analyzing it, and since Dean's studies included the fluid flow at low Reynolds numbers, there remained a vast area to explore.

Considerable amount of experimental, analytical and numerical studies are in hand regarding the flow over curved circular-pipes and curved ducts, nevertheless the interest of the present study is experimental measurements of the flow over curved circular-pipes which contains the recent measurements of Rowe (1970), Enayet *et al.* (1982), Azzola *et al.* (1986), Anwer *et al.* (1989), Sudo *et al.* (1998, 2000), Kurokawa *et al.* (1998).

Rowe (1970) measured the total pressure and yaw angle relative to the pipe axis of flow, using Pitot tube and claw-type/Conrad yawmeter respectively, in pipe with 180° bend and *S-bend* for Reynolds number 236000 and Dean number 48200. He stated that the highest intensity of the secondary flow is observed at 30° from the inlet of the bend, and in higher degrees of the bend, the formation of total pressure gradient perpendicular to the plane of the bend, which induces a streamwise vorticity with opposite rotational sense compared to the one produced at the inlet of the bend, causes the total secondary flow to reduce and reach a steady value at 90° which indicates little change in longitudinal mean velocities after about 90°, and this mechanism can infer the flow till it gets fully developed in downstream tangent of the bend. On the other hand, in the S-bends (i.e. 45°/45° S-bend in this study) the reversed bend produces vorticity in the same rotational sense as the secondary flow; therefore, the secondary flow intensity increases initially and force the fluids near the wall and in the center of the pipe to interchange completely that explains the large heat trasfer effects in wavy pipes. In addition, as another result the flow become

fully developed in lower values of pipe diameter in downstream tangent compared to U-bends. According to Azzola *et al.* (1986), because of the effects of the Pitot tubes on the flow and experimental uncertainty, the results of Rowe's measurements are not able to characterize the pattern and local reversal of the secondary flow in the symmetric plane of the bend.

Enayet *et al.* (1982) measured the longitudinal mean and fluctuating velocities of laminar and turbulent flow over bend at different degrees as well as upstream and downstream tangents of the bend using laser-doppler velocimetry and water seeded with milk droplets as the working fluid. They stated the conclusion, motivated by different behavior of laminar and turbulent flow, that the strength and characteristics of secondary flow are dependent on the thickness and nature of the inlet boundary layer which obviously is a consequence of Reynolds number. Hence, according to their results, in the case of thin inlet boundary layer (e.g. high Reynolds number) the deflection of a turbulent layer does not exceed 30° from the inlet of the bend and the secondary flow initially appears in the inner part due to inward shift of center high velocity region and then moves outwards by cross-stream pressure-gradient. On the other hand, for the case of laminar flow, the secondary flow forms after 45° in the outer part and remains there. In the case of turbulent flow, the difference in the initial appearance of the high velocity region due to secondary flow between the Rowe's observations and the measurements of Enayet *et al.* (1982) must be the result of different thicknesses in inlet boundary layers while the Dean numbers of the two cases are very similar.

Azzola *et al.* (1986) measured longitudinal and azimuthal mean velocities and turbulence intensities of water over Reynolds numbers 57400 and 110000, with Dean numbers 22100 and 42340 respectively, using laser-doppler velocimetry for 180° bend. The observations confirm the little changes in the mean longitudinal velocity after 90° as was mentioned by Rowe, and in addition to Rowe's results, Azzola *et al.* (1986) state that the circumferential velocity component never become fully-developed during the bend. According to the profiles of the circumferential component of velocity presented by Azzola *et al.* (1986), reversals of the secondary flow are inferred between 90° of the bend and 5 pipe diameter downstream in the tangent straight pipe which is considerably in agreement with the stated mechanism by Rowe of formation of the negative additional streamwise vortices in the rotational sense. They also stated that the turbulence intensities are increasing along the bend because of the additional mean strain which leads to creation of the secondary flow velocity gradients.

Anwer *et al.* (1989) conducted experimental measurements as well as a numerical computation to investigate the behavior of the fully developed turbulent pipe flow along the bend curvature of a circular-sectioned 180° bend pipe.

The experiments were carried out using miniature hot wires to measure three components of mean velocity and the six components of the Reynolds stress. They reported the acceleration of the flow in the outer part of the bend and mentioned that this behavior is a consequence of the accumulation of high velocity flow near the outer wall of the bend. They investigated an increase in all normal stresses across the pipe which begins to disappear as the flow reaches the bend exit. Turbulence energy production and transport were reported to be primarily responsible for this behavior. The extra strain rates created by bend curvature were mentioned to be the reason of formation of this greatly enhanced additional turbulence energy production. Their experimental evidence indicated that complete recovery from bend curvature effects would take more than 18D downstream of the bend exit. They related this with the extra turbulence energy production and inferred that since viscous dissipation is the only way to destroy the additional energy production, recovery takes a long distance. In agreement with Rowe (1970) and numerical computation, the appearance of a second cell in the secondary flow was investigated. This second cell was conjectured to be pressure driven like the Dean vortices. According to their results, the second cell disappears at about one diameter downstream of the bend curve. This result is contrary to the results of Rowe (1970), and also Rowe's finding that a fully developed flow is achieved within the U-bend was rejected.

Sudo *et al.* (1998, 2000) obtained radial as well as longitudinal and circumferential components of mean and fluctuating velocities together with the Renolds stresses, in addition to the studies of Enayet *et al.* (1982) and Azzola *et al.* (1986), for flow in circular-sectioned 90° and 180° bend at Reynolds number 60000 and Dean number 30000. The measurements confirms the initial acceleration of the flow near the inner wall and the formation of a pair of counter rotating vortices known as secondary flow at 30° of the bend. Thus, Reynolds stresses tend to decrease in the inner part with higher mean velocity contours and increase in the outer part. Due to the large velocity gradient, as a result of the greatly distorted primary flow, the turbulence intensity and Reynolds stresses increase in the inner part of the bend between 75° and 90° of the bend while the high velocity region is moving to the outer part by the secondary flow and make tongue shape mean velocity contours in the outer part of the bend. For the case of circular-sectioned 90° bend, Sudo *et al.* (1998), before the bend outlet, the primary flow velocity decreases in the central part of the bend and forms steep variations in velocity profile that leads to complicated distribution of fluctuating velocities. On the other hand, for the case of circular-sectioned 180° bend, Sudo *et al.* (2000), from 90° the high-velocity longitudinal regions are transported to the upper and lower walls of the bend leaving the low-velocity region in the central part. Formation of steep velocity gradients at this station leads to appearance of intensive turbulence, and considerable increase in the

value of Reynolds stresses are observed in the high negative values near the inner wall which diminishes rapidly after the bend outlet. At 1 pipe diameter after the outlet of the 180° bend pipe, the high-velocity region shifts to the outer part again and secondary flow becomes weak, but simultaneously a new pair of vortices shape up at the outer half of the pipe. At downstream of the bend, for both cases secondary flow starts to become weak and the vortices breaks down, but the inflence of the bend remains even at 10 pipe diameter downstream of the bends. However, the deflection of the high-velocity region to the outer wall lasts longer in the 180° bend compared to 90° bend.

Kurokawa *et al.* (1998) used flow visualization to investigate the relaminarization phenomena in curved pipes, and obtained results for secondary flow phenomena at the exit of 90° and 180° bends as well as helically coiled pipes for different Reynolds and Dean numbers. They stated that although the effect of Reynolds number for flow in a straight pipe is destabilizing the flow, in curved pipes secondary flow, that is imposed to the main flow in the cross-section of the pipe due to centrifugal forces, has a stabilizing effect which delay the laminar-turbulent transition. This continues until the inertial forces take over the centrifugal forces and destabilize the laminar flow again. Taking the effect of centrifugal forces into account, the critical Reynolds number for a curved pipe would become higher that that for a straight pipe, and this depends on the curvature ratio or in the other word Dean number. Since the prediction of transition to turbulence criteria and understanding the mechanism is important for flow in the curved pipe problems and heat transfer problems, the authors recommended farther studies on the subject.

3.2. Swirling flow in pipes

The effect of rotation on the turbulent pipe flow has been investigated extensively since it has been always of great interest to fluid dynamists due to its scientific and technological importance. However, since the present study is experimental and contains experimental investigations on turbulent swirling pipe flows, the main attempt was to gather literature about experimental studies performed on this topic.

Three different methods of introducing swirl in turbulent pipe flow have been used throughout the previous studies, and according to the utilized method different resulting flow behaviors were also reported. The methods of generating swirl in pipe flows are rotation methods, tangential injection and passive methods. In the rotation method, the swirl is applied to the flow through solid body rotation of rotating pipe mainly with sufficiently high Reynolds number and also large enough length-to-diameter ratio of the rotating pipe. The swirl number, S, in this method is defined as $S = V_w/U_b$, where V_w is the solid body rotation linear velocity, and U_b is the bulk velocity. According to the

well-defined fully developed outlet conditions that is being produced by using this method as the swirl generating method, the performed results provide an optimal data base for comparison interests with turbulence numeric and simulating models. The tangential injection method on the other hand is capable of providing high swirl numbers that enable the study of reverse flow and along the pipe centerline. In addition, this method can be applied on a variety of geometrical shapes. The passive methods are rather simple methods compared to the others, and are deflecting the flow into curved streamlines by utilizing deflecting or guiding vanes mounted upstream the orifice or nozzle. Similar to tangential injection method, passive method enables the study of reverse flow too, while this is not applicable for rotation methods.

Among the earliest experimental studies on axially rotating pipe flow is the study by White (1964) who performed flow visualization for both laminar and turbulent rotating pipe flows. He illustrated that in the turbulent regime the pressure drop decreased with an increase of the swirl number.

Conducting experiments in a water flow facility, Murakami & Kikuyana (1980) confirmed White's results by reporting that for a pipe length of 100 pipe diameters the pressure loss is governed only by the rate of the rotation. Utilizing a three-hole Pitot tube, they also presented the mean velocity profiles in the streamwise and azimuthal directions. They reported that for fully developed pipe flow condition obtained for pipe length greater than 120 pipe diameter, the velocity profile results are independent of the axial distance from the pipe inlet. The streamwise mean velocity profiles were influenced by swirl number to become less full and tend toward the parabolic shape of a laminar flow as they mentioned. In addition, they illustrated although solid body rotation is not represented by the azimuthal velocity profile, they tend to shape up to nearly parabolic profiles.

Kikuyama *et al.* (1983) followed earlier studies and presented mean streamwise and azimuthal velocity profiles by conducting laser-Doppler velocimetry (LDV) measurements for other experimental setups. Their results along with Reich & Beer (1989) three-hole pressure probe measurements confirmed the parabolic shape of the mean velocity profiles in both streamwise and azimuthal direction as was reported previously.

Using laser-Doppler velocimetry, Imao *et al.* (1996) conducted experiments in a 120 pipe diameter long pipe to measure the turbulent fluctuation velocities and Reynolds shear stresses of the flow in an axially rotating pipe. The working fluid was water at $Re = 20000$. According to their results they reported that due to the stabilizing effects of the centrifugal force, the turbulence intensity of the turbulent swirling flow in the pipe decreases gradually with an increase

in swirl number. More dramatic reduction in shear stresses with an increase in swirl on the other hand was reported compared to turbulence intensity. In addition, their results confirmed the decrease of friction factor and changes in mean streamwise and azimuthal velocities with increasing swirl number as reported in the earlier studies.

In contrast with the results reported from using rotation method (i.e. axially rotating pipes) to generate swirl in turbulent pipe flows that illustrate an acceleration of the mean streamwise velocity at the center of the pipe, tangential injection methods result in the so-called 2-cell structure in which a flow reversal is produced at the center of the pipe. Chang & Kim (2001) performed measurements using PIV technique to measure velocity and turbulence intensity in a circular pipe at $Re = 1000,\ 15000,\ 20000$. Tangential injection method was utilized and the flow properties were measured for swirling and non-swirling flow. They reported at the highest Reynolds numbers, the maximum values of the measured axial velocity components had moved toward the test tube wall and produce more flow reversal a the center of the tube. Regarding the intensive velocity decrease at center of the pipe due to flow reversal, a considerable growth in the turbulence intensity of the swirling flow for high Reynolds numbers is reported at the pipe center compared to the non-swirling case. Their results are in agreement with those of King *et al.* (1969) and Medwell *et al.* (1989) that also utilized tangential injection method in their studies.

3.3. Swirling flow in curved circular-pipes

Despite the importance of investigating the effect of pipe curvature on swirling pipe flows, a few studies have been conducted on this topic. Among the experimental investigations that have been performed on swirling flow in curved circular-pipes are Shimizu & Sugino (1980), Anwer & So (1993) and Chang & Lee (2003). Also the numerical study of Pruvost *et al.* (2004) is included in this section due to the well performed comparison between the numerical results and the experimental data.

Shimizu & Sugino (1980) studied hydraulic losses and flow patterns of a swirling flow in curved pipes both experimentally and theoretically. The working fluid was water and the swirl was generated using guide vanes. The strength of the swirl were adjusted by a change of the guide vane angles. The type of the swirling motion provided by the guide vanes was free vortex. Hence, experiments in regard to the forced vortex type motion in curved pipes were also conducted to clearly investigate the effects of vortex types on the hydraulic losses and the flow patterns. A cylindrical Pitot tube with three holes was utilized to measure the velocity distribution within the curved pipe. They reported, for sufficiently high swirl numbers, the swirling flow through the curved pipes is a one-directionally rotative motion, and the angular momentum flux

in this type of flow decays along the pipe centerline in a wavy form. For lower swirl numbers, the angular momentum flux decays gradually at the first in bend pipes, and then drops sharply toward the bend exit. In addition, they illustrated that for the case of swirling flow into the bend pipes, the flow patterns are affected more by the bend curvature and wall roughness compared to the case of non-swirling inlet condition to the bend pipes.

Anwer & So (1993) conducted experimental study of a swirling turbulent flow through a 180° curved bend and its downstream tangent using rotating hot-wires, hot-film gauges and pressure transducers. The Reynolds number based on mean bulk velocity and the pipe diameter was $Re = 50000$ and the Dean number was $De = 13878$. During the experiments the wall static pressure, mean velocity distributions, Reynolds stresses and wall shear distribution around the pipe were measured. The swirl number for all swirling cases was $S = 1$. Their study consisted of two parts. Part one is investigation of the effect of swirl and bend curvature along the bend pipe while part two is on the recovery from swirl and bend curvature in the downstream tangent. As a result of superimposed solid-body rotation while having swirling flow, they reported the secondary flow pattern was re-organized in the cross-stream plane of the curved pipe because the rotating flow dominates the curved-pipe flow. In contrary to the non-swirling flow case, the measured wall static pressure at the outer wall was lower compared to the inner wall. In addition, Although there exists a significant difference between the wall shear at the outer and inner wall of the curved-pipe in the non-swirling case, their results depicted an approximately equal wall shear distribution at the outer and inner wall of the curved-pipe for the swirling flow case. they mentioned that this behavior is a consequence of the absence of the Dean cells in the swirling flow through curved-pipe case. As illustrated in their report, the normal stress distributions are more uniform and symmetric in the swirling flow case due to an increase in turbulence production of the normal stresses near the pipe wall in radial and tangential directions. This leads to a significant reduction in the radial and circumferential gradients of theses stresses that make them not sufficient to form and sustain secondary cells near the outer wall as in non-swirling case. In the second part of their study, Anwer & So (1993) , illustrate that as a consequence of the significant reduction of the angular momentum across the curved bend, the total recovery length from the the swirl and bend curvature is substantially shorter compared to the case of swirling flow through straight pipe. Hence, they reported that the bend curvature has an accelerating effect on swirl effect in pipe flows which shortens the recovery length.

Chang & Lee (2003) utilized Particle Image Velocimetry (PIV) method to measure the time averaged streamwise velocity distribution and turbulence intensity of the flow with swirl and without swirl in a 90° bent tube for

$Re = 10000, 15000, 20000, 25000$. Water was used as the working fluid for the two-dimensional particle image velocimetry technique. The swirl flow was generated by a tangential inlet. For the non-swirling case they again reported the same behavior of the flow along the bent pipe that a peak in streamwise velocity was observed at $0.5D$ before the bend and moved along the test tube, and was shifted toward the outer wall from $\theta = 45°$. High values for the maximum turbulence intensity was reported near the tube wall in the case of non-swirling flow. Due to the swirl generating method and strong swirl intensity, strong axial velocity near the tube wall and negative velocity in the center of the tube was reported at the entrance of the test tube. Depicted by their results, the swirl decayed along the bend and the balance in the velocity distribution was regained after $\theta = 90°$. In addition, together with the decay of swirl intensity along the test tube, the strong 2-celll phenomenon that appeared at the entrance of the tube was diminished. Similar to the case of non-swirling flow, the peak of the streamwise velocity distribution of the swirling flow in bent tube moved toward the inner wall until $\theta = 45°$, and beyond that point the peak zone was shifted toward the outer wall.

Pruvost *et al.* (2004) (2004) conducted a numerical flow prediction on the effect of swirl motion on flow structure in bend circular-pipes. In their study, two different bends, 90° and 180°, with similar characteristics to earlier experimental studies were investigated using the commercial CFD code FLUENT. The test cases were simulated from Sudo *et al.* (1998) work on flow through bend pipes with $Re = 60000$ and $De = 30000$, and Anwer & So (1993) studies on swirling flow into bend pipes with $Re = 50000$ and $De = 13878$, and consequently the numerical results were validated with the experimental results. They observed a reduction in the effect of the bend curvature on the flow while increasing the swirl number. Hence, they concluded that the curvature effects decrease by applying a swirl motion at the entrance of the bend. Consequently, in agreement to the earlier studies, they reported an increase in swirl intensity leads to a swirl dominate flow which the bend curvature effects on it are poor. On the other hand, for small values of swirl intensity, the outlet flow of the bend is resulting from a complex interaction between Dean vortices and swirl motion. According to their results, swirl motion tends to restore the symmetry in both mean velocity and turbulent kinetic energy profiles. In addition, they report that the turbulent values are more sensitive to the bend curvature, and compared to the mean profiles, higher values of swirl intensity is needed in order to obtain well restored symmetric turbulent values along the pipe radial direction. In order to characterize the bend curvature effects on the swirl motion, they introduced a drop criterion for swirl intensity. They illustrated that for bend inlet swirl intensities greater than 1, the drop in swirl intensity in both bend pipe and a straight pipe having same corresponding length as the bend are of

the order of each other. However, for swirl intensities lower than 1, high swirl intensity drop in bend pipe are reported compared to the straight pipe.

CHAPTER 4

Experimental setup and measurement technique

4.1. Experimental apparatus

4.1.1. *Hot-wire calibration nozzle*

The conventional hot-wire calibration were performed using the calibration nozzle. Passing through the contraction part of the nozzle, the flow is expected to have constant velocity at the outlet. The flow inside the stagnation chamber of the calibration nozzle facility is pressurized by the air flow coming from a compressor, and in order to keep the inlet pressure constant a regulator is mounted at the inlet of the calibration nozzle. The total pressure inside the stagnation chamber is measured with a pressure transducer relative to the ambient pressure. The outlet velocity of the nozzle then can be calculated using the Bernoulli's equation as

$$u = \sqrt{2\Delta P/\rho}\,, \tag{4.1}$$

where ΔP is the measured relative pressure and ρ is the density of the air. The temperate of the air inside the stagnation chamber is measured with a thermocouple, and is used for calculating the density of the air at each calibration point as well as providing the temperature deviations during the calibration. The atmospheric pressure is measured with a barometer, and together with the measure temperature provide enough information for calculating the air density through the ideal gas assumption. By manipulating the inlet pressure through the pressure regulator, different known velocity are provided at the nozzle outlet, where the hot-wire probe is mounted, for different calibration points.

4.1.2. *Rotating pipe flow facility*

The turbulent pipe flow measurements of both straight and bend pipe were performed in the rotating pipe facility located at the *Fluid Physics Laboratory* of the *Linné Flow Centre* at *KTH Mechanics* that consists of a 100 pipe diameter long axially rotating pipe. Figure 4.1 illustrates the rotating pipe that was designed and built by Facciolo (2006), and taken into operation in connection with the work of Facciolo (2006) and Örlü (2009). Figure 4.2 shows a schematic of the rotating pipe facility. Air at ambient temperature is provided by a centrifugal fan (A) with a butterfly valve for flow rate adjustment, which

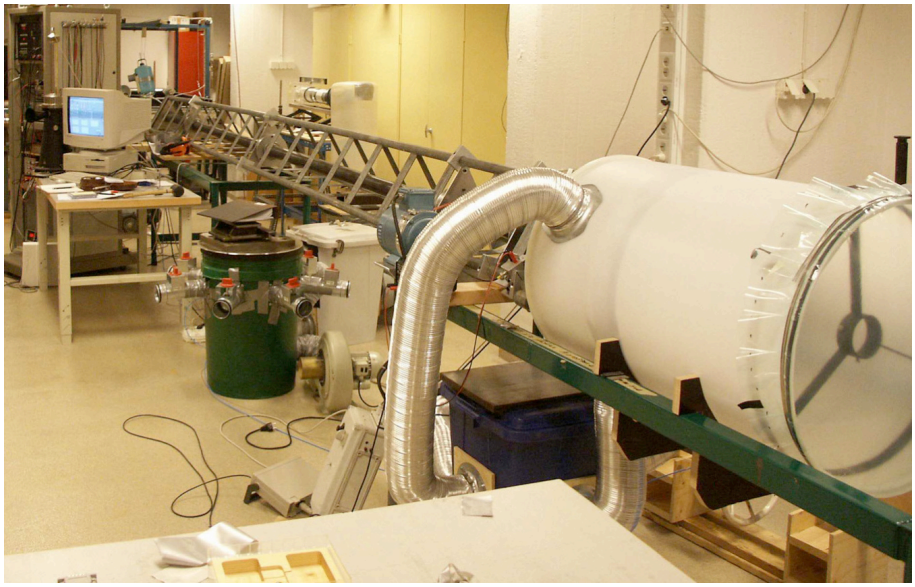

FIGURE 4.1. Rotating pipe experimental setup showing the pipe mounted within the triangular shaped framework and fed into the stagnation chamber covered by an elastic membrane.

is monitored through the pressure drop across an orifice plate (B) inserted in the air supply pipe. A distribution chamber (D) to reduce the transmission of vibrations generated by the fan is mounted on the way. From there the air stream is distributed into three different spiral pipes, which are symmetrically fed into the stagnation chamber (E), consisting of a honeycomb, in order to distribute the air evenly. One end of the cylindrical stagnation chamber is covered with an elastic membrane in order to further reduce the pressure fluctuations as apparent in figure 4.1. A bell mouth shaped entrance first leads the air into a one meter long stationary section, which is connected to the rotating pipe (K) through a rotating coupling (F). In the first section of the rotating part of the pipe a 12 cm long honeycomb (G), consisting of drinking straws of a diameter of 5 mm, is mounted which brings the flow into more or less solid body rotation. The inner diameter ofthe pipe amounts 60 mm whereas the wall thickness is 5 mm. The 6 m long pipe is made of seamless steel and has a honed inner surface with a roughness of less than 5 micron, according to manufacturer specifications. It is supported along its full length by 5 ball bearings (J), which are mounted within a rigid triangular shaped framework. The pipe is belt driven via a feedback controlled DC motor (H), which is capable to run the pipe up to rotational speeds of 2000 rpm. The pipe flow emanates as a free (M) 1.1 m above the floor into the ambient air at rest. By placing

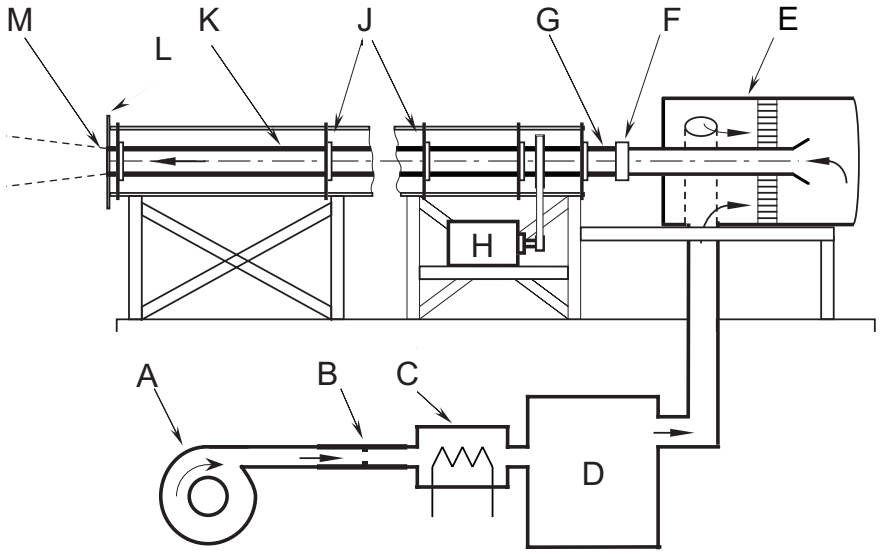

FIGURE 4.2. Schematic of the rotating pipe facility. A) Centrifugal fan, B) flow meter, C) electrical heater, D) distribution chamber, E) stagnation chamber, F) coupling between stationary and rotating pipe, G) honeycomb, H) DC motor, J) ball bearings, K) rotating pipe, L) circular end plate

the apparatus in a large laboratory with a large ventilation opening more than 60 pipe diameters downstream of the pipe outlet it is ensured that the jet can develop far away from any physical boundaries.

4.1.3. *Minimum Turbulence Level (MTL) wind tunnel*

The low-velocity calibration method in the irregular regime was tested by performing measurements in the wake behind the cylinder inside the *Minimum Turbulent Level* (MTL) windtunnel at the *Fluid Physics Laboratory* of the *Linné Flow Centre* at *KTH Mechanics)*. A schematic of the MTL wind tunnel is shown in figure 4.1.3. The maximum speed with an empty test section is 70 m/s and the streamwise velocity disturbance level is less than 0.025% of the free stream velocity. The air temperature can be regulated within $\pm 0.05°C$ by means of a heat exchanger. For further information regarding the flow quality in the MTL wind tunnel the intrested reader is reffered to Lindgre & Johansson (2002).

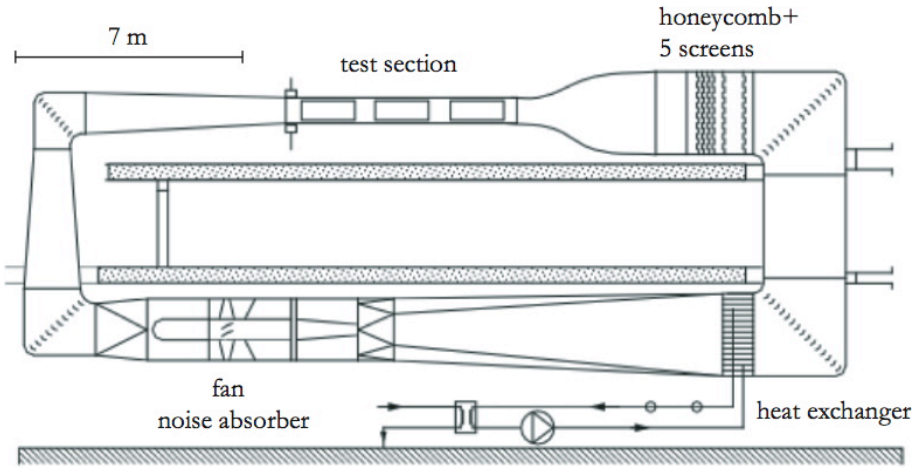

FIGURE 4.3. Schematic of the Minimum Turbulent Level (MTL) wind tunnel at KTH Mechanics. The dimensions of the test section are 0.8 m (hight), 1.2 m (width) and 7 m (length).

4.2. Hot-wire anemometry

4.2.1. *Probe manufacturing*

4.2.1a. *Conventional single wires.* Different types of single hot-wire probes were utilized for different measurements performed in the present study, and all the hot-wire probes were built in house through guide lines from Alfredsson & Tillmark (2005). For the near wall measurements of the straight non-swirling turbulent pipe flow, boundary layer type probes were used. Steel piano wires with diameter of 0.5 mm were etched and used as prongs. In order to reduce the aerodynamic blockage of the probe body in the near wall measurements, the tip of the prongs were bent toward the pipe wall. Ceramic cylindrical tubes with two holes were used as the fixture of the prongs, and for connecting the probe bodies to the probe holder the ceramic tubes were mounted inside steel tubes. Platinum wires (Pt core) with nominal diameters of 2.54 micron and 5 micron were used for the boundary layer probes in four different lengths (i.e. spacing distance between the ending tip of the prongs) according to the measurement purposes. However, the usual minimum length to diameter ratio of 200 for hot-wires was taken into consideration. The wire lengths were 510 micron and 670 micron for the wire with the nominal diameter of 2.54 micron, and 1 mm and 1.65 mm for the wire with the nominal diameter of 5 micron. For the turbulent swirling pipe flow measurements, Pt core wire with a diameter of 2.54 micron and length of 510 micron was soldered on bend prongs. The

wires were soldered on the outer part of the ending tips of the prongs that face the pipe wall. Due to the symmetric behavior of the fully developed turbulent flow in straight pipes as confirmed by Facciolo (2006) and Örlü (2009) for the present pipe facility, measurements were performed only in half of the pipe outlet. Consequently, the bend shape of the prongs did not have any effects on the measured data. On the other hand, according to non-symmetric behavior of the flow in bend pipes, measurements were needed and performed in both sides of the bend pipe outlet. In addition, the aim of the bend pipe measurements was to investigate the large scale structures of the flow and near wall measurements was not needed for that purpose. Hence, straight single hot-wires were utilized in order to hinder the effects of the shape of the hot-wire probe. Platinum wire with nominal diameter of 5 micron and length of 1.035 mm was soldered on straight prongs for this purpose. For both cases, the single wire hot-wires was fixed in a 300 mm long probe holder that was mounted on an airfoil shaped arm in order to minimize the upstream effects of the probe and the probe holder on the flow. For vortex shedding measurements in the minimum turbulence level (MTL) wind tunnel, straight single wires were utilized by soldering Pt core wire with a diameter of 5 micron and length of 1.1 mm on straight prongs.

4.2.1b. *Array of 6 hot-wires on a circuit board.* The array of hot-wires[1] was built in the house by getting the idea from Monty *et al.* (2007). Instead of using ceramic cylinders for probes bodies, an array of prongs were mounted on a printed electronic circuit board *PCB*. Using this method enhanced the process of measuring the ability to use six hot-wires at the same time for measuring the time-series of the flow properties. The traveling traverse system for measuring along the pipe radial coordinate then was neglected and just an azimuthal traverse system for rotating the electronic circuit board, on which the six hot-wires were mounted, was needed. Using the rake of hot-wire probe (i.e. in the present experiment the PCB) makes it possible to measure simultaneously at different points and hence find out about spatial correlations and infer what kind of turbulent structures the flow has, e.g., Dean vortices' thickness in the present experiment.

At first, the process of using the circuit board was started by mounting a simple array of prongs on the circuit for using single wire hot-wires with constant distances from each other along the pipe radius for half of the pipe diameter including the pipe center. The diameter of the pipe was 60 mm, and for primary measurements for testing the circuit board the near wall measurements of the pipe flow was neglected, so the arrange of the prongs along the pipe radius starting from the pipe centerline was distributed for 25 mm out of the pipe radius of 30 mm.Hence, the constant distance between each hot-wire (prong)

[1]The array of 6 hot-wires on a circuit board was only manufactured during the present study, and no data was acquired using this array.

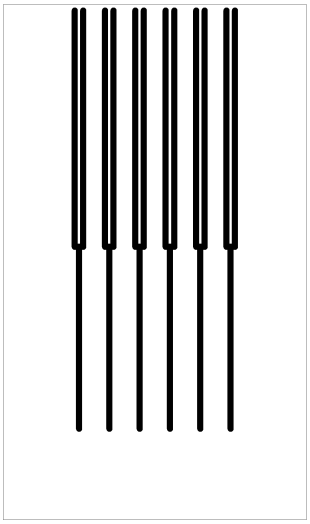

FIGURE 4.4. A sketch of the circuit board

on the circuit board was 5 mm. For implementing the hot wires on the circuit board, a two sided electronic circuit board was used in order to solder each of the two needed prongs for a single wire hot-wire on one its sides. The circuit board was designed using the electronic circuit board designing software Easily Applicable Graphical Layout Editor (EAGLE), Version 5.10.0 for Mac OS X,Light Edition. Figure 4.4 shows an sketch of the primary design of one side of the circuit board that were used for mounting the six hot-wires with constant distance from each other. After designing the circuit board it was printed on transparent film. The photo resist PCB was used which means the PCB already had the photo-resist substance applied on it. To protect the photo-resist layer the PCB was covered with a blue sticker that is UV protective. The printed transparent film was then adjusted on each side of the circuit board, two sticked printed transparent film for each side. Next was to place the PCB with the copper side facing the UV source for each side of the double-sided circuit board, inside the UV exposure unit for about 10 minutes. After that, it was put in a plastic container which was filled with developer and water. After couple of minutes the photo-resist substance was removed from the area of circuit which was not on the printed film. The final step was to etch the copper with Ferric Chloride mixed with water in the plastic container. After 15 minutes in the etching solution the board was almost complete, only a small area of copper remained. Aiming to accelerate the etching process one would have to heat the Ferric Chloride up to $40°C$ and gently shake the container to move the etching solution around. The circuit board was cleaned up with Acetone at the end.

The thickness of two sided circuit board was 1 mm, and the prongs that were soldered on the circuit had a diameter of 0.5 mm; therefore, the distance left between the prongs for soldering the single wire was about 2 mm.

4.2.2. *Data acquisition*

The hot-wire anemometer system used is a Dantec StreamLine 90N10 frame in conjunction with a 90C10 constant temperature anemometer module. The hot-wires were operated in constant temperature anemometry mode at an overheat resistance ratio of 80%. The utilized 16-bit analog to digital convertor card was a NI PCI-6014. In order to match the voltage range of the card, an offset and gain was applid to the top of the bridge voltage for each hot-wire setup. According to figure 2.10, the sampling frequency was set to 20 kHz, and it was used for all the measurements. The frequency response given by the square wave test was satisfying the needed sampling frequency for all the hot-wire setups. An analog low pass filter with 10 kHz cut-off frequency, half of the sampling frequency, was used prior to the data acquisition as the Nyquist or folding frequency with respect to the sampling frequency in order to allow sufficiently resolved time signals for spectral analysis.

4.2.3. *Traversing system*

A combined manual and automatic traversing system was used for hot-wire data acquisition of straight and bend pipe measurements. The manual part is consisted of a micrometer mounted between the automatic traverse system and the airfoil shaped arm, and was used for the near wall measurements of non-swirling turbulent pipe flow due to the accuracy needed for small distance traversing and safety issues of the hot-wire probe. The automatic traverse system is a AIRPAX L92411-P2 with a trusted traversing accuracy of 0.1 mm. Since near wall measurements were included, the data acquisition positions for the straight non-swirling turbulent pipe flow investigation were set logarithmically along the pipe radius. The MTL wind tunnel is equipped with a five degree of freedom (x, y, z and two angles α, ϕ) traversing system operated with computer-controlled dc motors. Here, however, only x and y are used which are the streamwise and vertical coordinates.

4.3. Calibration

4.3.1. *Conventional hot-wire calibration*

The relation between the hot-wire voltage (i.e. constant temperature anemometer output) and the actual flow velocity is established through calibration curves. Exposing the probe to a set of known velocities, the relative voltage response of the hot-wire setup can be obtained. The transfer function that converts the data records from voltage into velocity can then be determined by fitting a curve through the calibration points. *Polynomial* curve fitting

and *Power law* curve fitting are the main methods to fit calibration curves on the acquired calibration points. The Polynomial curve fitting for hot-wire calibration plots U as a function of E and is obtained by fitting a forth order polynomial trend line on the calibration points. The forth order polynomial relation is given as

$$U = C_0 + C_1 E + C_2 E^2 + C_3 E^3 + C_4 E^4 \,, \tag{4.2}$$

where U is the known velocity that the hot-wire probe is exposed to, E is hot-wire voltage response and C_0 to C_4 are calibration constants that have to be determined. This curve fitting method makes very good fits with small linearization error, but it may oscillate considerably if the velocity is outside the velocity range, e.g. low velocities. To overcome this problem a method with physical basis was reported by King (1914) as *King's law* for predicting fitted curve on the calibration data. This method utilizes *Newton's law of cooling* which relates the *Joule heating* to the cooling due to forced convection. The power law relation is given through the so-called *King's law* relation and plots E^2 as a function of U^n in double logarithmic scale through an iterative procedure as

$$E^2 = A + B\, U^n \,, \tag{4.3}$$

where by iteratively varying n, calibration constants A and B for acceptable curve fitting errors are determined. The determined constants (i.e. A, B and n) are variables dependent on physical properties and characteristics of hot-wire setup. The problem with the King's law is that only forced convection conditions were utilized in order to derive the relation whereas in many cases, e.g. low velocities, natural convection plays an important role. In order to compensate for natural convection, which appears to be a problem for low speed measurements, a modified version of King's law was reported by Johansson & Alfredsson (1982) as

$$U = k_1 (E^2 - E_0^2)^{1/n} + k_2 (E - E_0)^{1/2} \,, \tag{4.4}$$

where E and E_0 are the hot-wire voltage response at the velocities U and zero respectively, and k_1, k_2 and n are calibration constants. The second term in equation (4.4) is related to the effects of natural convection, which becomes important at low velocities as mentioned earlier.

In the present study, the single hot-wires were calibrated after long aging time using the hot-wire calibration nozzle where the free jet velocity of the nozzle was known through pressure drop measurements. The calibration procedure was

performed by taking a set of around 30 calibration points with a concentration on low velocities. The modified King's law was utilized for fitting calibration curve on calibration data. The calibration curves were taken before and after measurements, and E_0 of the hot-wires were also checked for eventual changes. The average between the pre/post-measuremnt calibrations was used in the case that they were identical. Otherwise, in the case of a drift or change in E_0 or calibration curve, the one that was taken closer in time to each measurement case was used. The latter case, however, barely occurred.

4.3.2. *Hot-wire temperature compensation*

It is important to keep track of the temperature during calibration and also the actual measurements. If the temperature varies within the calibration or from calibration to measurements, it is necessary to compensate for the temperature variations. In order to compensate the effect of ambient temperature variation on the hot-wire voltage during calibration process and also measurements following relation was used.

$$E_{out}(T_{ref})^2 = E_{out}(T)^2 \left(\frac{T_h - T_{ref}}{T_h - T} \right) , \tag{4.5}$$

where T_h is the hot-wire temperature that is fixed if the process is operating in the CTA mode, T is the flow ambient temperature that changes during the calibration or measurements, and T_{ref} is the reference temperature for the calibration which usually is the average of T for all calibration points. $E_{out}(T)$ is the voltage from anemometer and $E_{out}(T_{ref})$ would be the compensated voltage. Hence, if ambient temperature of the flow at every points of calibration remained constant, the need of compensation was eliminated.

The resistance overheat ratio, a_R, that is related to temperature overheat ratio, a_T, is set by the user with respect to the case of measurements,

$$a_R = \frac{R(T_h) - R(T_{ref})}{R(T_{ref})} , \tag{4.6}$$

$$a_T = \frac{T_h - T_{ref}}{T_{ref}} . \tag{4.7}$$

Assuming the resistance of the heated hot-wire changes linearly with respect to temperature changes gives

$$R(T_h) = R(T_{ref})[1 + \alpha_{el}(T_h - T_{ref})] , \tag{4.8}$$

where α_{el} is the temperature coefficient of electrical resistivity. One shall find the relation between a_R and a_T as $a_T = a_R/(\alpha_{el} T_{ref})$, and set the appropriate resistance overheat ratio, a_R, to get the temperature overheat ratio, a_T, and thus the operating temperature needed for the case of the measurements. The

compensated hot-wire anemometer voltage relation can be rewritten using resistance overheat ratio and the temperature coefficient of electrical resistivity as

$$E_{out}(T_{ref})^2 = E_{out}(T)^2 \left(1 - \frac{T - T_{ref}}{a_R/\alpha_{el}}\right)^{-1}. \tag{4.9}$$

During calibration, the nozzle flow temperature, T, is measured by use of a thermocouple at each calibration point. The compensated hot-wire voltage can be calculated by knowing the temperature coefficient of electrical resistance, α_{el}. The value of α_{el} for different hot-wire materials is available in the tables of *Hot-Wire Anemometry* text books, for instance, Bruun (1995) mentions $\alpha = 0.0036K^{-1}$ for Tungsten at $20°C$, but according to van Dijk (1999) these values are reliable for macroscopic amount of hot-wire materials. van Dijk (1999) and Örlü (2006) reported that during tormenting processes that Tungsten undergoes while spooling, the crystal-structure of the material becomes less ordered which increases the resistance for electrons to travel along the spool. This affects the temperature coefficient of electrical resistance by the means of decreasing it. While mounting the wire on the prongs of the probe by soldering or welding it, the crystal-structure of the wire becomes even less ordered and the resistance coefficient of the wire ends up being even worse, hence the value of α_{el} becomes lower. Due to the affects of these processes to α_{el}, the mentioned values in the literatures are not reliable.

To overcome this problem in the present study, an iterating method was used to estimate α_{el} of the mounted tungsten hot-wire on the probes. For that purpose, The hot-wire was first calibrated using the air flow with the ambient room temperature through the nozzle, and then calibrated once more using a heater to heat the air flow before entering the nozzle, and for both cases the temperature variations in the nozzle were measured by means of a thermocouple. Using modified King's law and the average of temperature variations at the ambient room temperature as T_{ref} for each calibration, two curves were fitted in the $U[m/s]$ vs. $E[V]$ diagram on the measured points of each calibration after compensating the temperature difference against T_{ref} with the iterated α_{el}. The goal was to reach the value α_{el} that makes the two curves overlap. Figure 4.5 shows the calibration points for both hot and cold temperature together with the fitted curves. In figure 4.5(a) the hot-wire anemometer voltage for the hot temperature calibration is not compensated against the T_{ref}, and the difference between the two curves before iteration is clearly shown. But in figure 4.5(b) all the calibration voltages are compensated against T_{ref} and the best possible overlap between two curves is shown after iterating α_{el}. The obtained α_{el} is $0.00335K^{-1}$ which is lower than $0.0036K^{-1}$ mentioned by Bruun

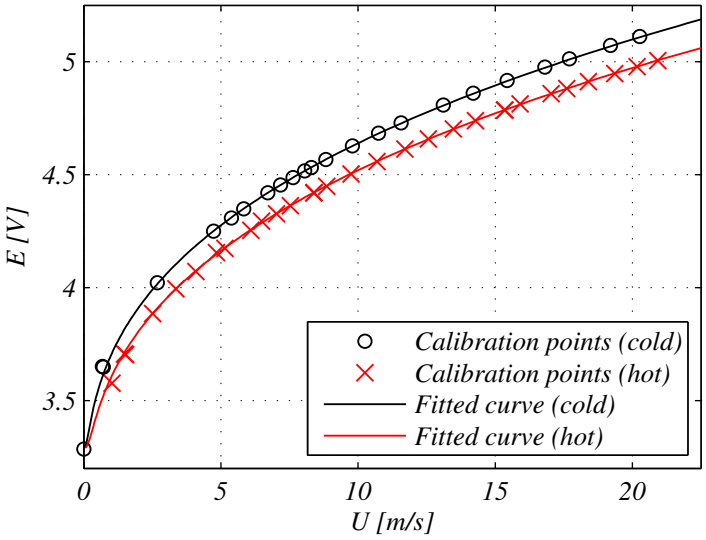

(a) The high temperature calibration voltages are not compensated

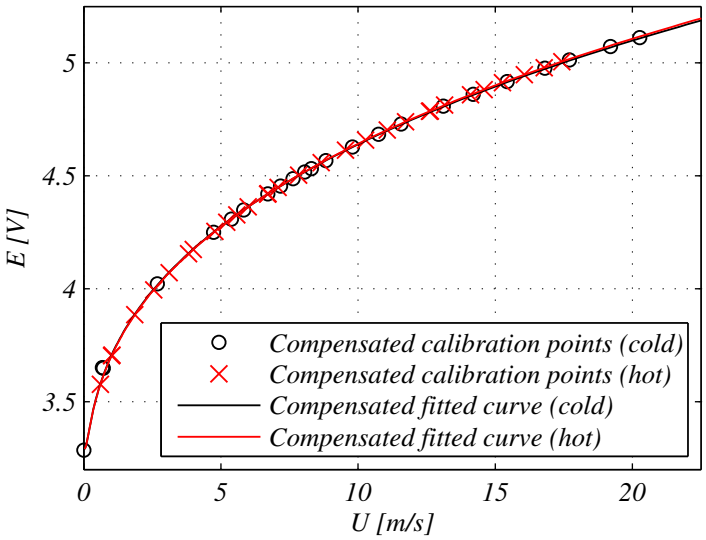

(b) Both cases are compensated

FIGURE 4.5. Calibration points and modified King's law fitted curves for high and low temperatures

(1995). The reduction of α_{el} is in agreement with van Dijk (1999) and Örlü (2006) reports.

4.3.3. *Low speed calibration for hot-wires*

Due to accuracy limitations of pressure transducers as well as other insensitivities of the conventional ways for hot-wire calibration at low velocities the vortex shedding frequency method was used. In this method, the shedding frequency of the wake behind a circular cylinder located in the minimum-turbulence-level (MTL) wind-tunnel at KTH Mechanics was used in order to determine the flow velocity accurately using the relation between flow velocity, shedding frequency, diameter of cylinder and *Strouhal number*, St. The velocity time series of the flow behind the cylinder was measured for different locations downstream as well as vertical offsets from the center of the circular cylinder, and the shedding frequencies were obtained from the dominant peak of the power spectral density.

The method of using vortex-shedding frequency in order to calibrate hot-wire sensors at low velocities is reported as having been used successfully over times by different experimentalists but not all of them had used the same relation in order to relate Reynolds and Strouhal numbers. Czech physicist, Vincent Strouhal measured the frequency of oscillating wires and rods whirled through the air for the first time, Strouhal (1878), and formed a dimensionless parameter which later on was named after him as the Strouhal number by Benard (1926). The Strouhal number that describes oscillating flow mechanism is defined as

$$St = \frac{fL}{U}\,, \tag{4.10}$$

where f is the frequency of the vortex shedding, L is the characteristic length, and U is the velocity of the fluid. Benard found constant values for Strouhal number with respect to different thicknesses of wires and rods, and also found that one cannot find constant Strouhal number for thin oscillating wires. Following Strouhal, Rayleigh (1896) wire measurements, Roshko (1954) hot-wire measurements, and also the fitted curve over experimental data of Berger (1964) were in acceptable agreement with Strouhal's and Benard's results concluding the fact that the Strouhal number is not constant for thin oscillating wires or to put it more accurately for low Re numbers of the range of $40 < Re < 160$. According to Rayleigh, Roshko and Berger measurements, the relation between Strouhal and Reynolds numbers is not linear. To overcome this non-linearity another dimensionless parameter was introduced by Roshko (1954) which has a linear relation with the Reynlds number. The non-dimensional *Roshko number* is defined as

$$Ro = StRe = \frac{fL^2}{\nu}\,. \tag{4.11}$$

Using this linear dependency between shedding frequency and velocity, Roshko proposed a new way for measuring very low velocities. The linear relation

between Ro and Re numbers as stated by Roshko is

$$Ro = 0.212Re - 4.5, \qquad (50 < Re < 150) \tag{4.12}$$

$$Ro = 0.212Re - 2.7, \qquad (300 < Re < 2000)\,. \tag{4.13}$$

Since the calibration at low velocities has brought about lot of concerns among experimentalist, the work of Roshko (1954) has been followed by Tritton (1959), Berger & Wille (1972), Kohan & Schwarz (1973), Williamson (1989), König *et al.* (1990), Lee & Budwig (1991), and Lanspeary (1997). The attempt was to find the relation between St and Re numbers, but discontinuities were observed for all non-linear $St - Re$ curves except for Roshko's investigations. Observing the discontinuity at St-Re curve, Lee & Budwig (1991) reported that the observed discontinuity is due to unmodified ending conditions of the circular cylinders that are being used to provide vortex shedding. According to their span-wise flow visualizations in the wind-tunnel section, they reported that modified ending conditions for mounting circular cylinders are needed to gain modified parallel vortex shedding which can be used for an accurate vortex-shedding low-speed calibration method. They also reported that for cylinders with no end modifications the axis of the vortex filament is non-parallel to the axis of the cylinder which leads to oblique vortex shedding mode. Using cylindrical sleeves at each end of the cylinder as the end modifications in order to generate parallel vortex shedding, Lee and Budwig found a non-linear relation between St and Re numbers as

$$St = 2.531 \times 10^{-5} Re + 0.2102 - \frac{4.332}{Re}\,. \tag{4.14}$$

Williamson (1988, 1989) introduced another relation to overcome the effect of non-modified ending conditions and oblique vortex shedding as

$$\frac{St}{\cos\theta} = \frac{-3.3265}{Re} + 0.1816 + 0.00016Re\,, \tag{4.15}$$

where θ is the angle of oblique shedding.

In the present study, the vortex shedding method for low velocity calibration of hot-wires was investigated in the MTL wind-tunnel at KTH Mechanics where the dimensions of the test section are $7.0 \times 0.8 \times 1.2\ m^3$. Two circular cylinder with diameters of 8 mm and 12 mm were used. Cylinders were fixed by fixtures from each side of the wind-tunnel and were stiff enough not to oscillate. The L/D ratios of the 8 mm and 12 mm diameter cylinders were 150 and 100 respectively.

The aim was to investigate if the vortex shedding method for low velocity calibration can be utilized. For that purpose, first the hot-wire was calibrated using the conventional method. The calibration points and fitted modified King's law curve are shown in figure 4.6 as open circles and solid lines respectively. Then, for each imposed velocity, the time series of hot-wire response was

taken for both inside and outside the wake region. The downstream position of data acquisition was 3 cylinder-diameters, and the vertical offset for irrotational region (outside the wake) was 6 cylinder-diameters for all cases. The vertical offsets for wake region were 2 and 2.5 cylinder-diameters for 8 mm and 12 mm cylinders respectively. The data acquisition in irrotational region was in order to determine the hot-wire voltage response to each imposed velocity, and the shedding frequency corresponding to that velocity was determined by the dominant peak of power spectral density of hot-wire voltage response inside the wake region. Using the averaged hot-wire voltage response in laminar region and the determined velocity from the shedding frequency inside the wake, a set of data containing velocity versus averaged hot-wire voltage is obtained that can be compared to the primary calibrations. The results are depicted as black asterisk in figure 4.6 for both cylinders. In addition, in order to illustrate the shedding frequencies (i.e. dominant peak of PSD) more clearly, pre-multiplied power spectral density functions of data acquisition inside the wake region are depicted against the average hot-wire voltage response in irrotational region for both cylinders in figure 4.7.

The plus signs in figure 4.6 are the acquired data outside the wake region for each velocity and their averaged hot-wire voltage response were used for the vortex shedding method, i.e., the plus signs and the asterisks have the same voltage for each velocity. It can be observed that as the velocity increases the difference between the determined velocity from vortex shedding method and conventional calibration grows. The growing discrepancy is due to the limitation of the used St Re relation by Roshko, i.e. equation (4.13), which is only validated up to Re_D equal to 2000 that corresponds to about 3.73 m/s and 2.51 m/s for the 8 mm and 12 mm cylinders, respectively. These velocities are depicted as vertical dashed lines in figures 4.6(a) and 4.6(b). It is known that for $Re_D > 2000$ the St number gradually decreases[2] which is not applied in St Re relation of Roshko. This reduction in the St number would cause the determined velocity to increase and thereby reduce the discrepancy. Here, however, the focus of interest is the low velocity region, hence, no attempt has been made to further improve the relation for $Re_D > 2000$. The position of data acquisition in the wake region in order to determine the shedding frequency was chosen according to earlier studies. In addition to reassure that the hot-wire is capturing the shedding phenomena the oscilloscope was checked for sinusoidal waves that represent vortex shedding. Hence, the vertical offsets of two cylinders differ slightly. However, since the shedding frequency inside the wake region is expected to be homogeneous, the homogeneity of St number was investigated by mapping the area behind the cylinders (i.e., the wake region) for two different velocities. The area of mapping included 1 to 6 cylinder-diameters downstream for both cylinders while 0 to 4 and 0 to 6

[2]Norberg (1994)

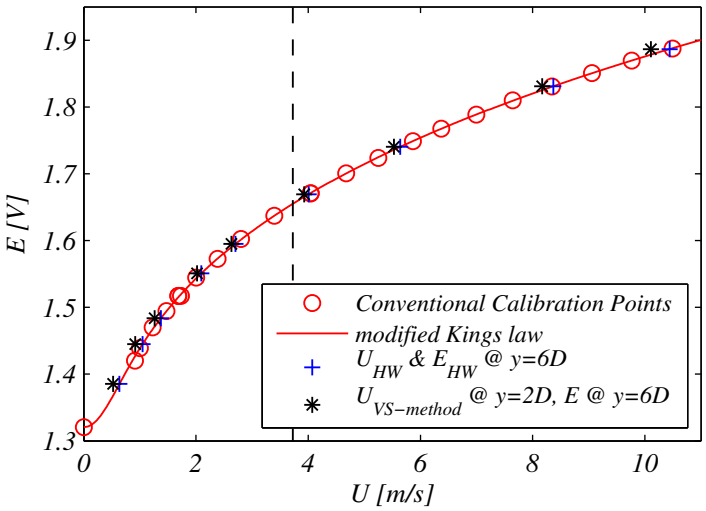

(a) The diameter of the cylinder is 8 mm. Vertical dashed line indicates $Re_D = 2000$.

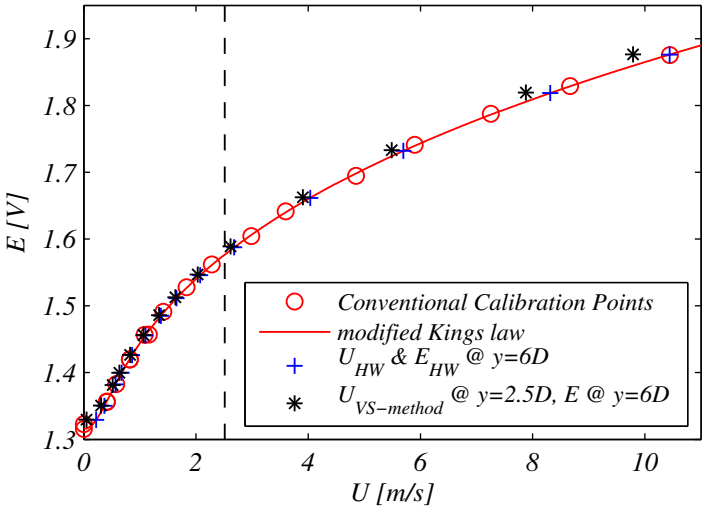

(b) The diameter of the cylinder is 12 mm. Vertical dashed line indicates $Re_D = 2000$.

FIGURE 4.6. Vortex shedding method compared to conventional calibration

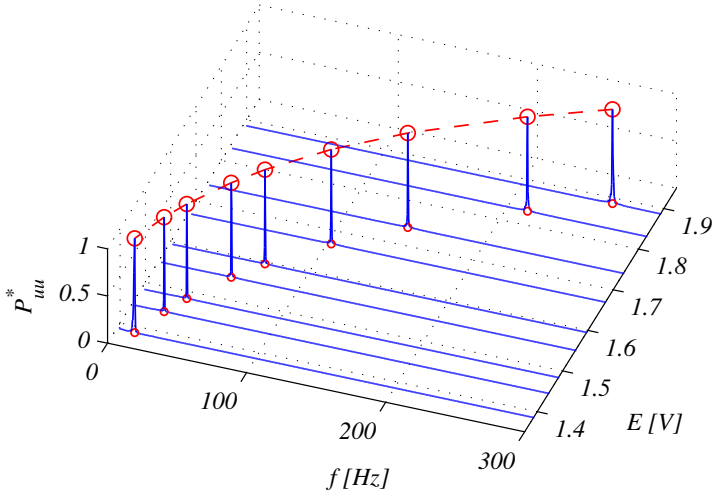

(a) The diameter of the cylinder is 8 mm.

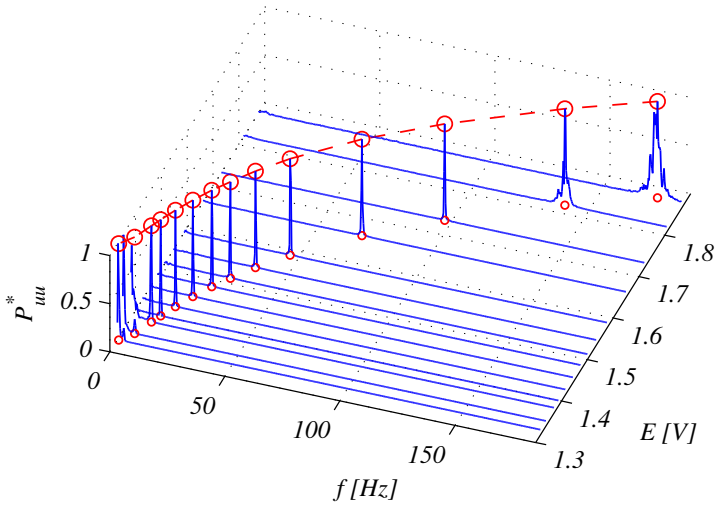

(b) The diameter of the cylinder is 12 mm.

FIGURE 4.7. Pre-multiplied power spectral density functions of data acquisition inside the wake region against the average hot-wire voltage response in irrotational region

cylinder-diameters vertical offset for 8 mm and 12 mm cylinders respectively. The pre-multiplied power spectral density maps across cross-stream plane for hot-wire voltage signal for both cases of cylinders are depicted in figure 4.8. It

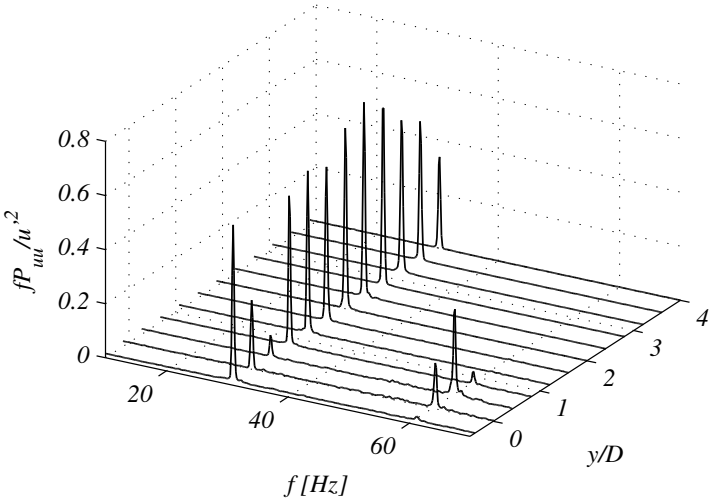

(a) At $3D$ downstream position of $8mm$ diameter cylinder.

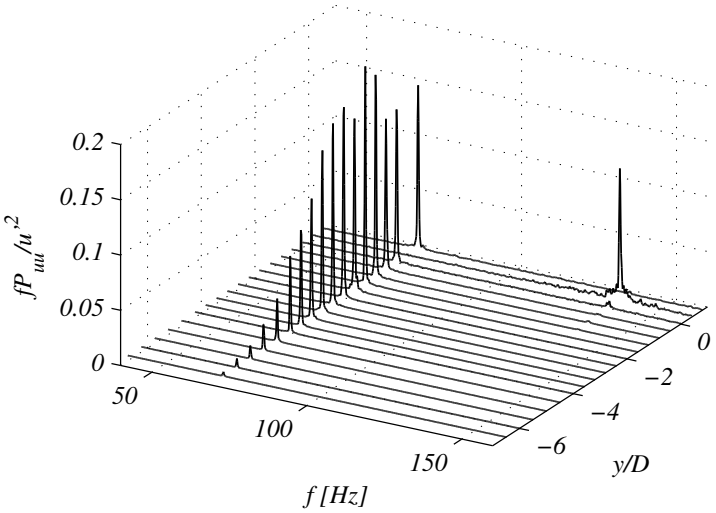

(b) At $1.5D$ downstream position of $12mm$ diameter cylinder.

FIGURE 4.8. Pre-multiplied power spectral density map for the voltage signal from the hot-wire inside the wake region across the cross-stream plane showing the dominant peak of vortex shedding frequency.

is clearly illustrated that the dominant vortex shedding frequency is constant across different vertical offsets in the cross-stream plane inside the wake region

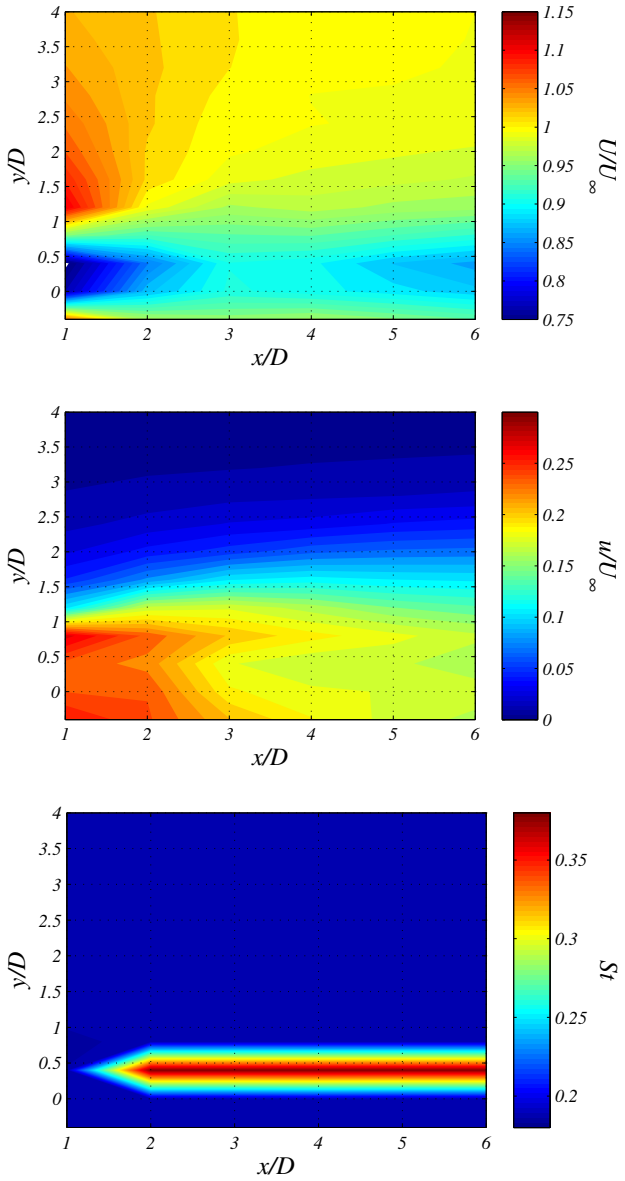

FIGURE 4.9. Contour plots of streamwise mean velocity and turbulence intensity normalized by freestream velocity as well as the Strouhal number, St, for cylinder of diameter of 8 mm.

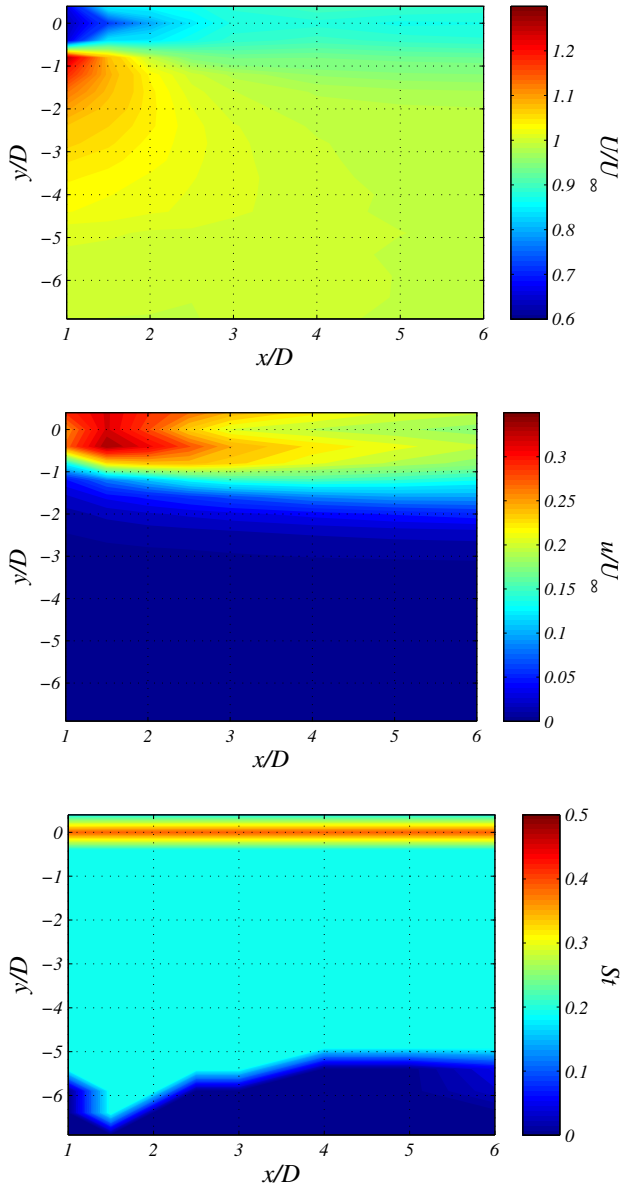

FIGURE 4.10. Contour plots of streamwise mean velocity and turbulence intensity normalized by freestream velocity as well as the Strouhal number, St, for cylinder of diameter of 12 mm.

except for the position behind the cylinders. In addition, the contour plots of streamwise mean velocity and turbulence intensity normalized by freestream velocity as well as the Strouhal number, St, for cylinders of diameters of 8 mm and 12 mm are depicted in figures 4.9 and 4.10, respectively. It can be seen from those figures that the downstream position of $3D$ and vertical offset of $6D$ is suitable for obtaining the hot wire voltage response for free stream velocity in irrotational region. Also, the turbulence intensity reaches the free stream level much quicker when increasing vertical offset compared to mean velocity. In addition, as shown in the strouhal number contour plots, the results illustrate a vast area of shedding frequency homogeneity in the wake region.

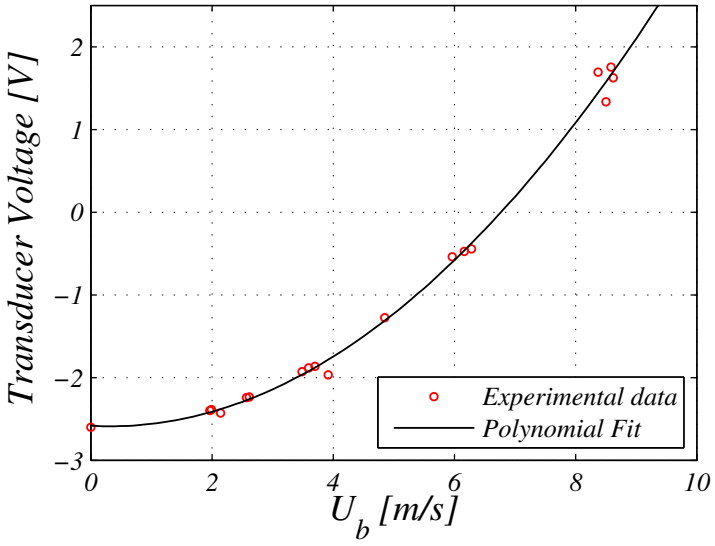

FIGURE 4.11. Mass flow calibration curve against bulk velocity

4.3.4. *Mass Flow Meter*

Stable inflow conditions with no variations in time was needed for obtaining fully developed pipe flow. To monitor the inflow conditions of the pipe, the voltage response of a *MPX10DP* pressure transducer measuring the pressure drop across an orifice plate in the flow meter was acquired. As the flow meter is depicted in figure 4.2, the orifice plate with a diameter of 28 mm was placed between the fan and the settling chamber in 40 mm diameter pipe. For the case of straight non-swirling pipe flow measurements, the desired Reynolds number, Re_D, was obtained by setting the center-line velocity at the pipe outlet to the estimated center-line velocity according to that Reynolds number. This method

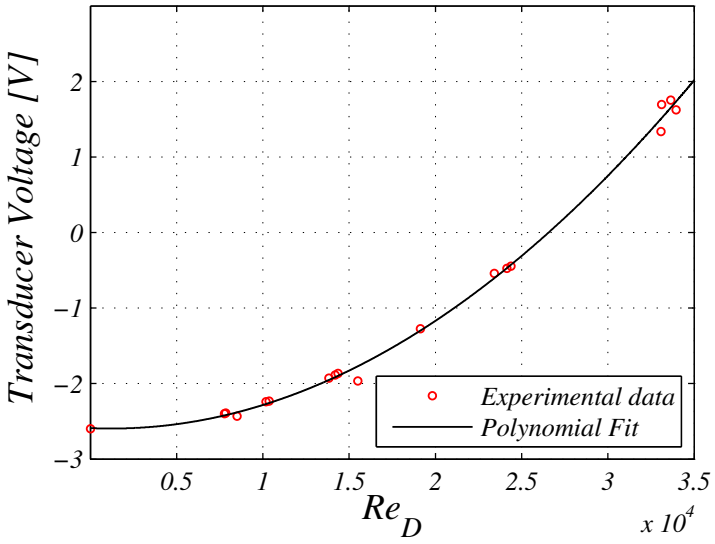

FIGURE 4.12. Mass flow calibration curve against Reynolds number based on bulk velocity and pipe diameter.

is not applicable for the swirling and bend pipe measurements since the centerline velocity is affected by the case conditions and cannot be estimated and set accurately for different Reynolds numbers. Hence, the orifice flow meter (i.e. output voltage of pressure transducer) was calibrated against different inflow speed through the straight non-swirling pipe measurement to set the desired Reynolds number for swirling and bend pipe cases. Integrating the velocity profile of the straight non-swirling pipe flow across radial direction for different inflow speed, the bulk velocity , U_b, and consequently Reynolds number, Re_D, was determined. Hence, having acquired the mass flow meter response during the measurements, it was calibrated against different Reynolds numbers. The transducer voltage as a function of the bulk velocity and the Reynolds number is shown in figures 4.11 and 4.12 respectively. Since the pressure transducer has a linear response between the pressure drop and the voltage, the relation between the transducer voltage and bulk velocity was expected to be near parabolic. Hence, the polynomial fit was used for fitting the curve over experimental data.

CHAPTER 5

Turbulent pipe flow

5.1. Measurement matrix

Hot-wire Measurements were conducted to investigate the behavior of fully developed turbulent pipe flow at the outlet of the straight pipe for both swirling and non-swirling conditions. The swirl effect produced by axially rotating pipe on the fully developed turbulent pipe flow was investigated as a result of the experiments. Also, as the inlet condition of the bend in the bend pipe measurements, the straight pipe measurements were needed to illustrate the effects of pipe curvature with respect to the inlet conditions. In addition, the complete profile of mean streamwise velocity of the non-swirling fully developed turbulent pipe flow was integrated to determine the bulk velocity, U_b, of the pipe flow, and hence calibrate the mass flow meter. For this purpose, near-wall measurements were needed in order to obtain the complete profiles of the mean velocity. This brought up additional interest to perform measurements in order to study the spatial resolution effects on pipe flow near-wall measurements. Four hot-wire probes with different spacing distance between the ending tips of the prongs were utilized as mentioned in probe manufacturing section in chapter 4.

Non-swirling turbulent pipe flow measurements were conducted for different Reynolds numbers, Re_D. The desired Reynolds numbers were obtained by adjusting the centerline velocity, U_{cl}, as explained in mass flow meter section in chapter 4. The experimental parameters of the non-swirling turbulent pipe flow measurements are tabulated in table 1. The cases A, B, C, and D are representing measurements mainly in the same pipe flow conditions with different utilized hot-wire probes according to the distance between the prong tips, i.e. wire length in each hot-wire probe. The wire length in viscous scales, L^+, for each measurement case is also presented in table 1, where $L^+ = \ell/\ell^*$, and ℓ denotes the dimensional wire length.

The hot-wire was placed inside the pipe at half pipe diameter upstream of the pipe outlet for these cases. These measurements were performed in order to investigate the effect of measuring at different positions. As apparent, the mean velocity profiles are not affected according to different positions since the

Case	U_{cl} $[ms^{-1}]$	Re_D $[-]$	R^+ $[-]$	ℓ $[mm]$	d $[\mu m]$	ℓ_* $[\mu m]$	L^+ $[-]$	Δt^+ $[-]$	$T_{min}U_{cl}/R$ $[-]$	$T_{max}U_{cl}/R$ $[-]$
A_1	10.59	33 070	901	0.51	2.5	33.3	15	0.70	7 000	18 300
A_2	7.89	24 390	691	0.51	2.5	43.4	12	0.41	5 300	13 600
A_3	4.66	14 340	435	0.51	2.5	68.9	7	0.16	5 420	13 000
B_1	10.47	33 120	902	0.67	2.5	33.2	20	0.69	7 000	18 200
B_2	7.48	23 420	664	0.67	2.5	45.2	15	0.37	5 000	13 000
B_3	4.40	13 820	423	0.67	2.5	70.9	9	0.15	5 100	12 400
B_4	3.31	10 360	332	0.67	2.5	90.3	7	0.09	5 300	12 100
B_5	2.49	7 770	261	0.67	2.5	114.9	6	0.06	5 200	11 700
C_1	10.68	33 650	916	1.00	5.0	32.7	31	0.71	7 100	18 500
C_2	7.75	24 140	688	1.00	5.0	43.6	23	0.40	5 200	13 400
C_3	6.12	19 140	561	1.00	5.0	53.4	19	0.27	5 100	12 200
C_4	4.54	14 190	433	1.00	5.0	69.3	14	0.16	5 300	12 700
C_5	3.27	10 180	326	1.00	5.0	91.9	11	0.09	5 200	12 000
C_6	2.54	7 850	264	1.00	5.0	113.6	9	0.06	5 300	12 000
D_1	10.78	33 960	920	1.65	5.0	32.6	51	0.72	7 200	18 700
D_2	4.93	15 500	470	1.65	5.0	63.8	26	0.19	5 800	13 800
D_3	2.70	8 520	283	1.65	5.0	106.1	16	0.07	5 700	12 700

TABLE 1. Experimental parameters for present hot-wire measurements of non-swirling turbulent straight pipe flow.

flow is fully developed. Hence, the half pipe diameter upstream the pipe outlet position was set for measurements since observation was needed during manual traversing through the wall in near-wall measurements.

For swirling turbulent pipe flow investigations, the measurements were performed at the pipe outlet position, and due to pipe vibrations near wall measurements were not conducted. The experimental parameters for swirling turbulent pipe flow is tabulated in table 2. The Reynolds number, Re_D, for the measurement cases E was according to the mass flow meter curve. The swirl number, S, was determined using the relation $S = V_W/U_b$, where V_w is the solid body rotation linear velocity of the rotating pipe flow. V_w was set by counting the steps mounted on the perimeter of the pipe via a step counter. Each full round of the pipe around its centerline contains 200 steps.

Case	U_b $[ms^{-1}]$	Re_D $[-]$	S $[-]$
E_1	6.23	23 570	0.1
E_2	6.26	23 680	0.3
E_3	6.33	24 110	0.5
E_4	3.61	13 680	0.5
E_5	8.70	33 040	0.5

TABLE 2. Experimental parameters for present hot-wire measurements of swirling turbulent straight pipe flow.

5.2. Wall position and friction velocity determination

For determining the the friction velocity, U_τ, one should measure the wall shear stress, τ_{wall}. There are several ways to determine the wall shear stress, τ_{wall}. By mounting pressure tabs in the pipe and measuring the pressure distribution along the pipe, one can use equation (2.31) in order to determine τ_{wall}. One other way is to use oil film interferometry technique. One of the most accurate and reliable way to measure the shear stress is oil film interferometry (OFI) technique. In this technique, oil is applied to the surface of the wind tunnel model. When fluid/air flows over the model surface, the shear stress that develops on the model surface causes the oil to create a thin film (thickness of this film is in the order of microns). When this film is illuminated by the quasi-monochromatic light, it produce interference patterns. If the image of the interference pattern is captured sometime after the flow has started, the spacing between fringes can be related to the shear stress acting on the oil film. Several oil drops or lines can be applied to the model to simultaneously determine shear stress at many locations on the model.

In the present study none of the aforementioned method were utilized due to existing limitations. Here we instead use the mean velocity profiles of non-swirling turbulent pipe flow to obtain friction velocity, u_τ, and also the offset from the wall position. As will be explained in section 5.3.2, the measured data is influenced by near wall effects for close to wall measurements. Neglecting the influenced data, the mean velocity profiles were fitted on the composite profiles of mean velocity of turbulent pipe flow as introduced by Nagib & Chauhan (2008) and explained in section 2.3.1. Using this data, an estimate of both u_τ and offset from the wall position were obtained that give an overall good fit to the data. A better fit of measured data with the composite profile for the near-wall region is presented in appendix A. The curve-fitting procedure was accomplished following different steps illustrated in Örlü *et al.* (2010). Figure 5.1(a) depicts the determined friction velocities according to different

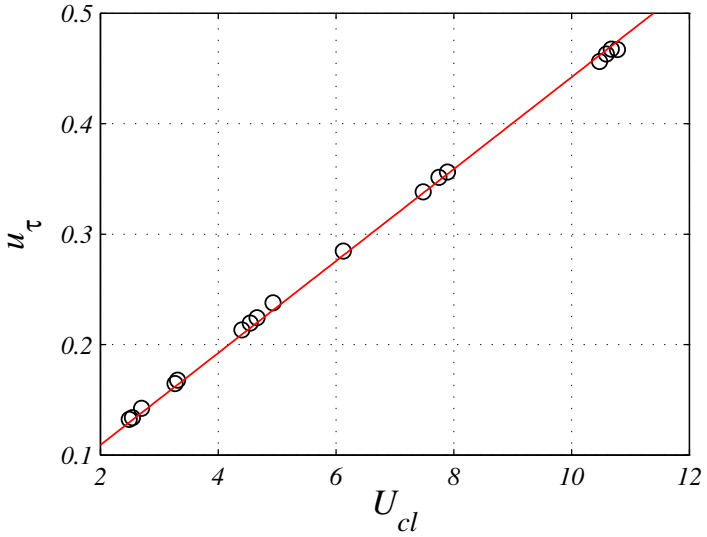

(a) Friction velocity, u_τ, as function of the centerline velocity, U_{cl}.

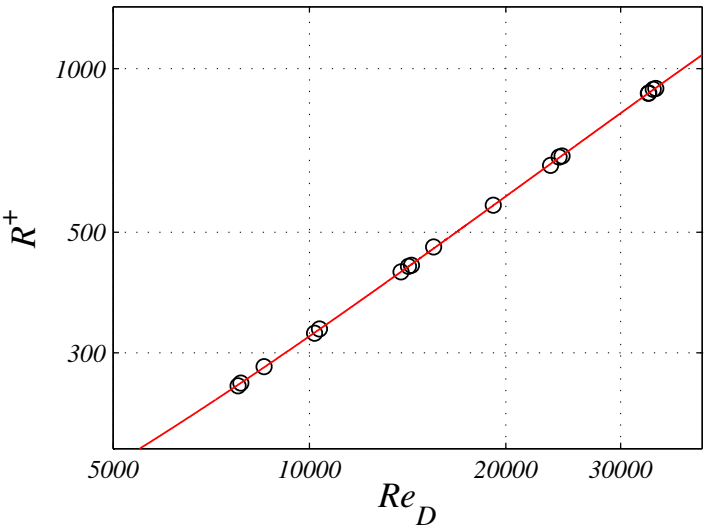

(b) Friction Reynolds number, R^+, as function of Reynolds number based on bulk velocity and pipe diameter, Re_D.

FIGURE 5.1. Symbols denote 17 individual experiments, while the solid lines is a linear and a polynomial fit to the data for (a) and (b) respectively.

measurement cases and centerline velocity, U_{cl}. Friction Reynolds number, R^+, as function of Reynolds number based on bulk velocity and pipe diameter, Re_D, is illustrated in figure 5.1(b).

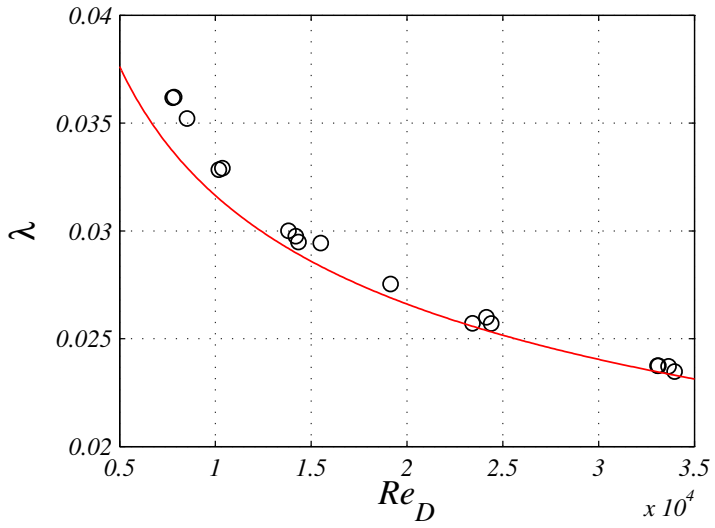

FIGURE 5.2. Friction factor, λ, as function of Reynolds number based on bulk velocity and pipe diameter, Re_D. Symbols denote 17 individual experiments, while the solid line is based on the 1/7th power law by Blasius (1913).

Friction factor, λ, as a function of Reynolds number based on bulk velocity and pipe diameter, Re_D, is shown in figure 5.2. The friction factor is determined through equation (2.35) for measured data. In fully developed smooth turbulent pipe flow, λ is a unique function of Re_D. Assuming a one-seventh power law variation of velocity and using a fit to experimental data, Blasius (1913) obtained,

$$\lambda = \frac{0.3164}{Re_D{}^{0.25}}\,, \tag{5.1}$$

which is depicted in figure 5.2 by the red solid line.

5.3. Results

5.3.1. *Mean velocity profiles*

In this chapter, the results are only presented in the outer scalings. Further analyze of the results in inner scaling is presented in appendix A. Figure 5.3(a) and 5.3(b) show the mean velocity profile in outer-scaling normalized with bulk velocity, U_b, and centerline velocity, U_{cl}, respectively for all 17 measurements. Also, data points that are affected by additional heat losses to the wall are included as gray shaded open circles. Although different wire length and diameter were utilized for different hot-wire probes, according to figure 5.3(a) and 5.3(b), the measured data seem to collapse in a general trend, and the changes in the profiles are $R+$ dependent as illustrated later on this section.

Figure 5.4 illustrates the ratio between the bulk velocity and the centerline velocity as a function of the Reynolds number. As it is shown in this figure, this ratio is approximately 0.8 and increasing slightly with the Reynolds number. The Reynolds number effects on the mean velocity profiles in outer scaling is depicted in figure 5.5. The friction Reynolds number, R^+, is utilized, and the relation between R^+ and Re_D is illustrated in figure 5.1(b) as well as table 1 for each measured case. The L^+ effects is removed in the results shown in this figure. It is observed that more complete mean velocity profiles are obtained as the Reynolds number increases. Figures 5.6 and 5.7 are showing the L^+ effects on the mean velocity profile in outer scaling for $R^+ \approx 420$ and $R^+ \approx 900$ respectively. The results of measurements with four different inner scaled wire lengths are depicted. As mentioned earlier, it is clearly shown that the inner-scaled wire length, L^+, has no effects on mean velocity profiles in outer scaling. The L^+ effect is further discussed in appendix A for mean velocity profiles in inner scaling.

The swirl number, S, effect on the mean velocity profiles at Re_D equal to 24000 is illustrated in figure 5.8. It is observed that by increasing the swirl number the profiles tend toward the parabolic shape of the laminar pipe flow velocity profile. The laminar pipe flow velocity profile is depicted as the red solid line. Figure 5.9 depicts the Reynolds number effect on mean velocity profiles for the case that the swirl number is fixed at $S = 0.5$. In contrary to the results for the non-swirling flow, i.e. figure 5.5, The Reynolds number has no effects on the mean velocity profiles of the swirling cases for the measured Re_D range. This is due to the dominating effect of the swirl on the pipe flow, and is shown in figure 5.10 as well. Figure 5.10 illustrates the effect of swirl on the ratio between bulk velocity and centerline velocity. It is shown that this ratio reduces by increasing the swirl number, and also for $S = 0.5$, i.e. three horizontal filled circles, this ratio is constant for different Re_D which again shows the dominating effect of the swirl on the turbulent pipe flow.

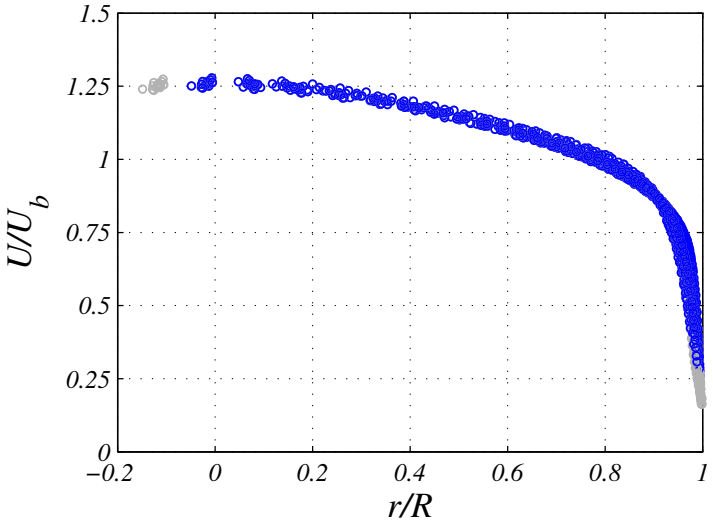

(a) The mean velocity is normalized with bulk velocity, U_b.

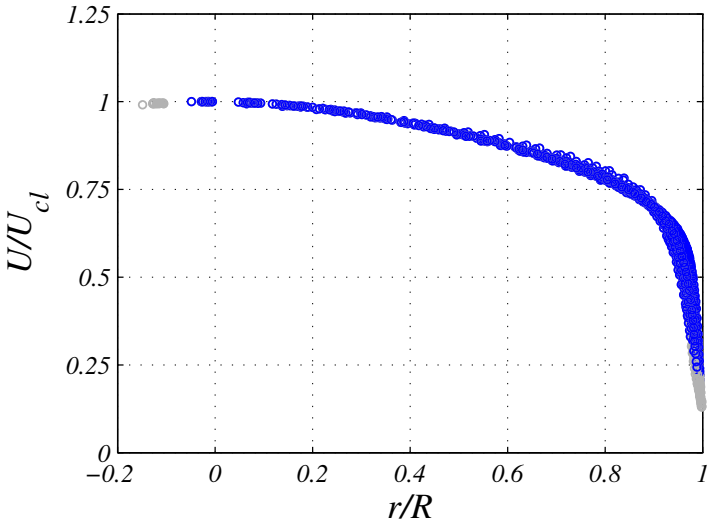

(b) The mean velocity is normalized with centerline velocity, U_{cl}.

FIGURE 5.3. Mean velocity profiles in outer scaling for all 17 measurements for non-swirling turbulent pipe flow. Gray shaded data points denote those measurements, that are affected by additional heat losses to the wall as well as those that correspond to the other half of the pipe cross-section.

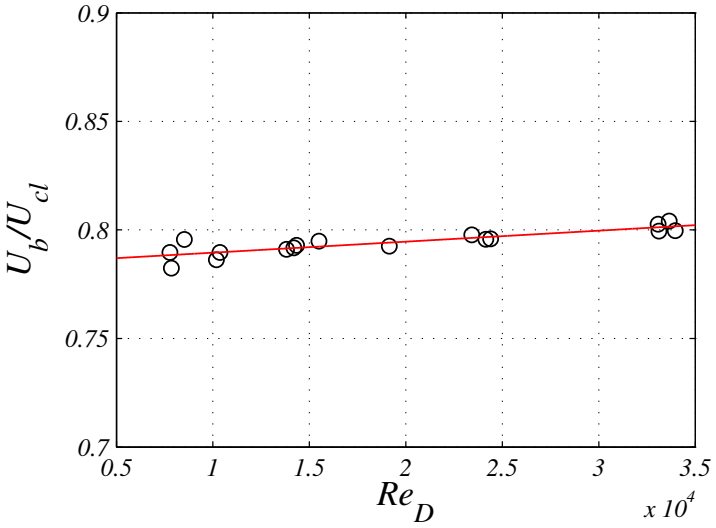

FIGURE 5.4. The ratio between bulk velocity and centerline velocity for different Reynolds numbers. Solid line is linear fit to the data.

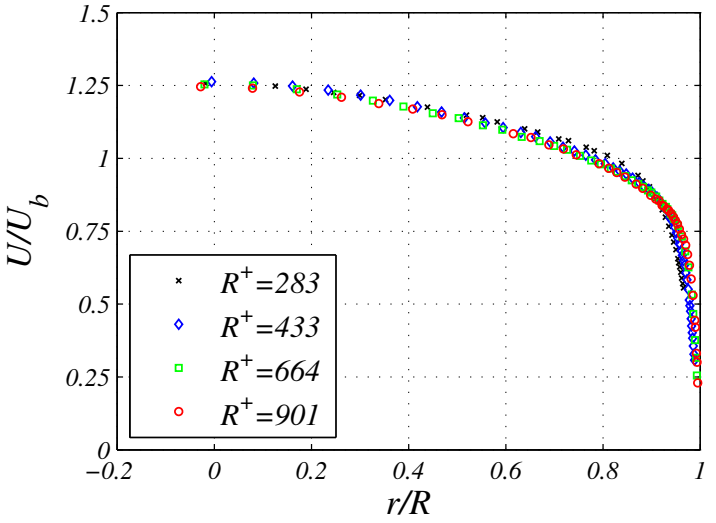

FIGURE 5.5. Mean velocity profiles in outer scaling for different R^+ at fixed inner-scaled wire length, i.e. $L^+ \approx 15$. The mean velocity is normalized with bulk velocity, U_b.

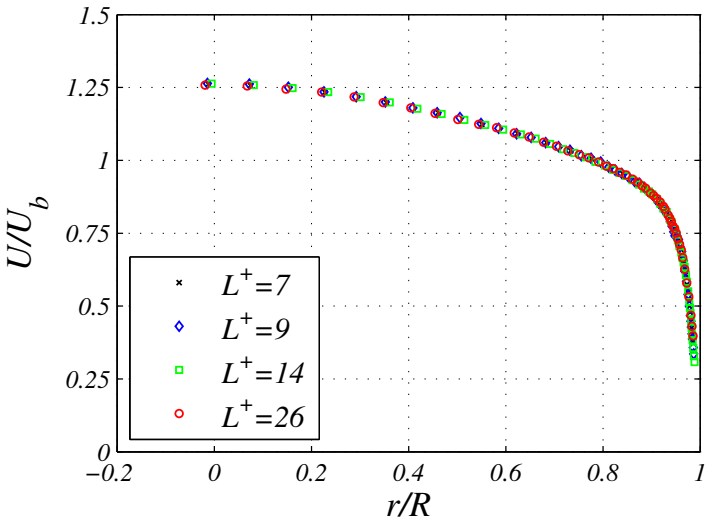

FIGURE 5.6. Mean velocity profiles in outer scaling for different L^+ at $R^+ \approx 420$.

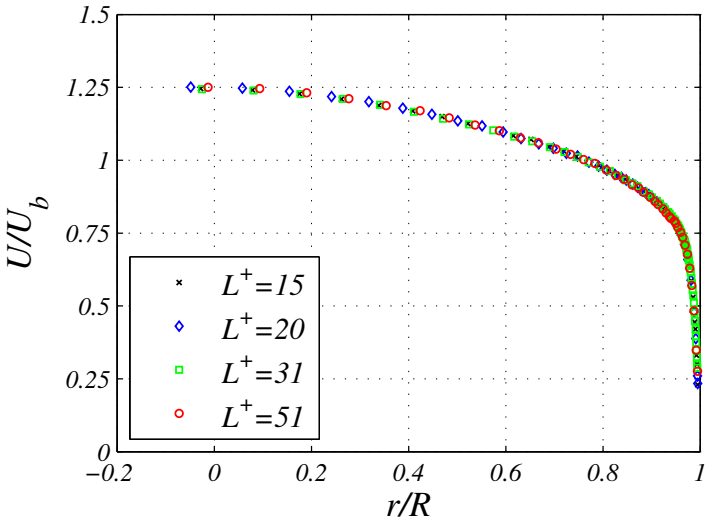

FIGURE 5.7. Mean velocity profiles in outer scaling for different L^+ at $R^+ \approx 900$.

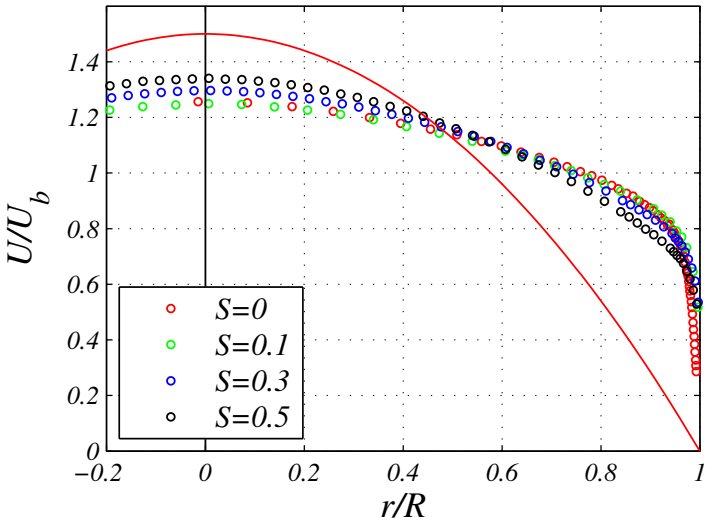

FIGURE 5.8. Mean velocity profiles for different swirl numbers at $Re_D = 24000$. The red solid line indicates the laminar pipe flow velocity profile.

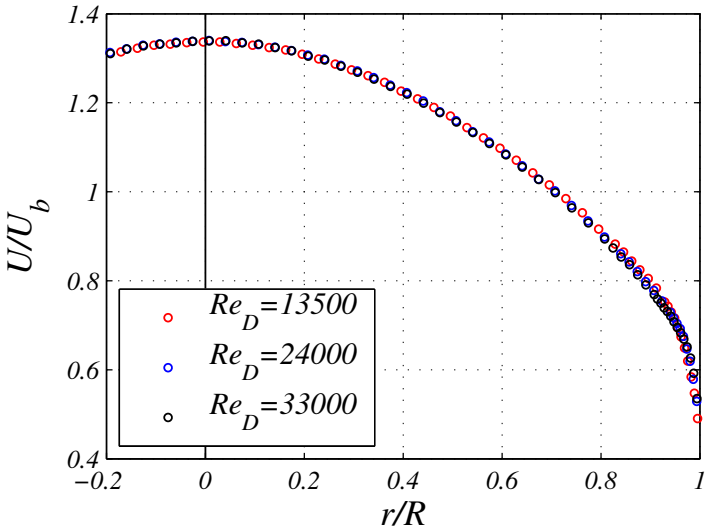

FIGURE 5.9. Mean velocity profiles for different Reynolds numbers at $S = 0.5$.

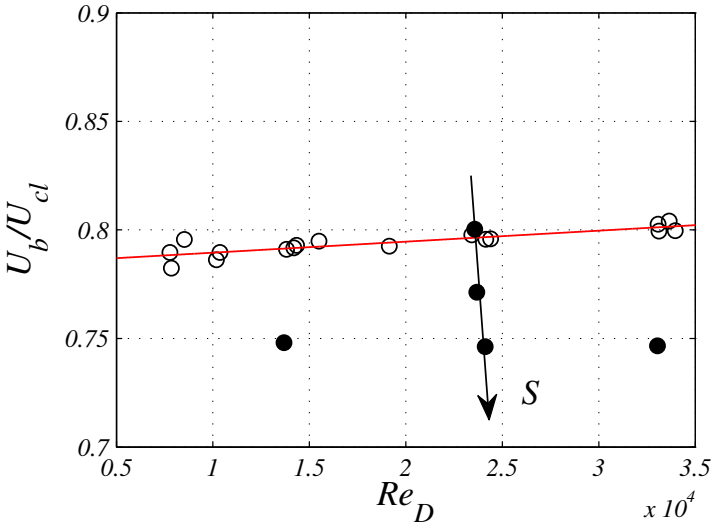

FIGURE 5.10. Swirl effect on the ratio between bulk velocity and centerline velocity. The filled circles represent Swirling pipe flow measurements.

5.3.2. *Turbulence intensity profiles*

Normalized with bulk velocity, U_b, the root mean square of velocity fluctuation, u_{rms}, that for simplification reasons is denoted with u' hereafter, is illustrated in figure 5.11 for all non-swirling measurement cases in outer-scaling. The gray shaded symbols at the right side are the data points affected by conduction heat losses according to near wall measurements, and the ones at the left side are the data points regarding the left half of the pipe diameter, and both are neglected hereafter. The illustrated trend of the profiles shows an increase in u' toward the wall while the mean velocity is decreasing, and a sudden reduction in u' after a peak close to the wall.

The R^+ effect on the root mean square of velocity fluctuation, u', at fixed inner-scaled wire length of $L^+ \approx 15$ is depicted in figure 5.12. As indicated in the figure, the radial position of the peak of u'/U_b goes toward the wall by an increase in R^+. But the trend of u'/U_b seem to be independent of R^+ for r/R less than around 0.7, i.e. outer region. For investigating the effect of inner-scaled wire length, L^+, on the measured data, profiles of u'/U_b in outer-scaling are presented for $R^+ \approx 420$ and $R^+ \approx 900$ in figures 5.13 and 5.14, respectively, for different L^+. It can be inferred from both figures that a higher peak in u'/U_b is obtained by reducing the inner-scaled wire length, L^+. As

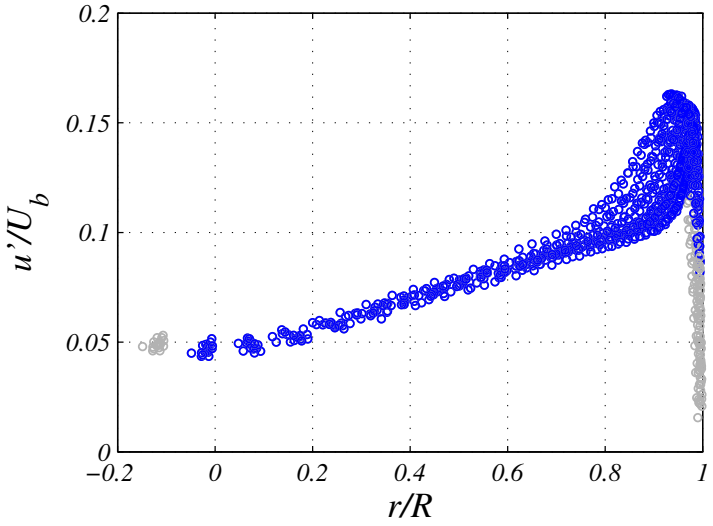

FIGURE 5.11. Profiles of the root mean square of velocity fluctuation, u', normalized with bulk velocity,U_b, in outer scaling for all 17 non-swirling turbulent pipe flow measurements.

for the case of $R^+ \approx 900$ that is depicted in figure 5.14 a wider range of L^+ has been measured, the difference between the captured L^+ is illustrated more clearly. The impact of the viscous scaled hot-wire length, L^+, on the PDF, and hence the higher order moments has been reported by Örlü & Alfredsson (2010) which is in agreement with the results from the present study.

Figure 5.15 shows the swirl number effect on the u'/U_b profiles at $Re_D = 24000$. As depicted, the root mean square of the velocity fluctuations decrease along all the pipe radius by an increase in the swirl number. Hence, this reduction in the turbulence level resembles reaching trend of the swirling pipe flow toward the laminar pipe flow behavior which is similar to the behavior of mean velocity profiles as discussed in figure 5.8. The effect of the Reynolds number on the u'/U_b profiles at $S = 0.5$ is depicted in figure 5.16 which illustrates overlapped profiles of u'/U_b almost in all the pipe radius for the Reynolds numbers equal to 24000 and 33000.

Figure 5.17 illustrates diagnostic plots as introduced by Alfredsson & Örlü (2010) (i.e. the profiles of root mean square of velocity fluctuations, u', against the local mean velocity, U, and both are normalized with the centerline velocity, U_{cl}) for all the measurement cases of non-swirling fully developed turbulent pipe flow. The grey point at the left side are the measured data affected by

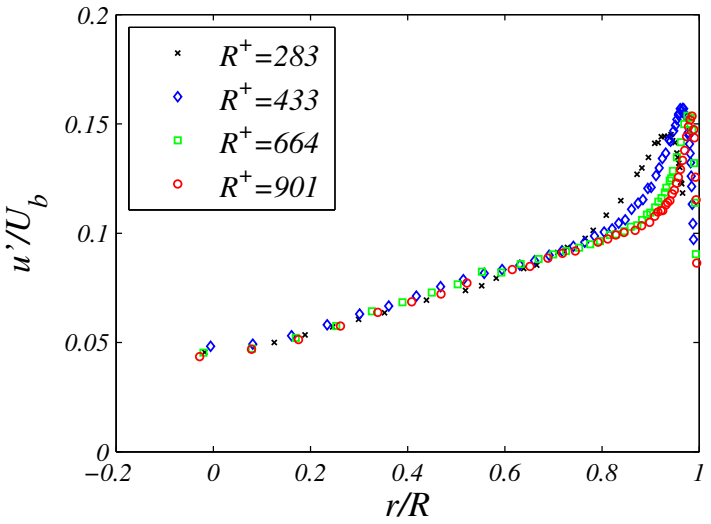

FIGURE 5.12. Profiles of the root mean square of velocity fluctuation, u', normalized with bulk velocity,U_b, in outer scaling for different R^+ at fixed inner-scaled wire length, i.e. $L^+ \approx 15$.

additional heat losses. As depicted in the figure, the profiles are overlapping in the outer region, i.e. the right side, as the local mean velocity, U, is reaching the centerline velocity, U_{cl}, which shows the pipe flow is fully developed. The Reynolds number dependency of the diagnostic plots for a fixed inner-scaled wire length of $L^+ \approx 15$ is shown in figure 5.18. As illustrated, the corresponding local mean velocity, U, to the maximum value of u' is decreasing for higher R^+. The spatial resolution effect on the measured data is illustrated for diagnostic plots in figures 5.19 and 5.20, and as discussed for the turbulence intensity profiles, higher u' is captured by reducing L^+. For the swirling cases, the reduction of the turbulence level throughout the whole pipe radius with an increase in the swirl number is depicted in figure 5.21 in diagnostic plots. One should take this into consideration that by increasing the swirl number the centerline velocity, U_{cl}, is increasing and simultaneously the root mean square of the velocity fluctuations is decreasing which explains the considerable deviations between the diagnostic plot in figure 5.21. The Reynolds number effects on the diagnostic plots for a fixed swirl number equal to 0.5 is demonstrated in figure 5.22.

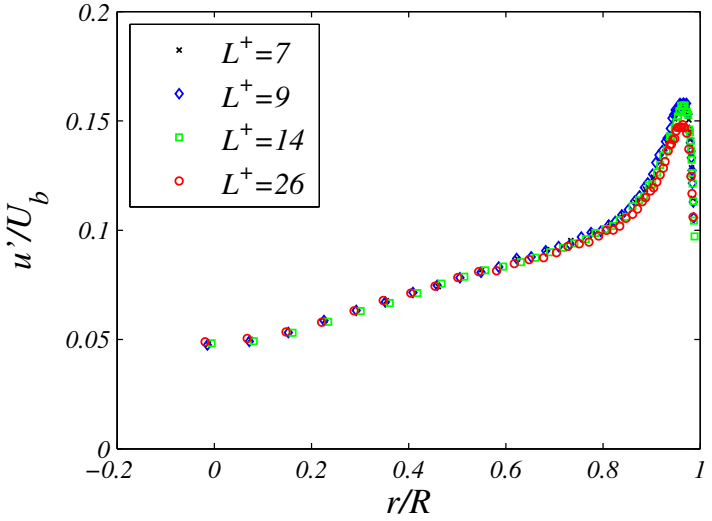

FIGURE 5.13. Profiles of the root mean square of velocity fluctuation, u', normalized with bulk velocity,U_b, in outer scaling for different L^+ at $R^+ \approx 420$.

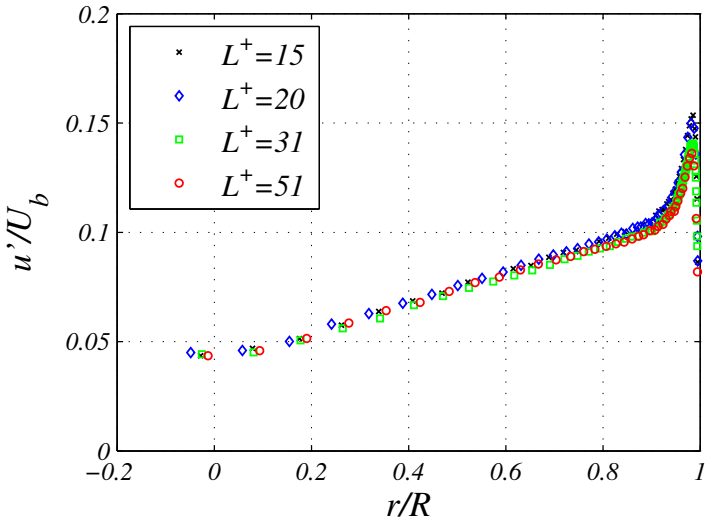

FIGURE 5.14. Profiles of the root mean square of velocity fluctuation, u', normalized with bulk velocity,U_b, in outer scaling for different L^+ at $R^+ \approx 900$.

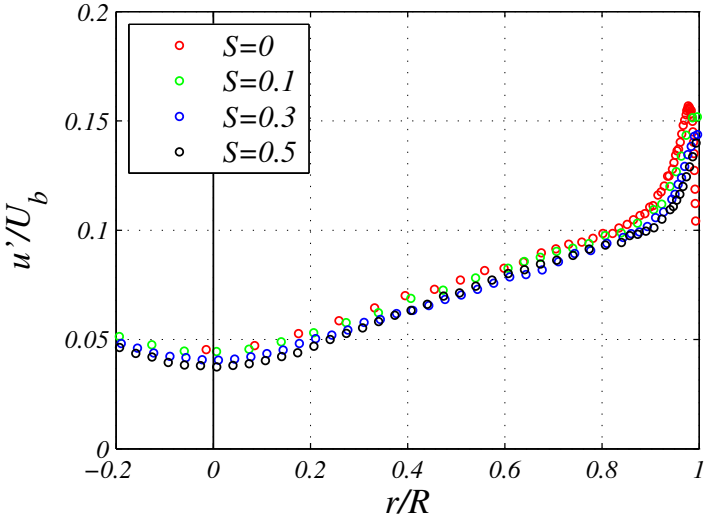

FIGURE 5.15. Swirl number effect on the root mean square of velocity fluctuation, u', normalized with bulk velocity,U_b, normalized by bulk velocity, U_b, for $Re_D = 24000$.

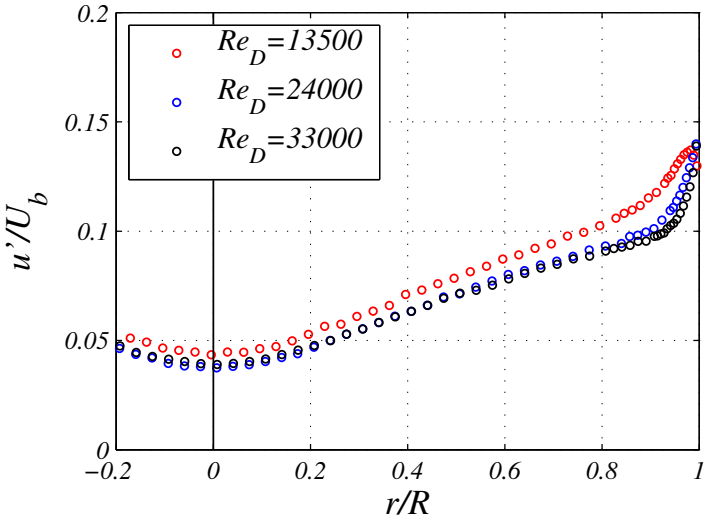

FIGURE 5.16. Reynolds number effect on he root mean square of velocity fluctuation, u', normalized by bulk velocity, U_b, for $S = 0.5$.

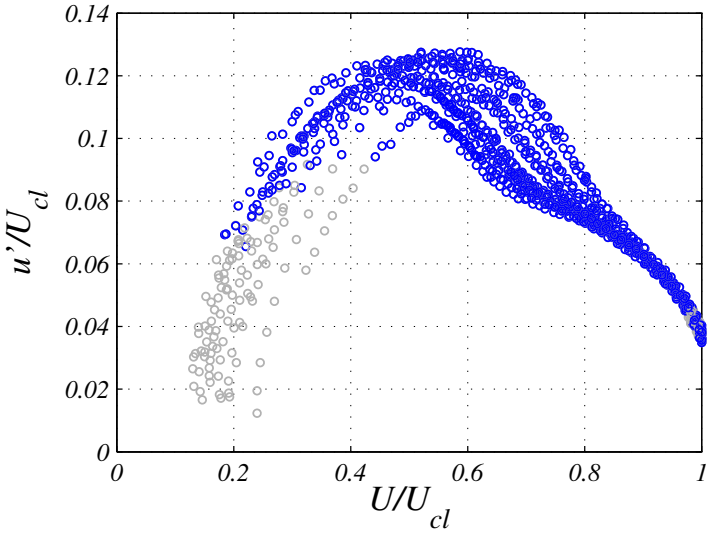

FIGURE 5.17. Mean velocity and the turbulence intensity in the diagnostic plot for all 17 measurements.

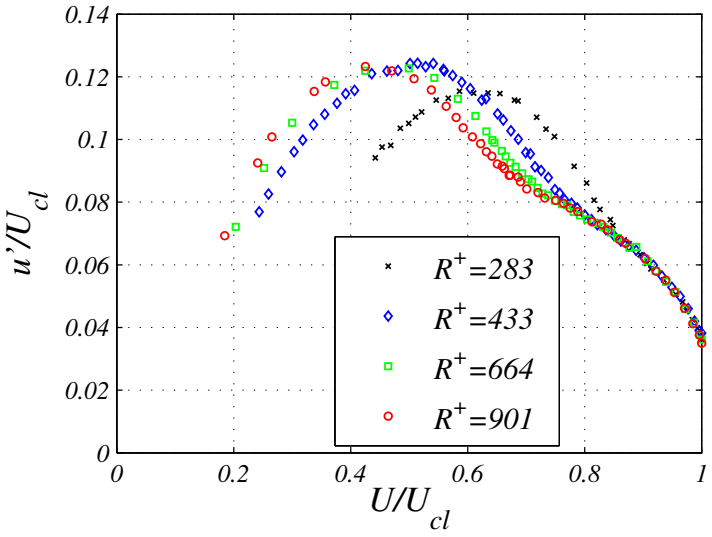

FIGURE 5.18. Mean velocity and the turbulence intensity in the diagnostic plot for different R^+ at fixed inner-scaled wire length, i.e. $L^+ \approx 15$.

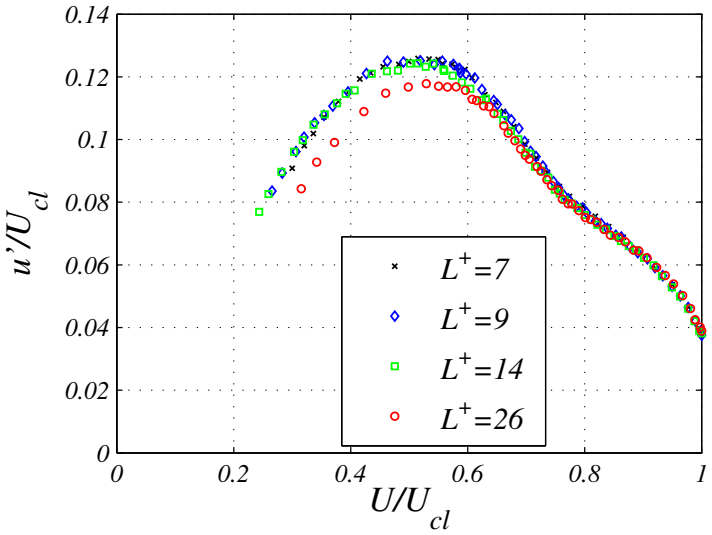

FIGURE 5.19. Mean velocity and the turbulence intensity in the diagnostic plot for different L^+ at $R^+ \approx 420$.

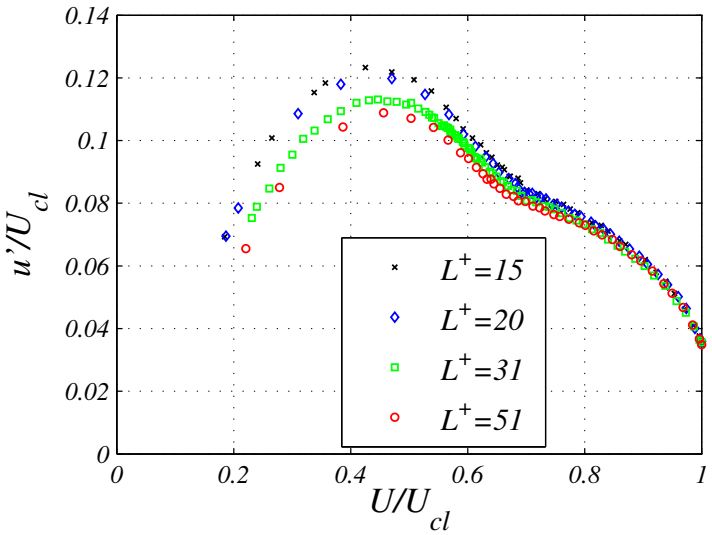

FIGURE 5.20. Mean velocity and the turbulence intensity in the diagnostic plot for different L^+ at $R^+ \approx 900$.

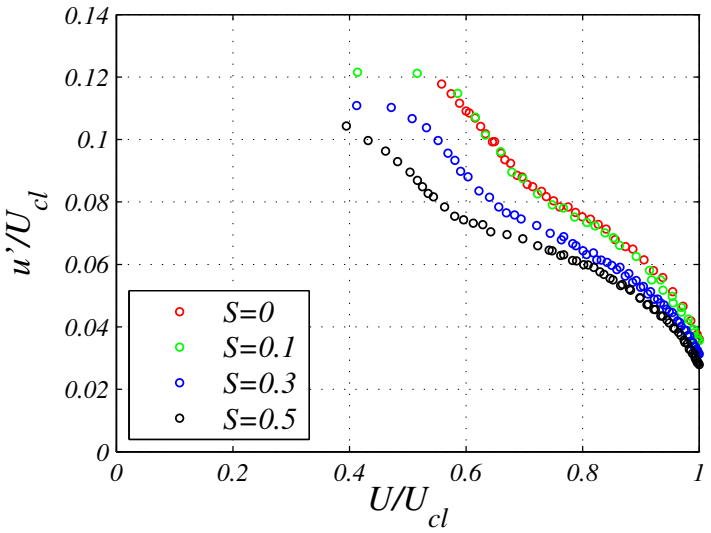

FIGURE 5.21. Mean velocity and turbulence intensity in the diagnostic plot for different swirl numbers at $Re_D = 24000$.

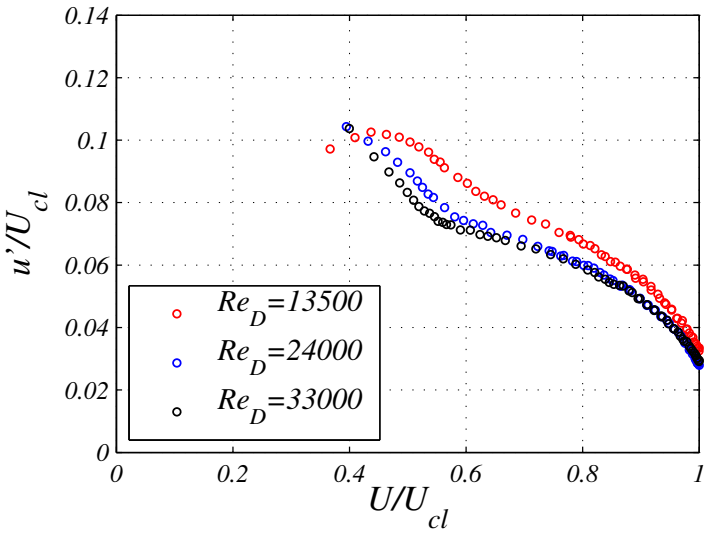

FIGURE 5.22. Mean velocity and turbulence intensity in the diagnostic plot for different Reynolds numbers at $S = 0.5$.

5.3.3. *Higher order moments*

The evolution of the skewness and the flatness along the pipe radius for the non-swirling and swirling turbulent pipe flow measurements are demonstrated in this section. The Reynolds number effects at both fixed inner-scaled wire length and swirl number as well as spatial resolution and swirling effects at fixed Reynolds number are presented. Figure 5.23 illustrates the Reynolds

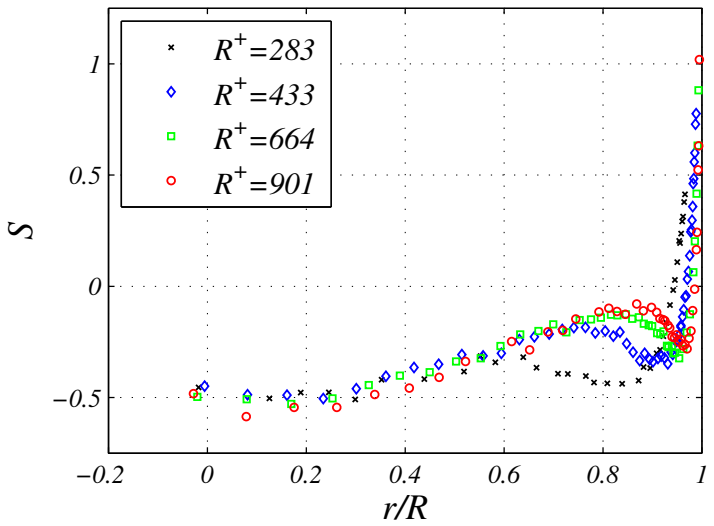

FIGURE 5.23. Skewness values in outer scaling for different Re_τ.

number dependecy of the skewness distributions for $L^+ \approx 15$. As depicted in the figure, the value of the peak in the skewness profiles at the inner region decreasing while the Reynolds number increases. Also it can be observed from the figures 5.24 and 5.25 that by reducing L^+ the captured value of the peak in the inner region is increasing. On the other hand, as depicted in figure 5.26, swirling motion has a different effect on the skewness distribution and decreases the value of the peak in the inner region in the skewness profiles. The Reynolds number effects on the skewness profiles at fixed swirl number equal to 0.5 is depicted in figure 5.27. The same behavior as the skewness distributions is observed for the flatness distributions. The Reynolds number dependency of the flatness profiles along the pipe radius is illustrated in figure 5.28 for $L^+ \approx 15$, and the spatial resolution effects at $R^+ \approx 480$ and $R^+ \approx 900$ are demonstrated in figures 5.29 and 5.30, respectively. The swirl number effect at $Re_D = 24000$ is depicted in figure 5.31, and the Reynolds number effect at $S = 0.5$ in figure 5.32.

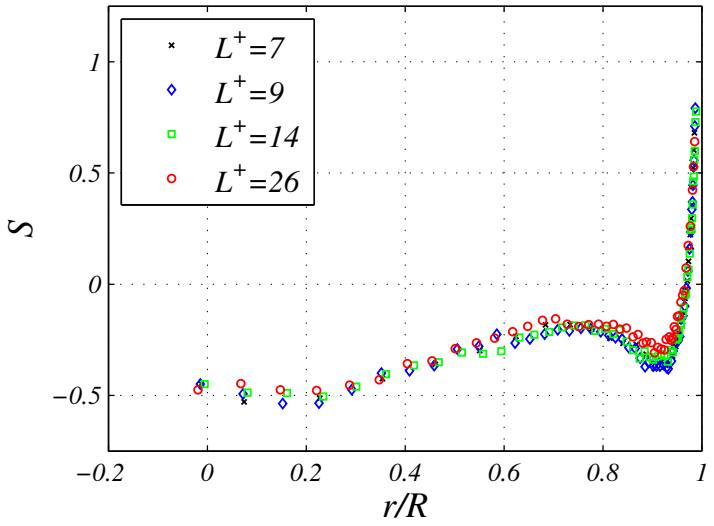

FIGURE 5.24. Skewness values in outer scaling for different L^+ and Re_τ equal to 480.

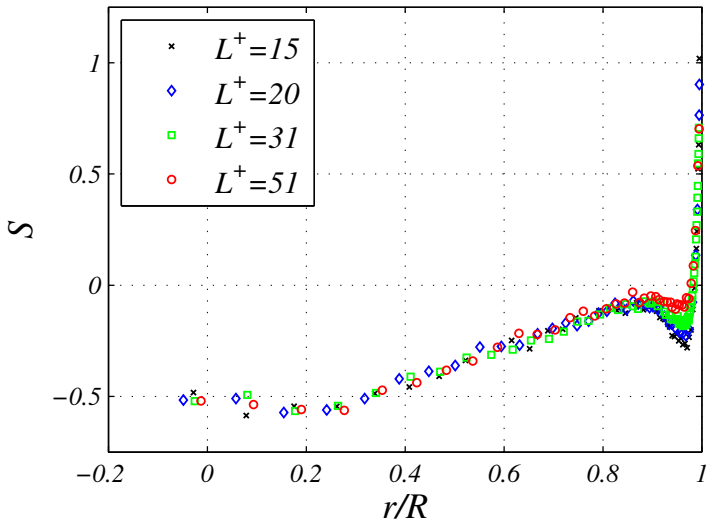

FIGURE 5.25. Skewness values in outer scaling for different L^+ and Re_τ equal to 900.

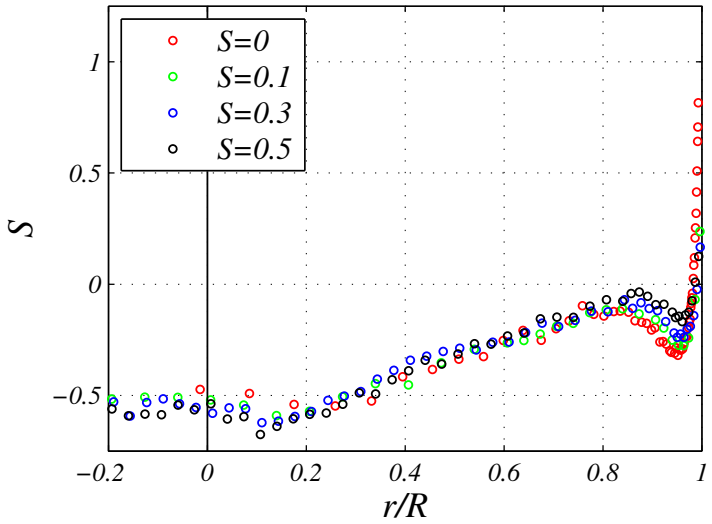

FIGURE 5.26. Swirl number effect on skewness distributions for $Re_D = 24000$.

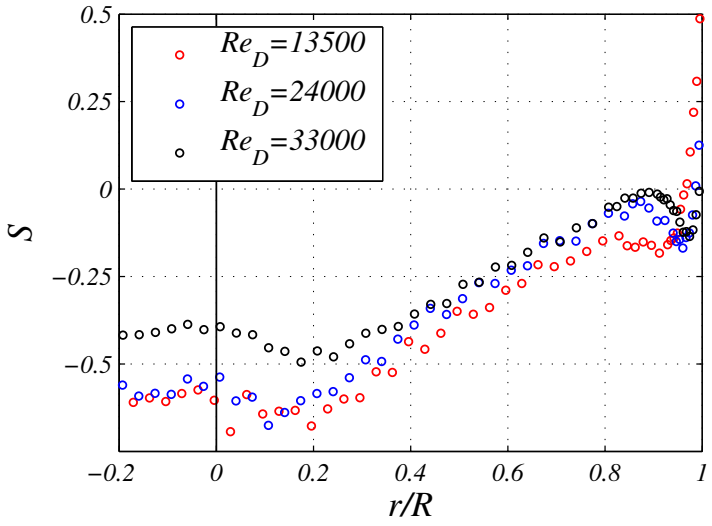

FIGURE 5.27. Reynolds number effect on skewness distributions for $S = 0.5$.

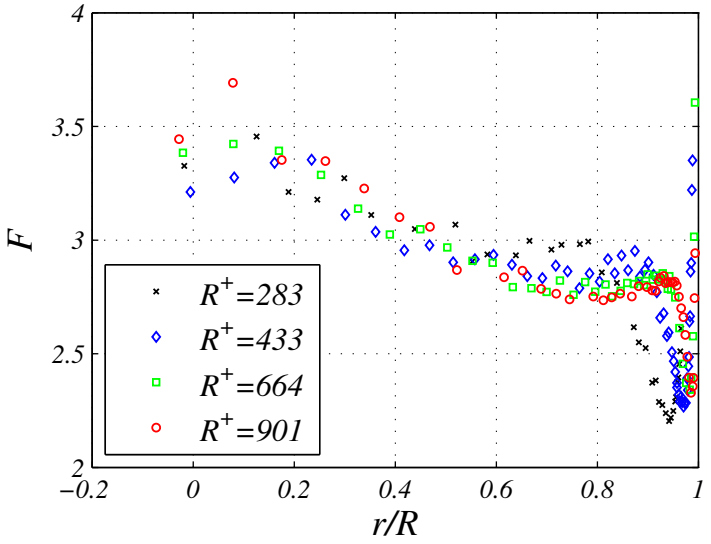

FIGURE 5.28. Flatness values in outer scaling for different Re_τ.

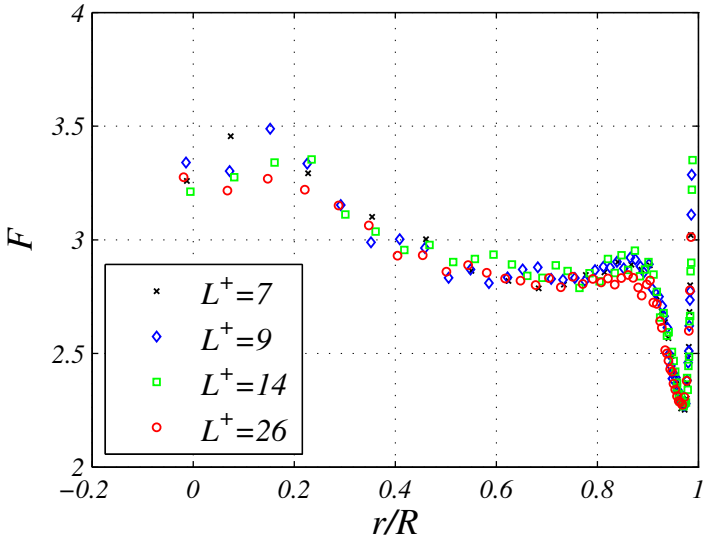

FIGURE 5.29. Flatness values in outer scaling for different L^+ and Re_τ equal to 480.

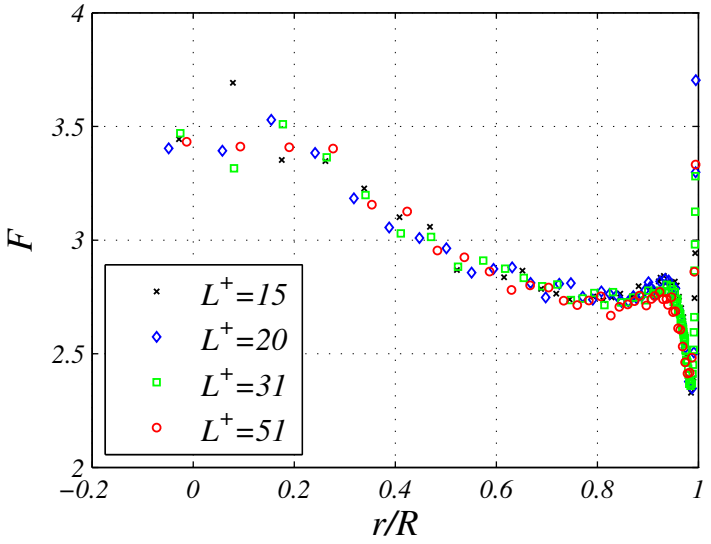

FIGURE 5.30. Flatness values in outer scaling for different L^+ and Re_τ equal to 900.

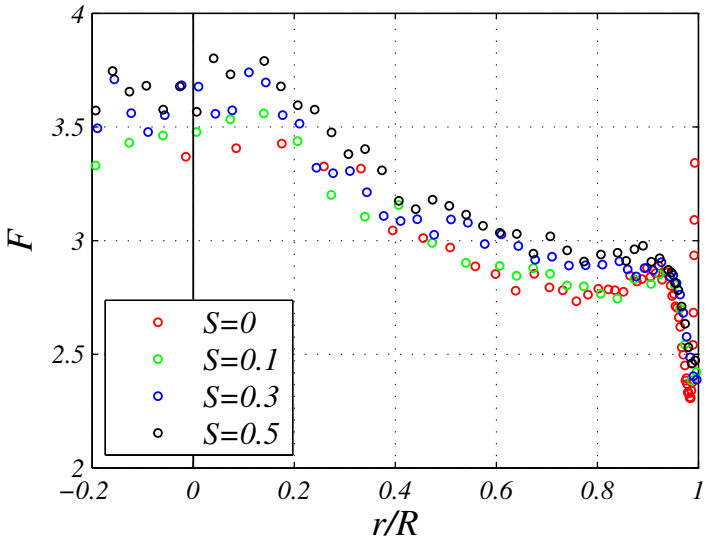

FIGURE 5.31. Swirl number effect on flatness distributions for $Re_d = 24000$.

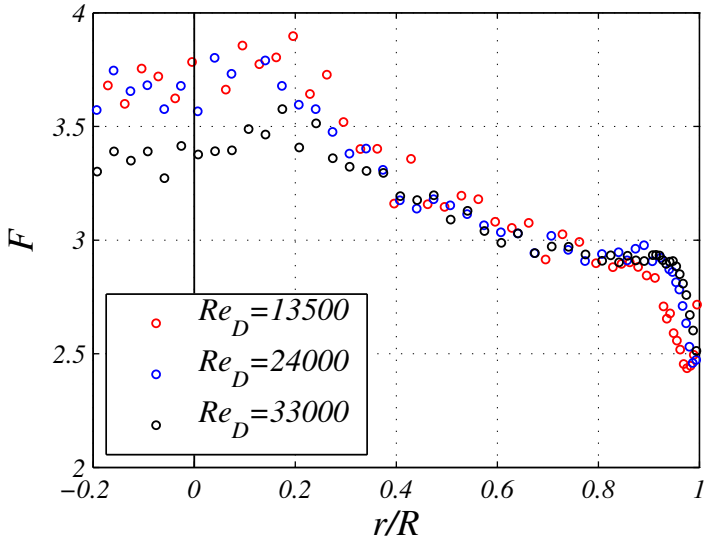

FIGURE 5.32. Reynolds number effect on flatness distributions for $S = 0.5$.

5.3.4. *Probability density function (PDF) maps*

The probability density function (PDF) distribution along the pipe radius is demonstrated through PDF contour plots for both non-swirling and swirling turbulent pipe flows in figures 5.35 and 5.36 respectively. The figures are illustrating the PDF distributions throughout the pipe radial direction at $Re_D = 24000$ and for swirl number equal to 0 and 0.5 respectively. In order to comprehend the PDF contour plots more clearly, the PDF diagrams in $2D$ plots for both non-swiriln and swirling cases at different radial positions are depicted in figure 5.33. The solid lines are denoting the non-swirling case while the dashed lines are denoting the swirling case. The vertical axis in figure 5.33 is showing the PDF values, as depicted in the color bars in figures 5.35 and 5.36, multiplied by the bulk velocity, U_b. The velocity distribution normalized the bulk velocity, u/U_b, depicted in the horizontal axis in figure 5.33 is the vertical axis in the contour plots, and the black solid lines in the PDF contour plots demonstrate the mean velocity profiles. As illustrated in figures 5.35 and 5.36, the swirling motion reduces the fluctuation level in the pipe core, and this reductio is smoothly extended throughout the whole pipe radius. PDF diagrams scaled by root mean square of the velocity fluctuations, u', are deppicted in figure 5.34 for all the cases presented in figure 5.33. It is shown that the PDF diagrams for both non-swirling and swirling cases for different radial position along the pipe radius overlap when scaled by u'.

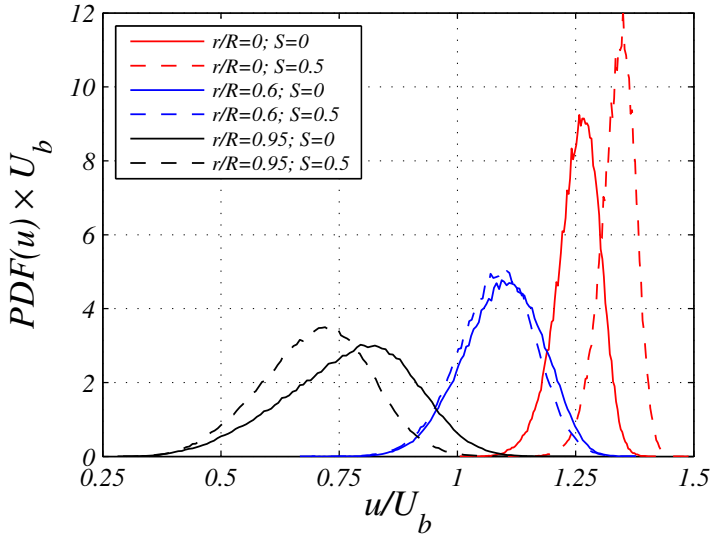

FIGURE 5.33. PDF diagrams scaled by U_b at different radial position of the straight pipe exit for $Re_D = 24000$.

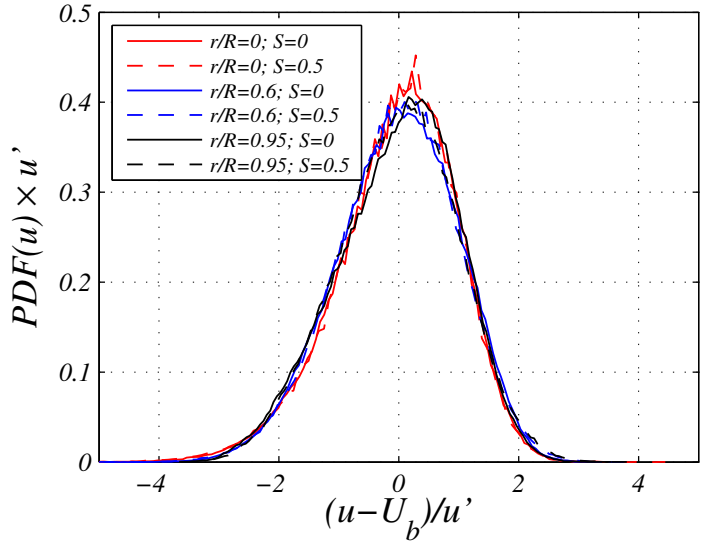

FIGURE 5.34. PDF diagrams scaled by u' at different radial position of the straight pipe exit for $Re_D = 24000$.

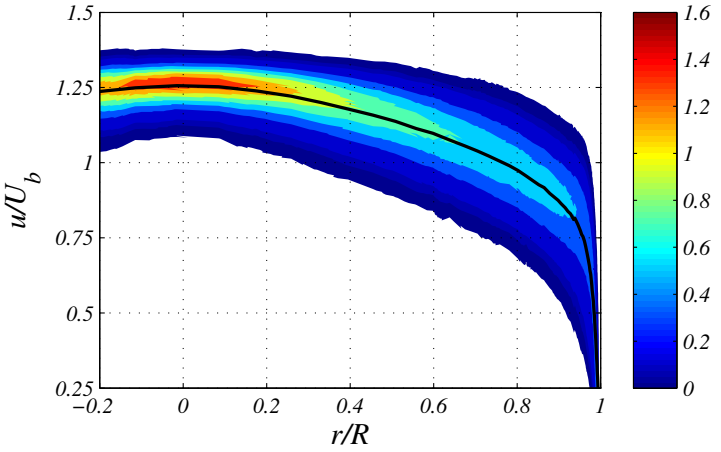

FIGURE 5.35. Contours of PDF distributions along cross stream horizontal line at the straight pipe exit for $Re_D = 24000$ and $S = 0$.

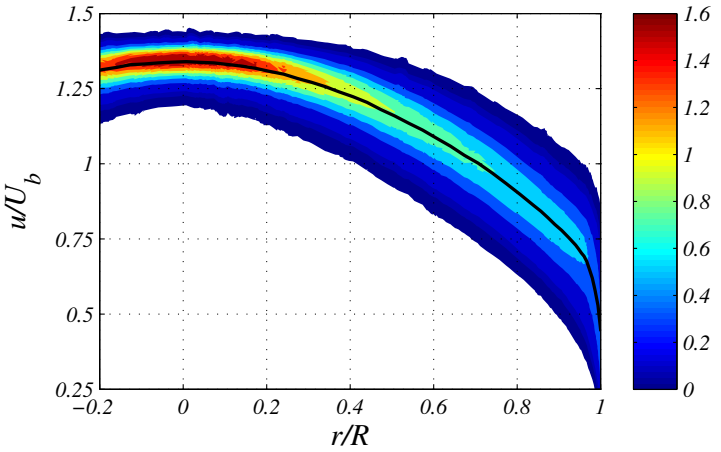

FIGURE 5.36. Contours of PDF distributions along cross stream horizontal line at the straight pipe exit for $Re_D = 24000$ and $S = 0.5$.

5.3.5. *Autocorrelation function maps*

The evolution of the autocorrelation functions along the pipe radius is depicted in figure 5.37 in $2D$ plots for the three radial positions depicted in figure 5.33. Contour plots of the evolution of autocorrelation function throughout the whole pipe radius are illustrated in figures 5.38 and 5.39 for swirl number equal to 0 and 0.5 respectively at $Re_D = 24000$. The color bars in the contour plots are showing the value of the autocorrelation functions, R_{uu}, for each radial position along the pipe radius which is the vertical axis of the $2D$ autocorrelation plots in figure 5.37. Note that the time lags, τ, in the $2D$ plot and the contour plots are second and millisecond respectively. As depicted in figure 5.37 the

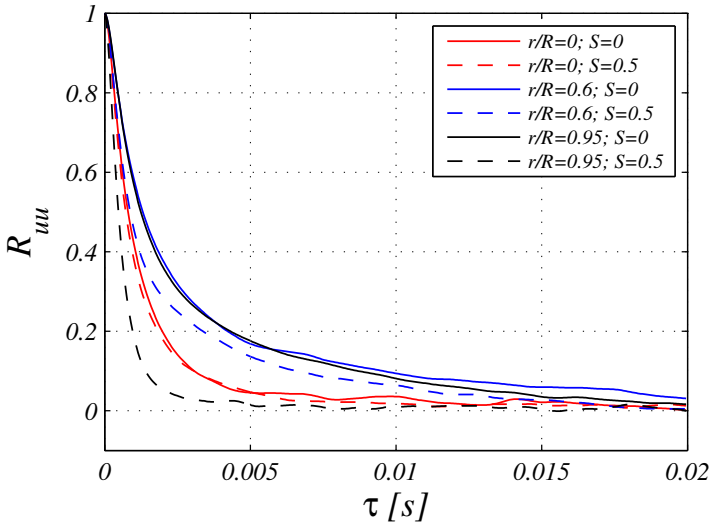

FIGURE 5.37. Autocorrelation diagrams at different radial position of the straight pipe exit for $Re_D = 24000$.

integral time scale, Λ_t (defined in equation (2.19)), for the non-swirling case is increasing by reaching the pipe wall. The growth in the integral time scales along the pipe radius for the non-swirling case is depicted more clearly in figure 5.38. On the other hand, according to the $2D$ and the contour plots of autocorrelation function for the swirling case, the growth of the integral time scales is not consistent through all the pipe radius and starts to decrease for r/R greater than around 0.6 for the swirling case. This reduction continues toward the pipe wall, therefore, the integral time scales near the pipe wall in the swirling cases have a considerable low values in contrary to the non-swirling cases.

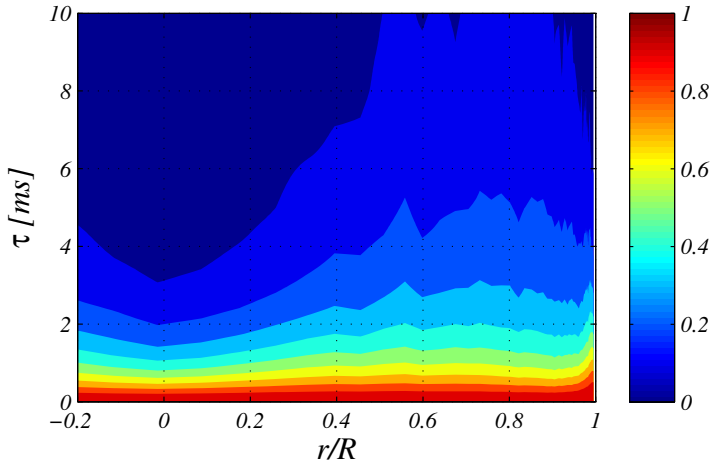

FIGURE 5.38. Contours of autocorrelation distributions along cross stream horizontal line at the straight pipe exit for $Re_D = 24000$ and $S = 0$.

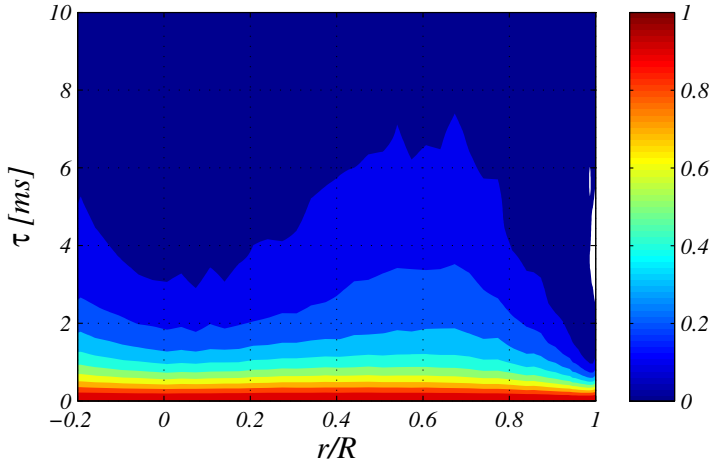

FIGURE 5.39. Contours of autocorrelation distributions along cross stream horizontal line at the straight pipe exit for $Re_D = 24000$ and $S = 0.5$.

5.3.6. *Power-spectral density (PSD) function maps*

The pre-multiplied power spectral density (PSD) functions at three different radial positions along the pipe radius are depicted in $2D$ plot for both non-swirling and swirling cases at $Re_D = 24000$ in figure 5.40. Note that the averaging overlapped spectra for discrete blocks, *Welch*'s average, is used to smooth the estimate for the power spectral density functions. The evolution of the pre-miltiplied power spectral density functions along all pipe radius is illustrated through contour plots in figures 5.41 and 5.42 for swirl number equal to 0 and 0.5 respectively. The color bars in the contour plots are illustrating the PSD function values at each radial position which is the vertical axis in the $2D$ plot of the pre-multiplied PSD functions. It can be observed from figure 5.40

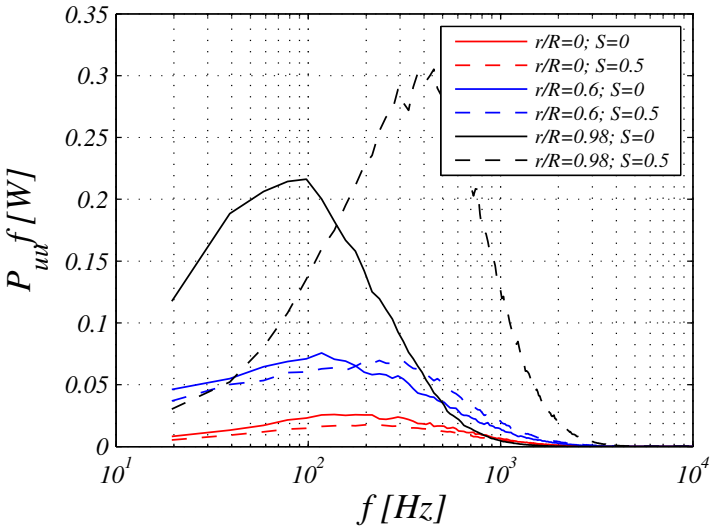

FIGURE 5.40. Pre-multiplied spectra diagrams at different radial position of the straight pipe exit for $Re_D = 24000$.

that by reaching the the pipe wall the peak value of the PSD function is increasing for both non-swirling and swirling cases. But the growth in the peak values and the corresponding frequencies are greater in the swirling cases. The aforementioned growth in the peak values and the corresponding frequencies for the swirling case is demonstrated more clearly in the PSD contour plots for the region near the pipe wall. On the other hand, as depicted in the $2D$ and the contour plots, the peak value of PSD function in the core region is lower for the swirling cases compared to the non-swirling cases.

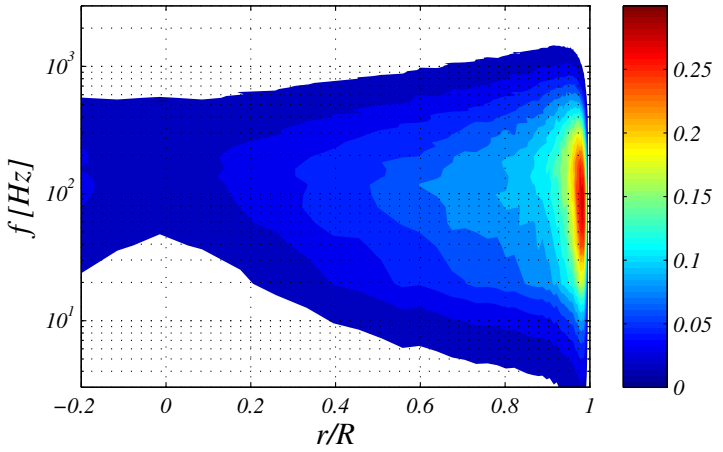

FIGURE 5.41. Contours of power-spectral density distributions along cross stream horizontal line at the straight pipe exit for $Re_D = 24000$ and $S = 0$.

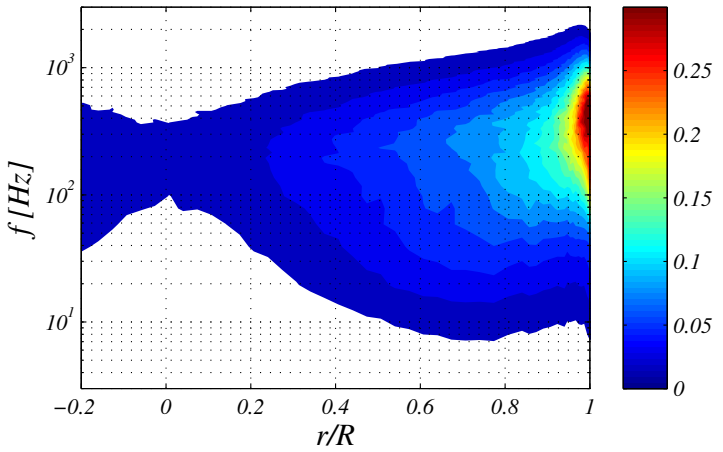

FIGURE 5.42. Contours of power-spectral density distributions along cross stream horizontal line at the straight pipe exit for $Re_D = 24000$ and $S = 0.5$.

CHAPTER 6

Bend pipe flow

6.1. Measurement matrix

In order to investigate the behavior of the flow into the bend pipes, hot-wire measurements were conducted. For this purpose, a 90° circular-section bend was mounted at the straight pipe exit. The diameter of the bend pipe was the same as the diameter of the straight pipe in the rotating pipe facility (i.e. 60 mm). The pipe to mean-bend-curvature radius ratio, α, was 0.43. Hot-wire measurements were obtained for both swirling and non-swirling inlet condition into the bend section as well as for different Reynolds numbers equal to 13500, 24000 and 33000. The corresponding Dean numbers to the aforementioned Reynolds numbers are 6350, 10900, and 15450 respectively. The Reynolds number were adjusted with respect to the mass flow meter calibration curve depicted in figure 4.12. The effect of different swirl numbers on the flow behavior were also investigated for swirl numbers equal to 0.1, 0.3 and 0.5. The 90° bend section had straight tangential extensions of 0.5D at both ends where D represents pipe diameter. The 0.5D extension located upstream of the mounted bend section has no effect on the inlet condition of the bend section for the non-swirling measurements. On the other hand, for the swirling cases, this extension might affect the inlet condition of the bend section since the exiting swirling flow from rotating pipe facility is going through a non-rotating straight pipe of the length of 0.5D before entering the pipe section. However, this effect can be negligible especially for swirl numbers equal to 0.3 and 0.5. The outlet extension of the bend section was desirable in order to investigate the re-stabilizing effect of the pipe extensions after bend section on the so-called *Dean vortices*. In addition, another 1D extension was also mounted after the existing 0.5D extension to monitor these effects slightly more. Figure 6.1 is illustrating the bend pipe mounted at the outlet of the straight pipe with the 1D extension at the outlet of it. The hot-wire measurements were performed along the horizontal line passing the pipe centerline. The radial position are denoted by r and have positive values in the inner region of the pipe and visa versa. Also, the effect due to the 1D extension at the bend outlet on the upstream flow was investigated by measuring 0.5D downstream the bend outlet for both cases of with and without 1D extension. All the experiments regarding to investigating the flow into the bend circular-sectioned pipe were performed

with the same hot-wire probe. Table 3 illustrates all the measured cases. In this table, the downstream position from the bend outlet and the extension length are denoted by x' and $L_{ext.}$ respectively.

FIGURE 6.1. The bend pipe with 1D extension mounted on the straight pipe outlet.

6.2. Results

6.2.1. *Mean velocity profiles*

Both swirling and non-swirling inlet conditions were examined as inlet conditions of the flow into the bend section. Figures 6.2 and 6.3 illustrate mean velocity profiles of the turbulent non-swirling pipe flow into the 90° bend for different Reynolds numbers at 0.5D and 1.5D downstream of the bend exit in the tangential extension respectively. The negative r values represent the outer part of the bend, and the mean velocity is normalized with bulk velocity, U_b. Velocity acceleration is depicted at the outer part of the bend as expected. It can also be inferred that by decelerating and accelerating affects at the outer and the inner parts of the bend respectively, the flow tends to recover its fully developed shape while the Reynolds number is increasing. Hence, it can be conjectured for higher values of the Reynolds number that pipe curvature affects are reducing. Since only one pipe to mean-bend-curvature radius ratio was utilized, the *Dean numbers* effects are correspondence to the Reynolds number effect. The utilized Dean numbers in present study are 6350, 10900, and 15450. Compared to mean velocity profiles at 0.5D downstream of the bend

Case	U_b $[ms^{-1}]$	Re_D [−]	De [−]	S [−]	x'/D [−]	$L_{ext.}/D$
A_1	3.49	13 960	6 350	0	1.5	1.5
A_2	6.02	24 010	10 920	0	1.5	1.5
A_3	8.63	33 950	15 440	0	1.5	1.5
A_4	6.05	23 980	10 910	0.1	1.5	1.5
A_5	6.09	24 010	10 920	0.3	1.5	1.5
A_6	6.10	23 970	10 900	0.5	1.5	1.5
A_7	3.56	13 970	6 350	0.5	1.5	1.5
A_8	8.70	34 050	15 490	0.5	1.5	1.5
B_1	3.53	13 960	6 350	0	0.5	1.5
B_2	6.07	23 970	10 900	0	0.5	1.5
B_3	8.61	34 010	15 470	0	0.5	1.5
C_1	3.53	14 020	6 380	0	0.5	0.5
C_2	6.03	23 950	10 890	0	0.5	0.5
C_3	8.56	33 960	15 450	0	0.5	0.5
C_4	6.07	24 050	10 940	0.1	0.5	0.5
C_5	6.07	24 040	10 930	0.3	0.5	0.5
C_6	6.07	24 030	10 930	0.5	0.5	0.5

TABLE 3. Experimental parameters for present hot-wire measurements of turbulent bend pipe flow.

exit in figureres 6.2, it can be observed in figure 6.3 that at 1.5D downstream of the bend exit flow has already started the process of re-stabilizing. The low velocity region in the inner part of the bend exit is accelerating, and the mean velocity profiles are therefore tending to shape like the normal turbulent mean velocity profiles. This re-stabilizing process is due to the break down of the Dean vortices in the downstream tangent and would take up to more than 18D downstream of the bend exit as reported by Anwer *et al.* (1989). The effect of downstream distance from the bend pipe on the mean velocity profiles for non-swirling case is depicted more clearly in figure 6.4. A considerable remaining issue is to investigate if the downstream conditions applied by the extra tangential extension would affect the flow at the bend exit. In order to examine the existence of the aforementioned effect, measurements were performed at 0.5D downstream of the bend exit in the tangential extension for both cases of with and without the 1D extra extension. The results are depicted in figure 6.5, and illustrate that the flow is not feeling the downstream conditions in the tangential extension after bend exit.

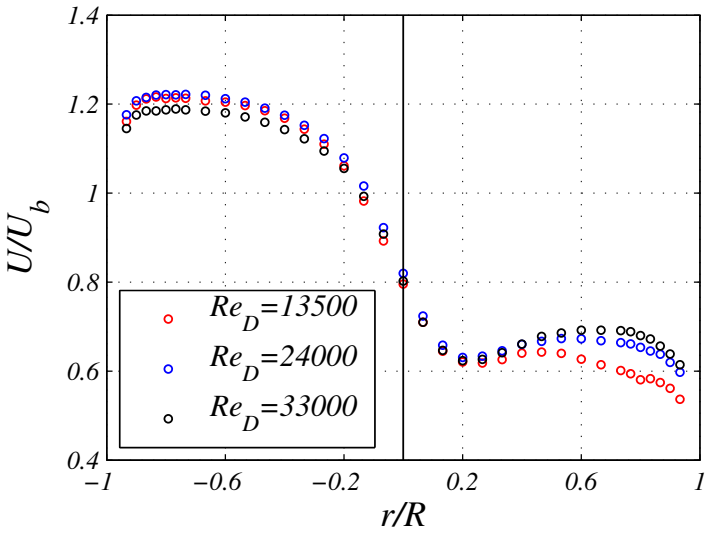

FIGURE 6.2. Reynolds number effect on mean velocity profile of bend pipe flow at 0.5D downstream of the bend exit.

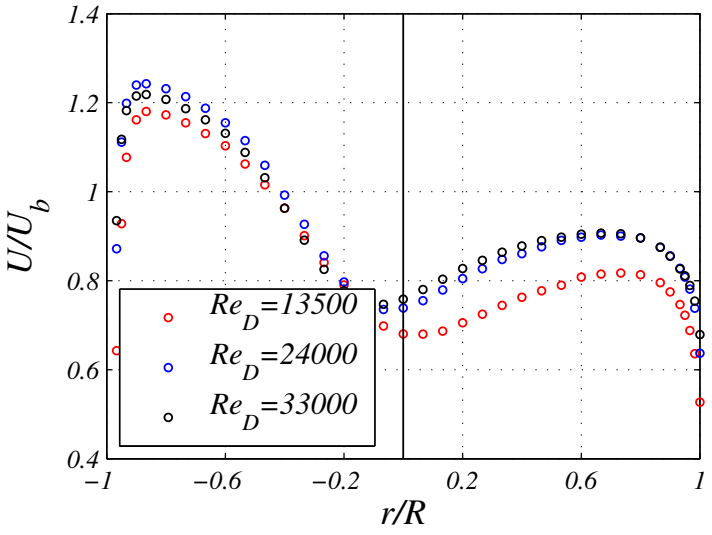

FIGURE 6.3. Reynolds number effect on mean velocity profile of bend pipe flow at 1.5D downstream of the bend exit.

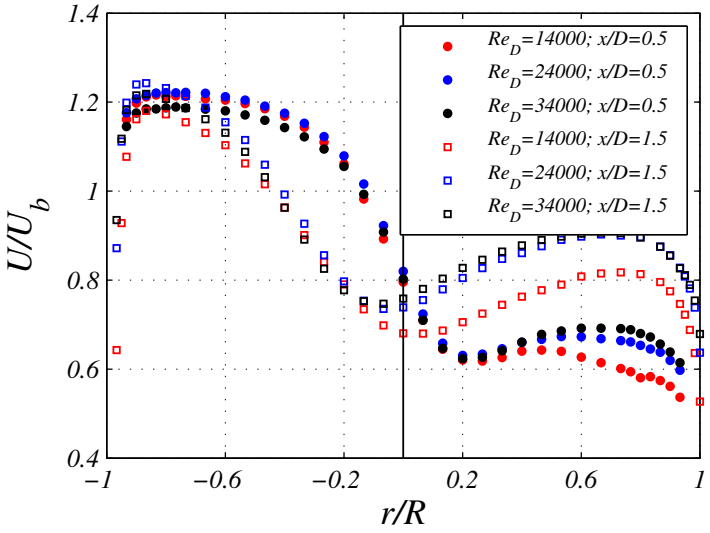

FIGURE 6.4. Comparison between mean velocity profiles at 0.5D and 1.5D downstream of bend exit for flow without swirl.

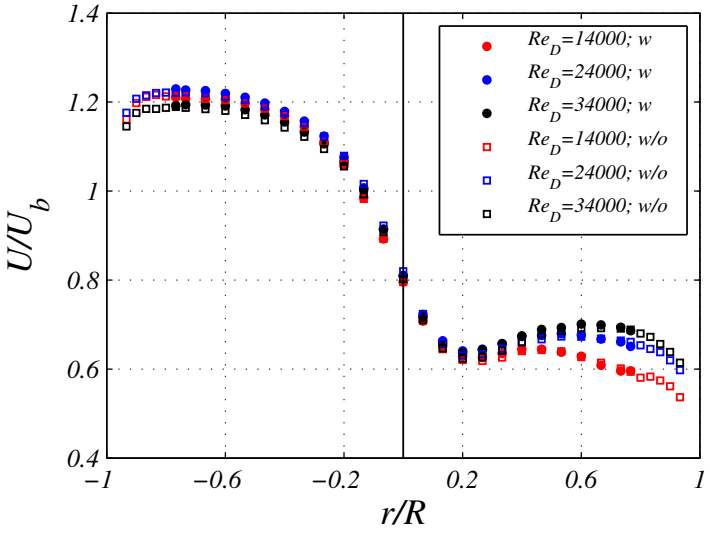

FIGURE 6.5. Mean velocity profiles at 0.5D downstream of bend exit; w and w/o represent with and without extra extension respectively.

Figures 6.6 and 6.7 illustrate mean velocity profiles of the turbulent swirling pipe flow into the 90° bend for different swirl numbers at 0.5D and 1.5D downstream of the bend exit in the tangential extension respectively while the Reynolds numbers was kept constant at 24000. It is shown that by increasing the swirl number, as the flow is becoming swirl dominant, the effect of pipe curvature is decreasing in the mean velocity profiles. The effect of swirl is more strong at 0.5D downstream of the bend exit compared to 1.5D of bend exit. The

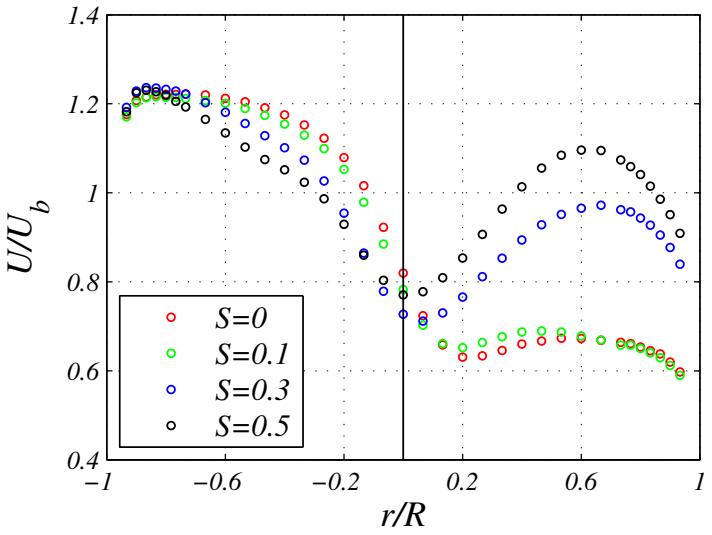

FIGURE 6.6. Swirl number effect on mean velocity profile of bend swirling pipe flow at 0.5D downstream of the bend exit for $Re = 24000$.

keen pipe curvature effects at 0.5D downstream the bend exit is smoothened both in outer and inner parts of the bend exit considerably for $S = 0.3$ and $S00.5$. The effect of swirl at 1.5D downstream the bend exit is mainly restricted to the flow close to inner part of the bend exit. The Reynolds number effect on the flow behavior after pipe curvature was also investigated while the swirl was kept constant at $S = 0.5$. The rsults are illustrated in figure 6.8.

The analyzed turbulence intensities, higher order moments, and PDF, autocorrelation and PSD contour plots are presented in the following sections.

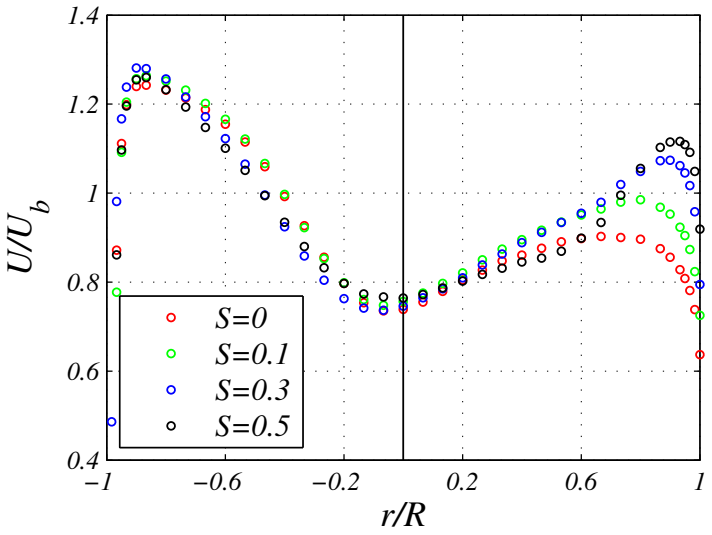

FIGURE 6.7. Swirl number effect on mean velocity profile of bend swirling pipe flow at 1.5D downstream of the bend exit for $Re = 24000$.

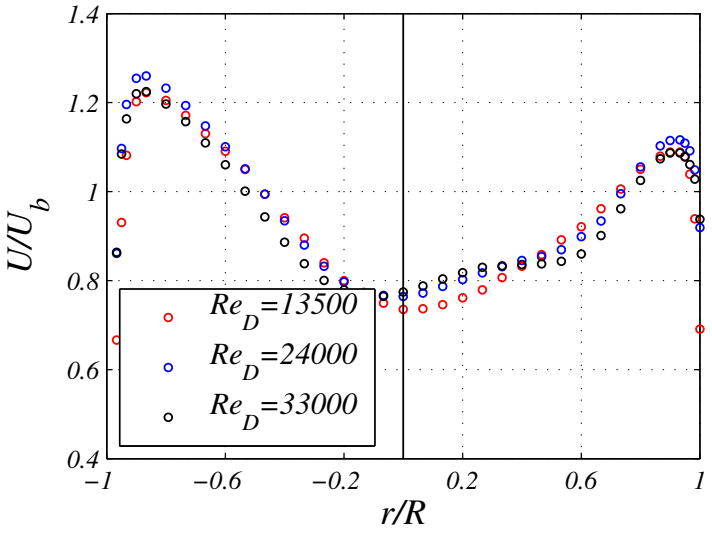

FIGURE 6.8. Reynolds number effect on mean velocity profile of bend swirling pipe flow at 1.5D downstream of the bend exit for $S = 0.5$.

6.2.2. *Turbulence intensity profiles*

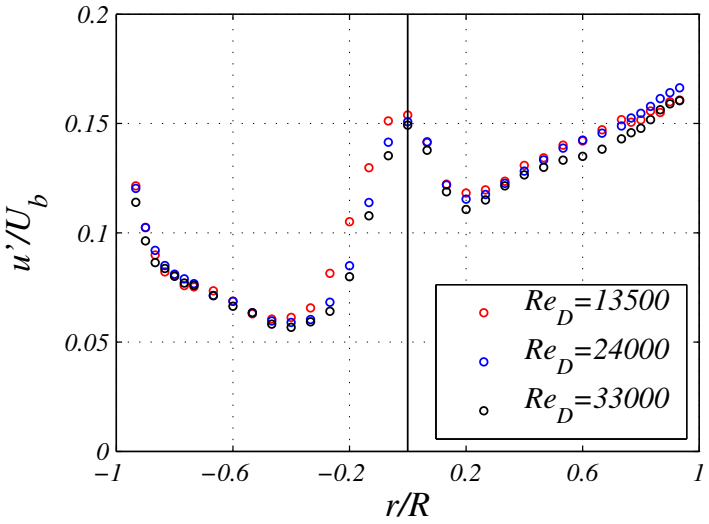

(a) Normalized by bulk velocity, U_b.

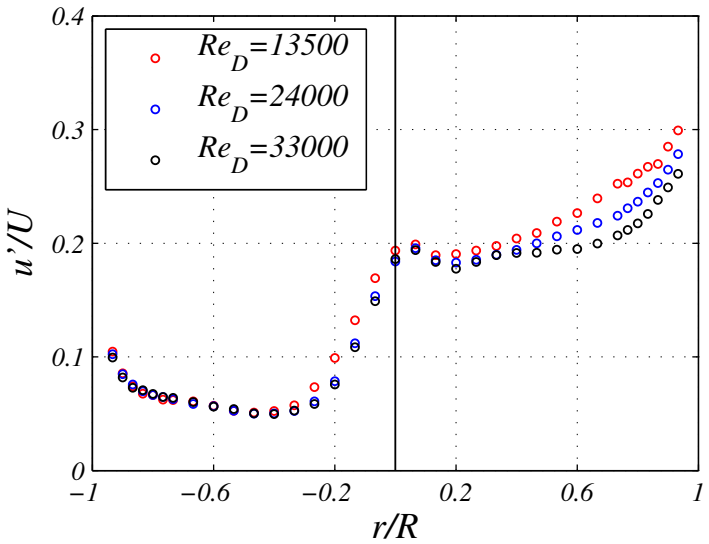

(b) Normalized by local mean velocity, U.

FIGURE 6.9. Reynolds number effect on the turbulence intensity at $x'/D = 0.5$ for the non-swirling case.

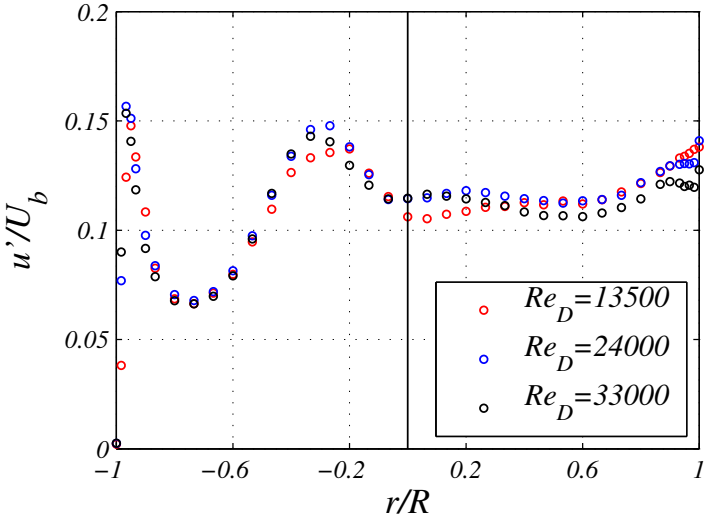

(a) Normalized by bulk velocity, U_b.

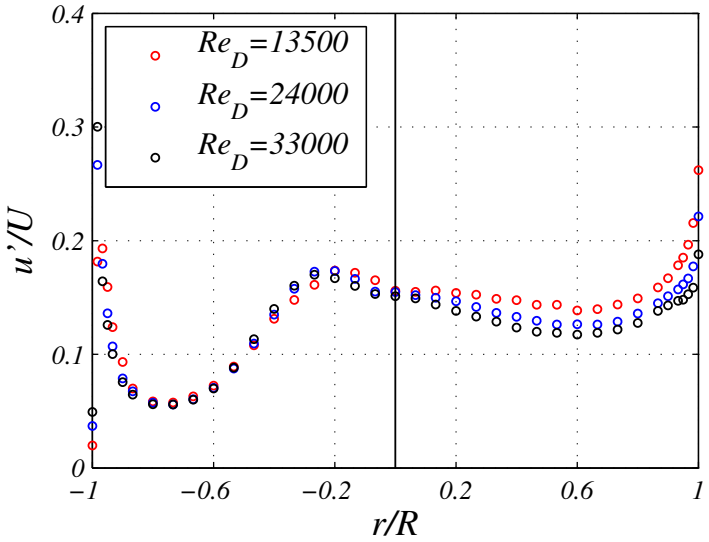

(b) Normalized by local mean velocity, U.

FIGURE 6.10. Reynolds number effect on the turbulence intensity at $x'/D = 1.5$ for the non-swirling case.

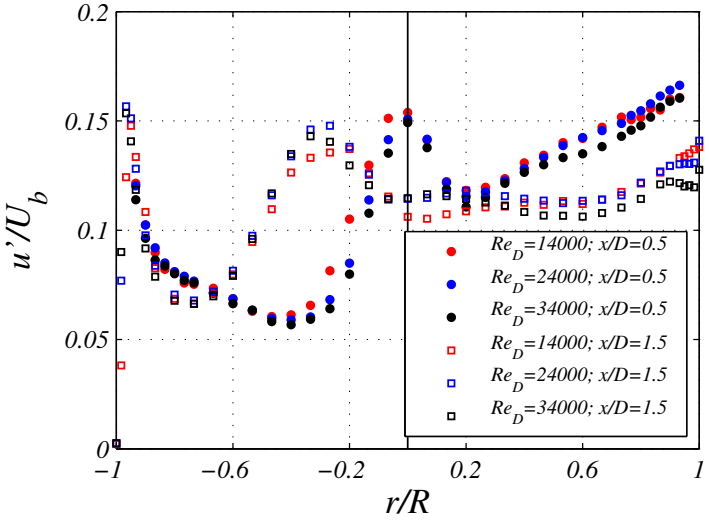

(a) Normalized by bulk velocity, U_b.

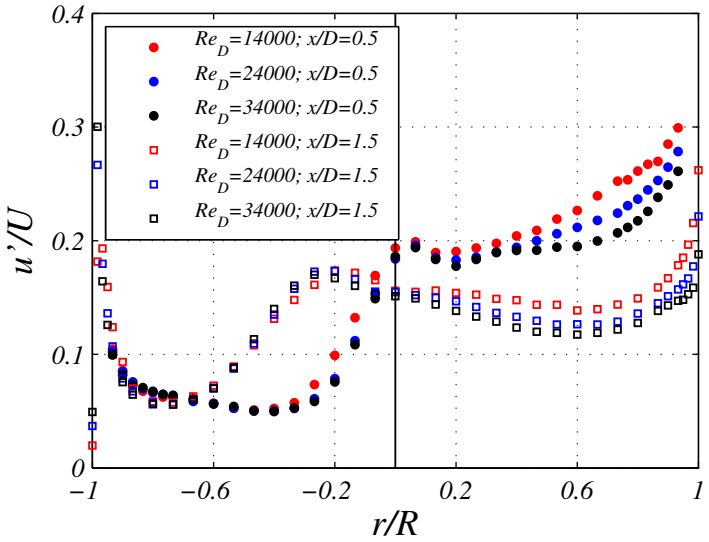

(b) Normalized by local mean velocity, U.

FIGURE 6.11. Comparison between the profiles of turbulence intensity at $x'/D = 0.5$ & 1.5 for the non-swirling case.

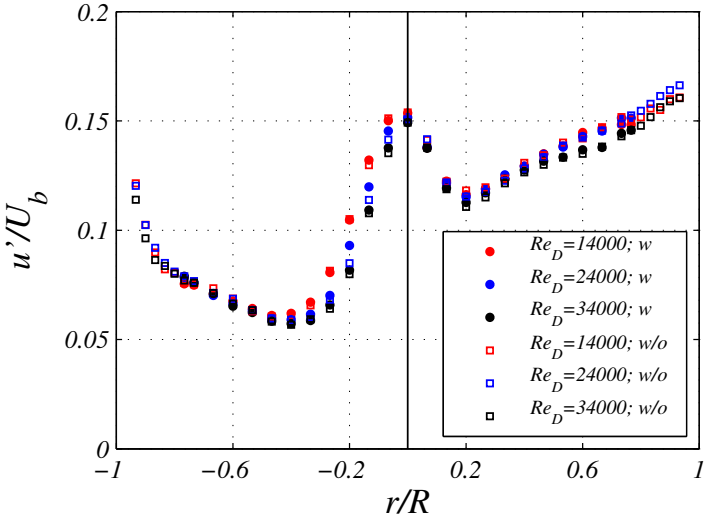

(a) Normalized by bulk velocity, U_b.

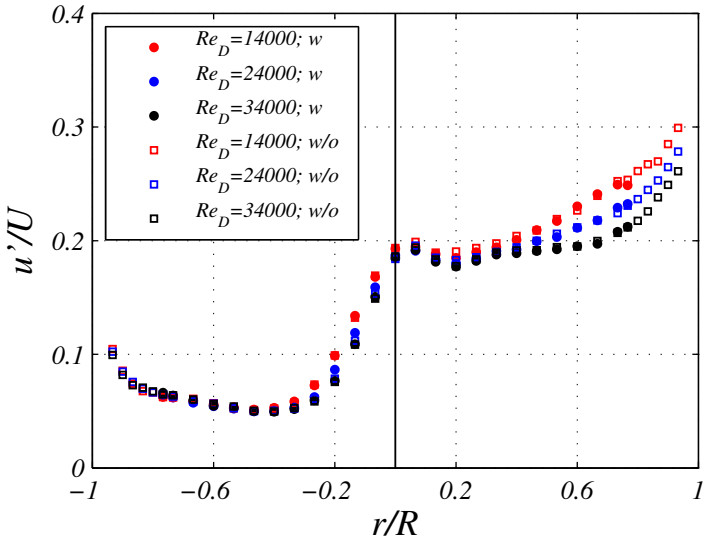

(b) Normalized by local mean velocity, U.

FIGURE 6.12. Profiles of turbulence intensity at $x'/D = 0.5$; w and w/o represent with and without extra extension respectively.

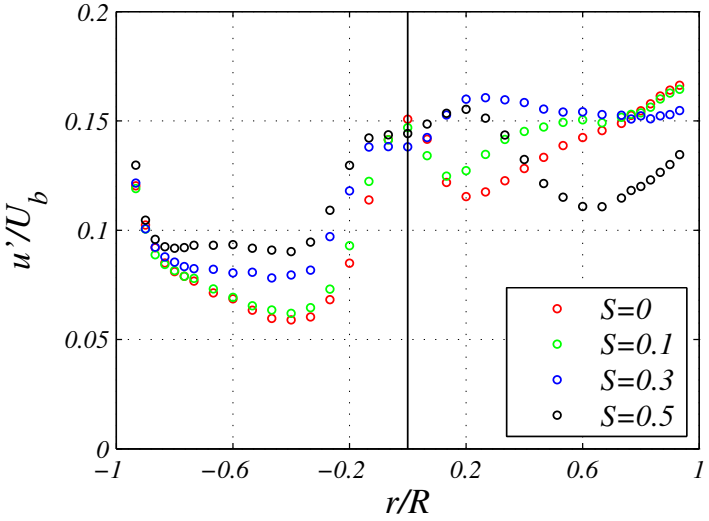

(a) Normalized by bulk velocity, U_b.

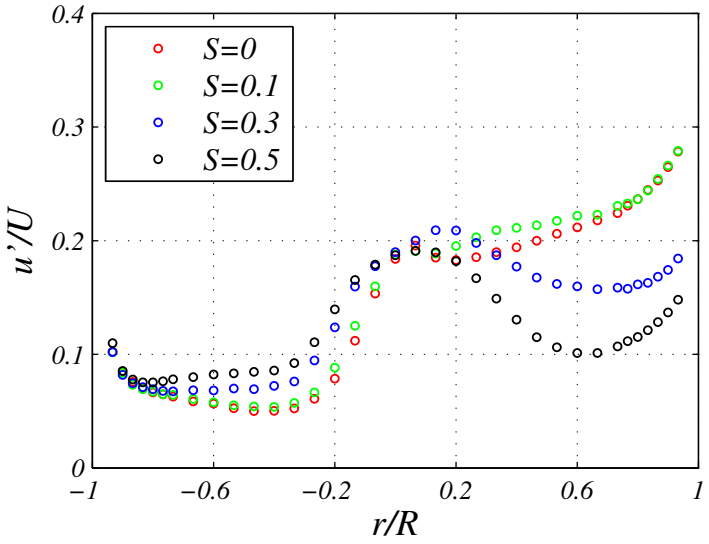

(b) Normalized by local mean velocity, U.

FIGURE 6.13. Swirl number effect on turbulence intensity at $x'/D = 0.5$ for $Re = 24000$.

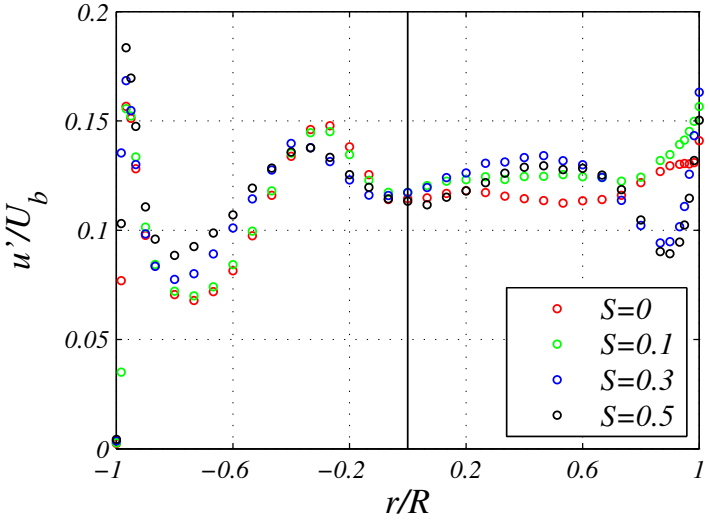

(a) Normalized by bulk velocity, U_b.

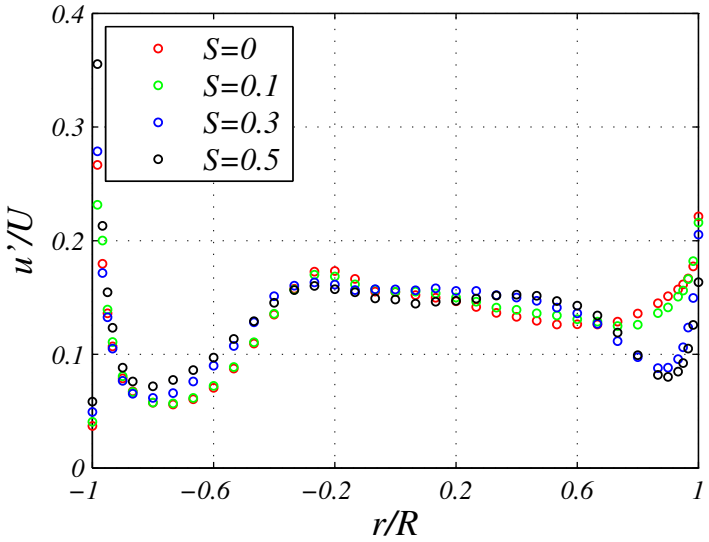

(b) Normalized by local mean velocity, U.

FIGURE 6.14. Swirl number effect on turbulence intensity at $x'/D = 1.5$ for $Re = 24000$.

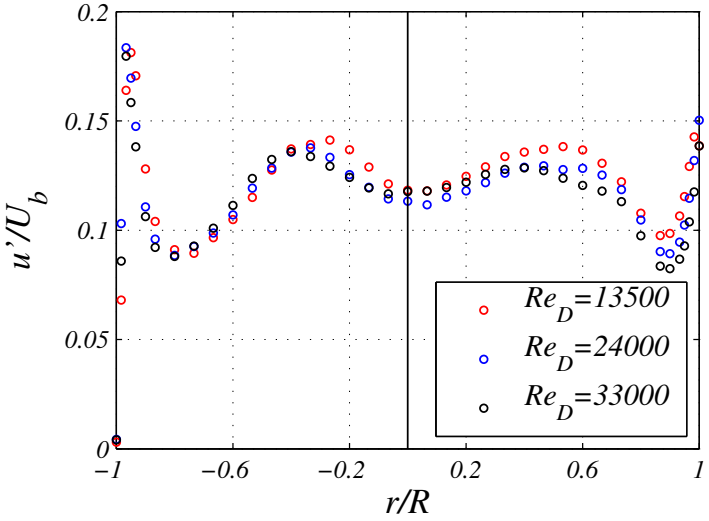

(a) Normalized by bulk velocity, U_b.

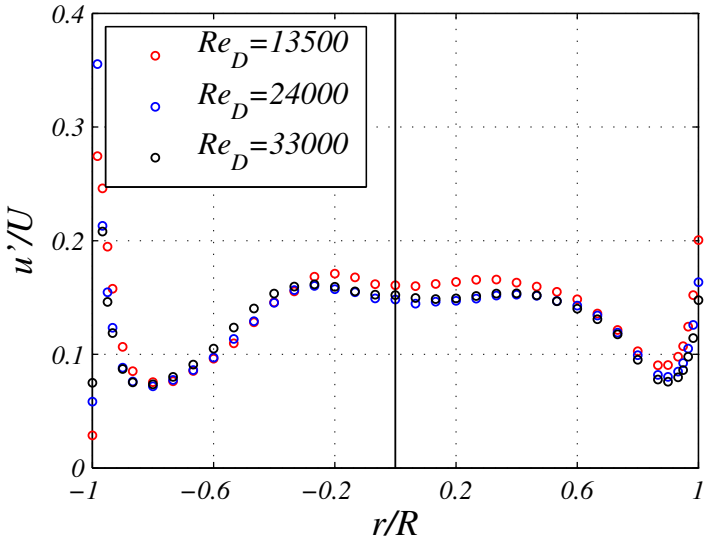

(b) Normalized by local mean velocity, U.

FIGURE 6.15. Reynolds number effect on turbulence intensity at $x'/D = 1.5$ for $S = 0.5$.

6.2.3. *Higher order moments*

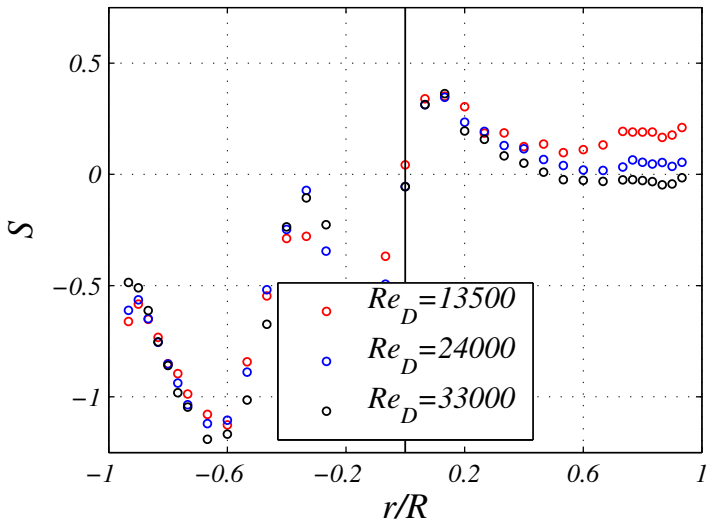

(a) at $x'/D = 0.5$.

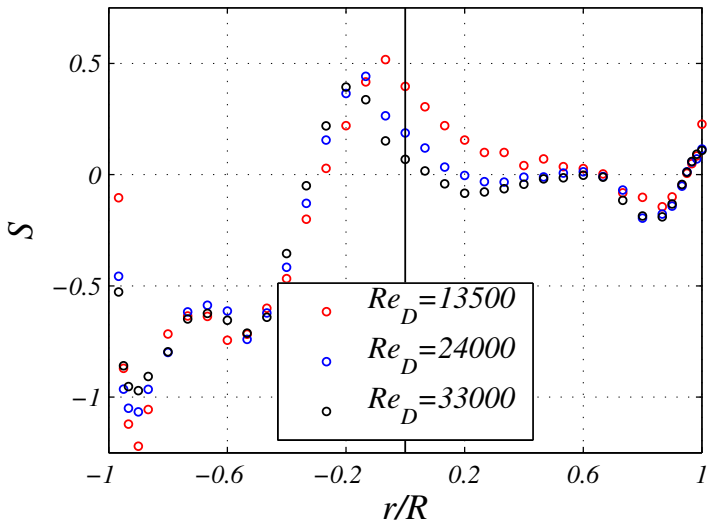

(b) at $x'/D = 1.5$.

FIGURE 6.16. Reynolds number effect on skewness distribution for non-swirling flow.

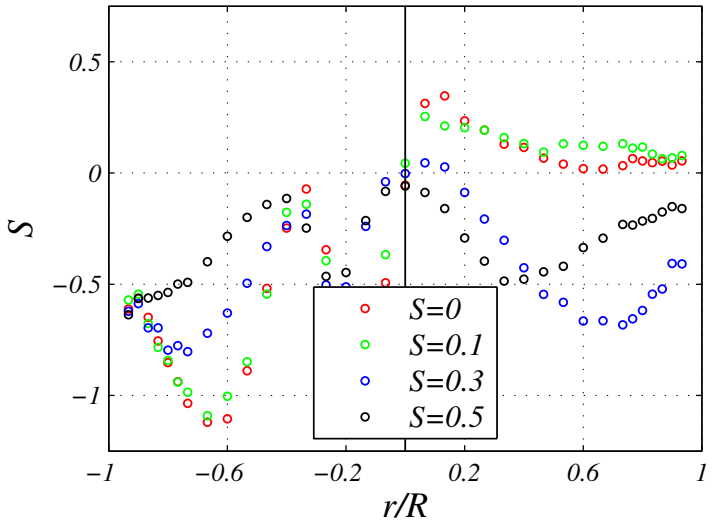

(a) at $x'/D = 0.5$.

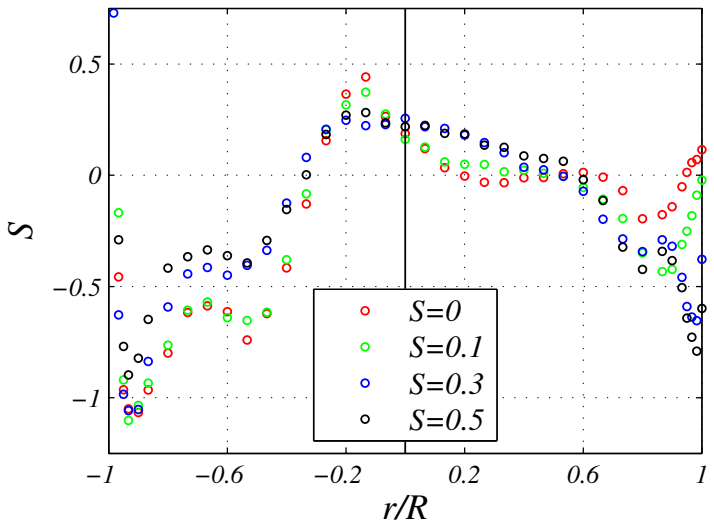

(b) at $x'/D = 1.5$.

FIGURE 6.17. Swirl number effect on skewness distribution for $Re = 24000$.

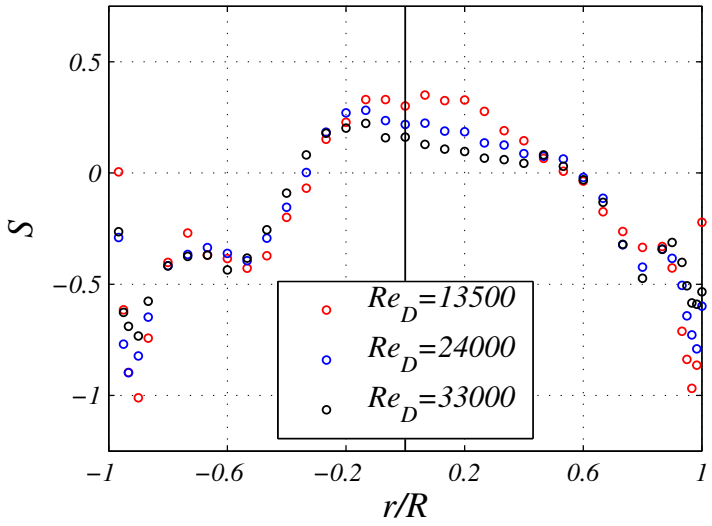

FIGURE 6.18. Reynolds number effect on skewness distribution at $x'/D = 1.5$ for $S = 0.5$.

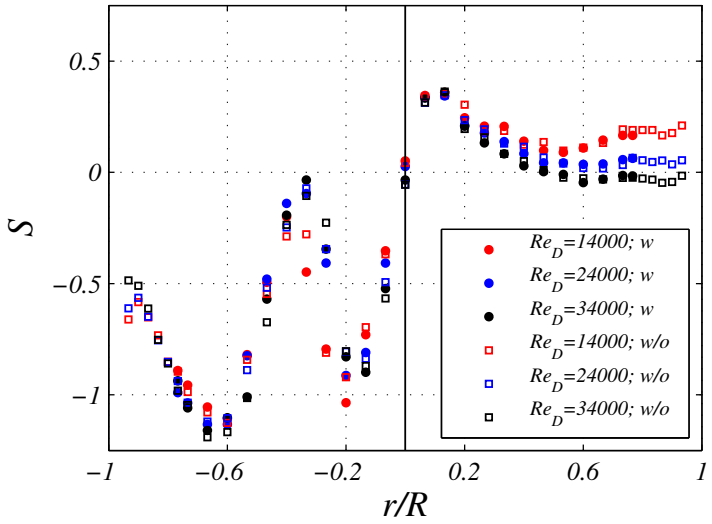

FIGURE 6.19. Skewness distribution at $x'/D = 0.5$; w and w/o represent with and without extra extension respectively.

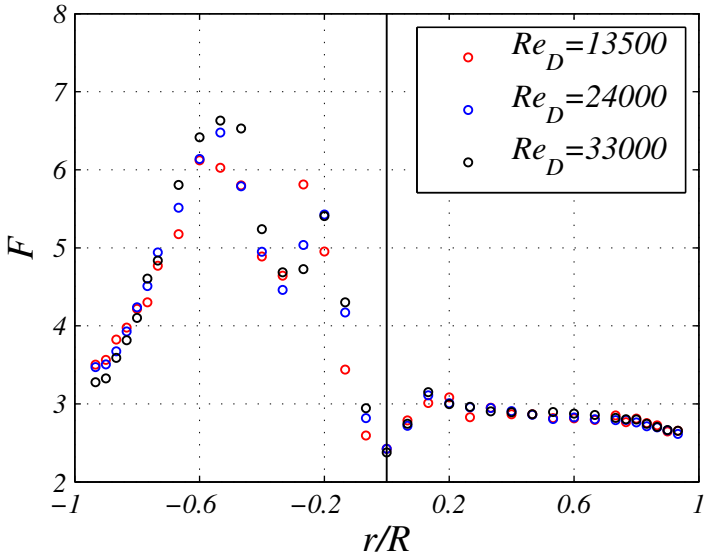

(a) at $x'/D = 0.5$.

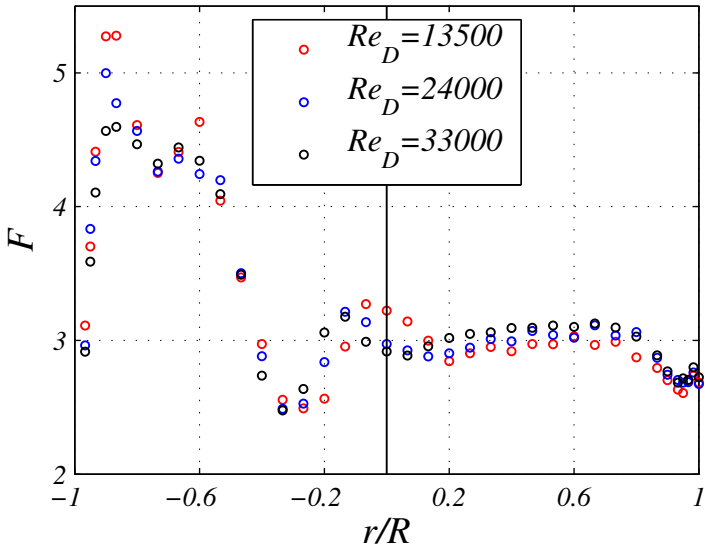

(b) at $x'/D = 1.5$.

FIGURE 6.20. Reynolds number effect on flatness distribution for non-swirling flow.

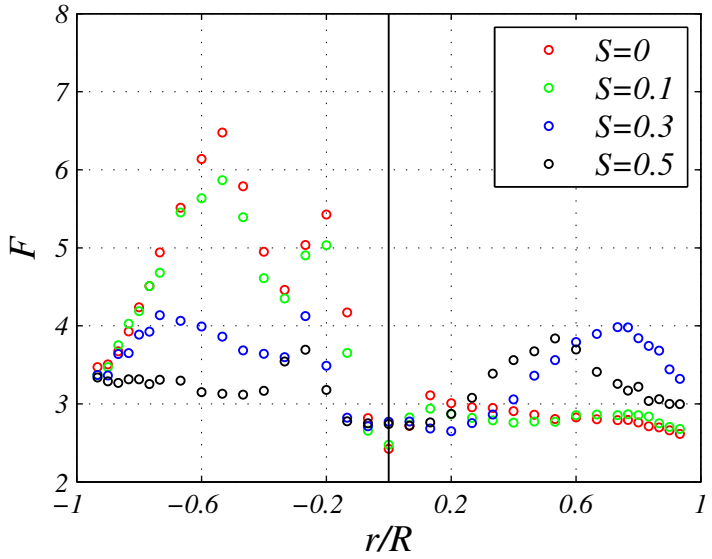

(a) at $x'/D = 0.5$.

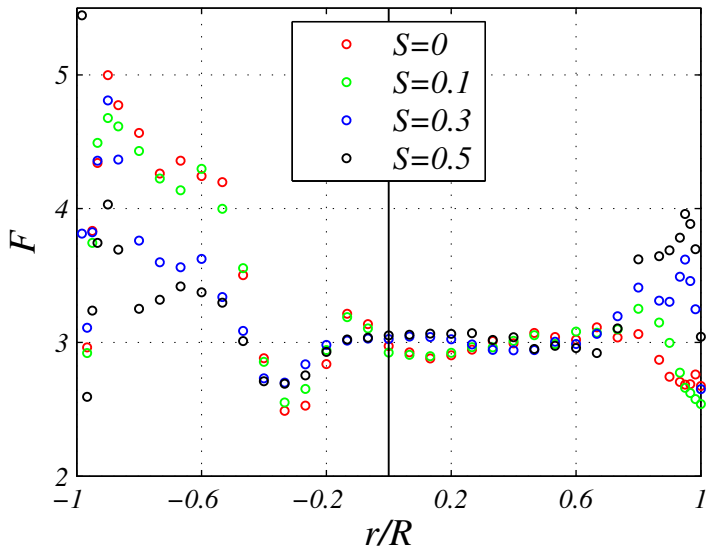

(b) at $x'/D = 1.5$.

FIGURE 6.21. Swirl number effect on flatness distribution for $Re = 24000$.

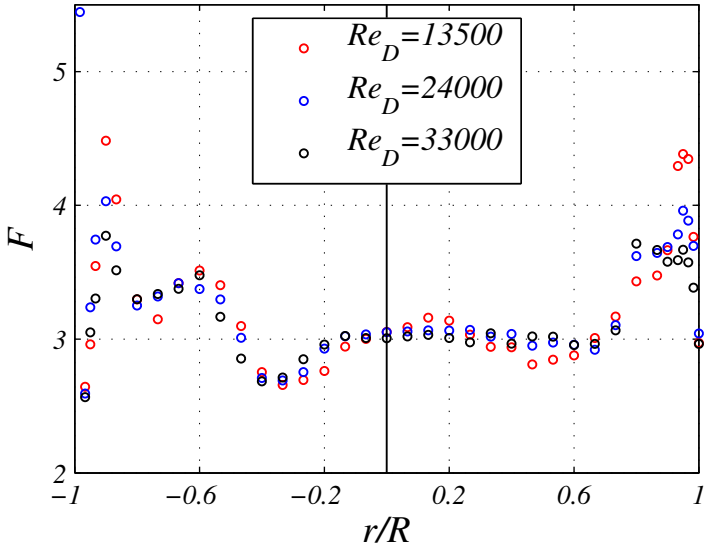

FIGURE 6.22. Reynolds number effect on flatness distribution at $x'/D = 1.5$ for $S = 0.5$.

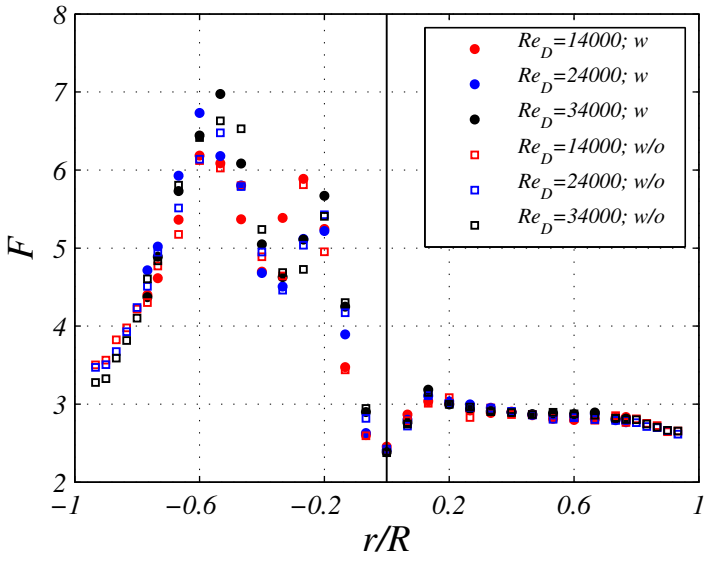

FIGURE 6.23. Flatness distribution at $x'/D = 0.5$; w and w/o represent with and without extra extension respectively.

6.2.4. *Probability density function (PDF) maps*

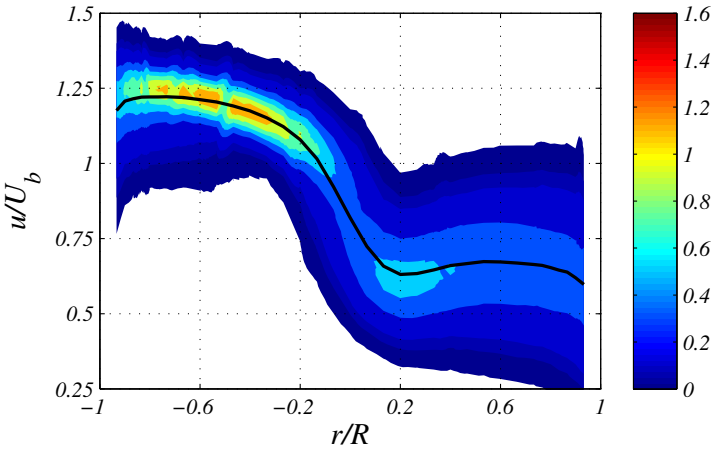

FIGURE 6.24. Contours of PDF distributions along cross-stream horizontal line at 0.5D downstream of the bend exit for $Re = 24000$ and $S = 0$.

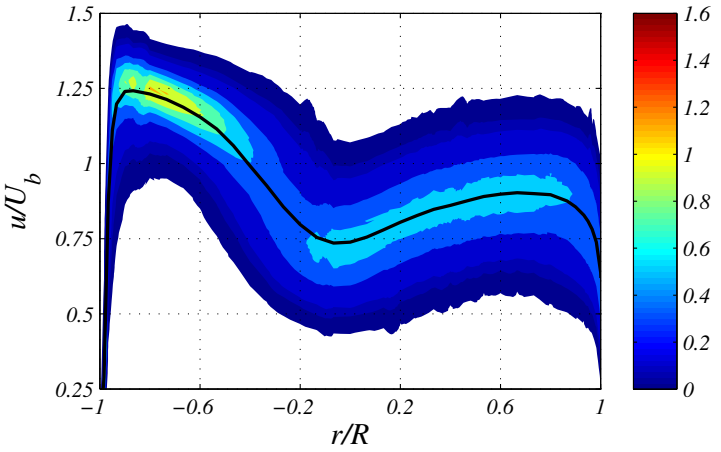

FIGURE 6.25. Contours of PDF distributions along cross-stream horizontal line at 1.5D downstream of the bend exit for $Re = 24000$ and $S = 0$.

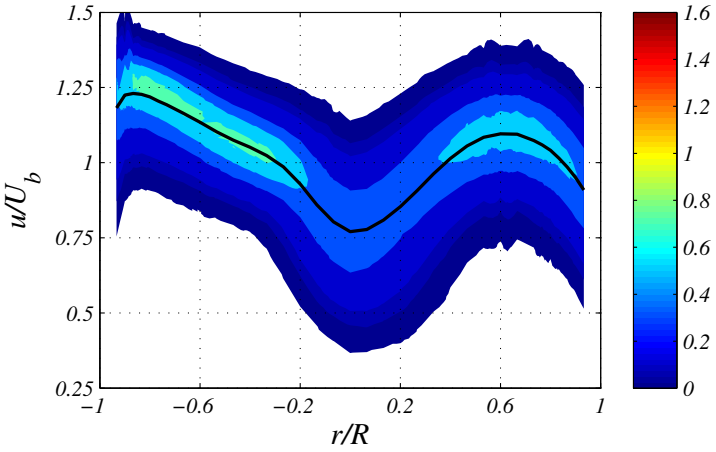

FIGURE 6.26. Contours of PDF distributions along cross-stream horizontal line at 0.5D downstream of the bend exit for $Re = 24000$ and $S = 0.5$.

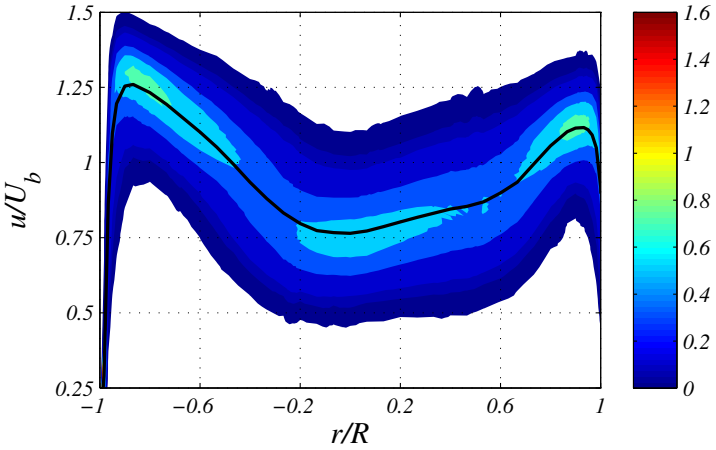

FIGURE 6.27. Contours of PDF distributions along cross-stream horizontal line at 1.5D downstream of the bend exit for $Re = 24000$ and $S = 0.5$.

6.2.5. *Autocorrelation function maps*

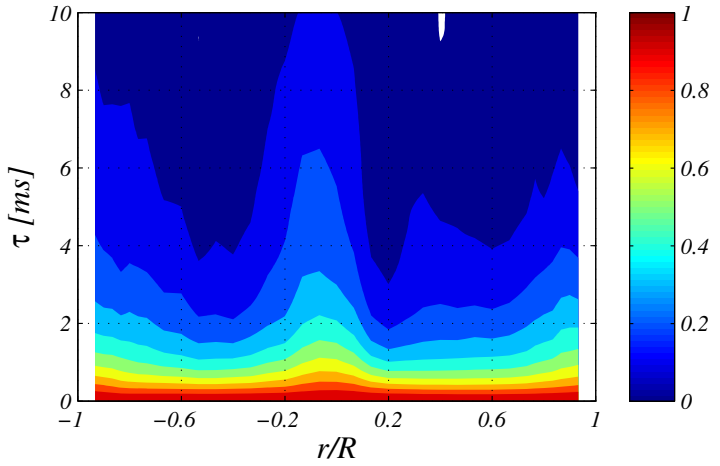

FIGURE 6.28. Contours of autocorrelation distributions along cross-stream horizontal line at 0.5D downstream of the bend exit for $Re = 24000$ and $S = 0$.

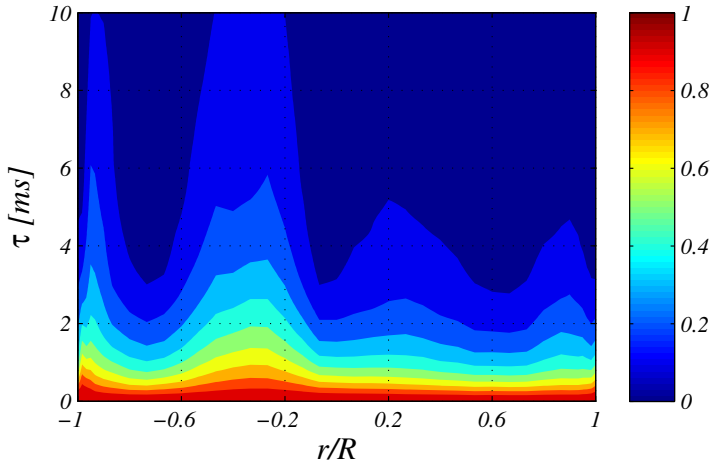

FIGURE 6.29. Contours of autocorrelation distributions along cross-stream horizontal line at 1.5D downstream of the bend exit for $Re = 24000$ and $S = 0$.

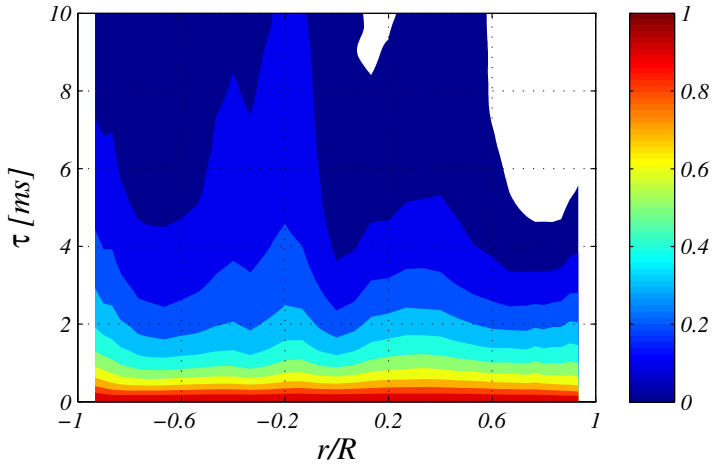

FIGURE 6.30. Contours of autocorrelation distributions along cross-stream horizontal line at 0.5D downstream of the bend exit for $Re = 24000$ and $S = 0.5$.

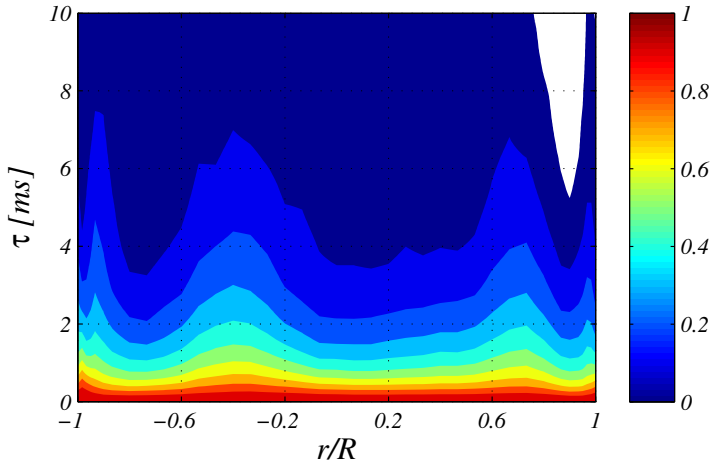

FIGURE 6.31. Contours of autocorrelation distributions along cross-stream horizontal line at 1.5D downstream of the bend exit for $Re = 24000$ and $S = 0.5$.

6.2.6. *Power-spectral density (PSD) function maps*

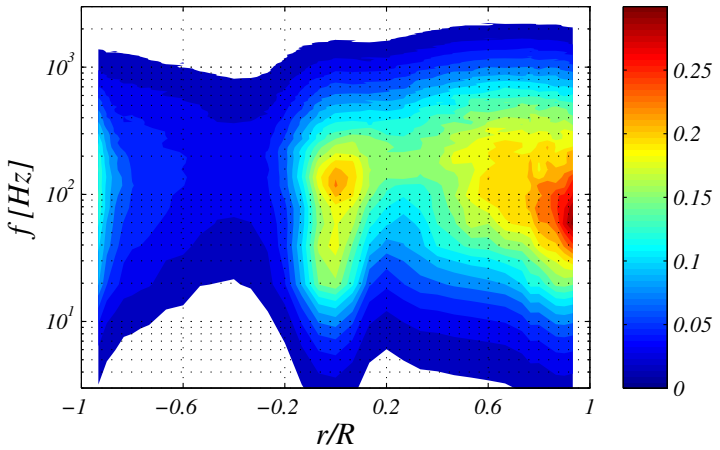

FIGURE 6.32. Contours of power-spectral density distributions along cross-stream horizontal line at 0.5D downstream of the bend exit for $Re = 24000$ and $S = 0$.

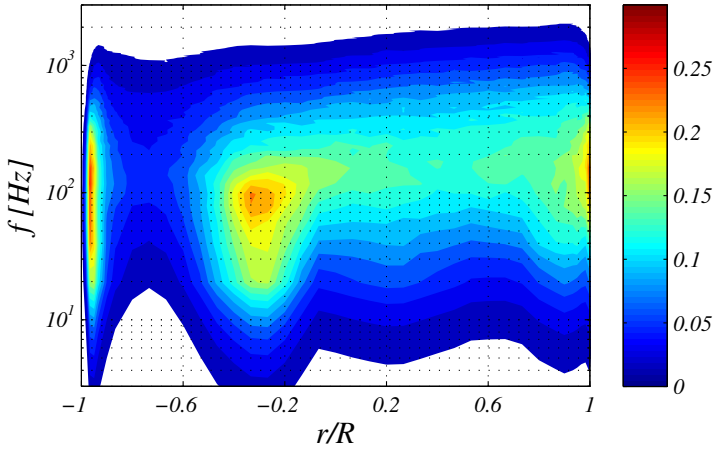

FIGURE 6.33. Contours of power-spectral density distributions along cross-stream horizontal line at 1.5D downstream of the bend exit for $Re = 24000$ and $S = 0$.

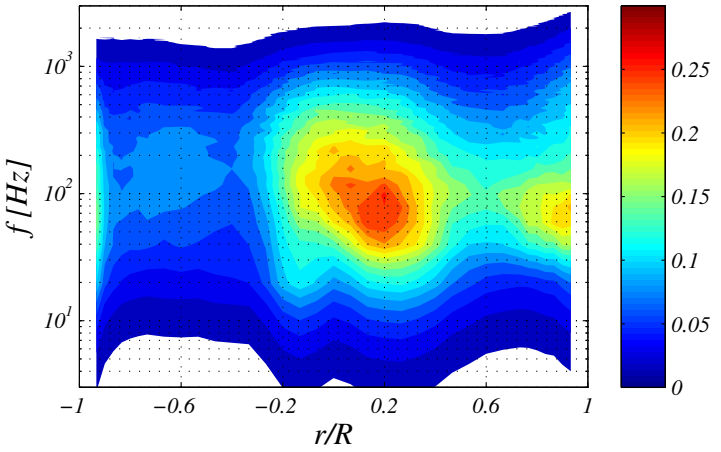

FIGURE 6.34. Contours of power-spectral density distributions along cross-stream horizontal line at 0.5D downstream of the bend exit for $Re = 24000$ and $S = 0.5$.

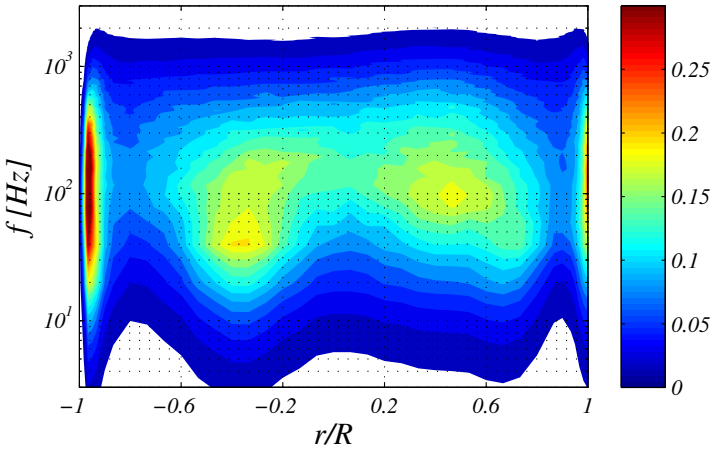

FIGURE 6.35. Contours of power-spectral density distributions along cross-stream horizontal line at 1.5D downstream of the bend exit for $Re = 24000$ and $S = 0.5$.

Acknowledgements

This work is a part of a larger project within the *CICERO/CCGEx* (Competence Centre for Gas Exchange).

First of all I want to thank my supervisor Prof. Henrik Alfredsson for trusting me and giving me the opportunity to work at the Fluid Physics Laboratory of KTH Mechanics, and also for his key guidance and comments throughout my work.

I would like to express my deep gratitude to my co-advisor Dr. Ramis Örlü for all his technical and non-technical helps, and also for guiding me to become an experimental fluid dynamicist from scratch.

I want to thank Sissy for spending extensive hours at the hot-wire corner helping me with all the hot-wire related problems, and Antonio for helping me with fixing the problems regarding the *LabView*. Also thanks to Bengt for helping me dealing with the problems occurring in the experimental setup during my measurements.

Special thanks to Dr. Nils Tillmark, Dr. Jens Fransson, Dr. Fredril Lundell, and all of the people in the lab specially Gabrielle, Malte, Outi, Ylva, Shahab, Niklas, Johan, Karl, Mathias, Shintaro, Markus, Fredrik La, Alexander, Emma, and my office mate Gustav for making it a nice and warm place to work in even during the cold winter. Kim and Göran, our toolmakers, are acknowledged for helping me whenever it was needed.

To my former classmates in the M.Sc. program at KTH, Iman, Soolmaz, Mohamad, Reza, and Amin: Thank you for your help and all the good thing that you gave me during our time at KTH.

Last but definitely not least I want to thank my parents, Shohreh and Sattar, and my sister, Sogol, for supporting me, in any sense, throughout all my life, and assuring me that they will be there for me anytime. I wouldn't have reached anywhere without you.

APPENDIX A

Turbulent pipe flow results in inner scaling

A.1. Results

A.1.1. *Mean velocity profiles*

Figure A.1 shows the mean velocity profile in inner-scaling for all 17 measurements including data points that are affected by additional heat losses to the wall. Note that despite the different wire length and diameter, the majority of measured data points within the viscous sublayer seem to collapse on a general trend.

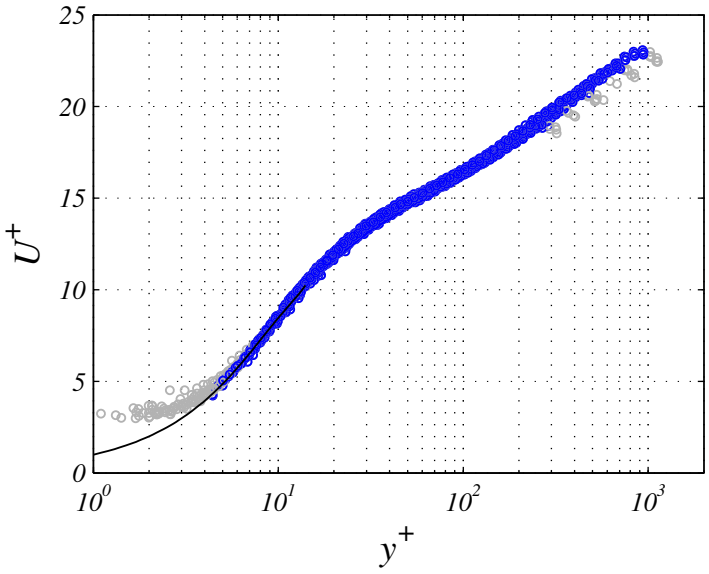

FIGURE A.1. Mean velocity profiles in inner scaling for all 17 measurements. Gray shaded data points denote those measurements that are affected by additional heat losses to the wall as well those that correspond to the other half of the pipe cross-section. Solid lines depicts the extended linear profile to fifth order.

Although figure A.1 displays Reynolds number effects in the core region, figure A.2, in addition, shows the Reynolds number effect for R^+ equal to 283, 433, 664 and 901 at fixed inner-scalled wire length of $L^+ \approx 15$. It can be observed from this figure that the overlap region is increasing with the Reynolds number. Also the spatial resolution effects on the mean velocity profiles in

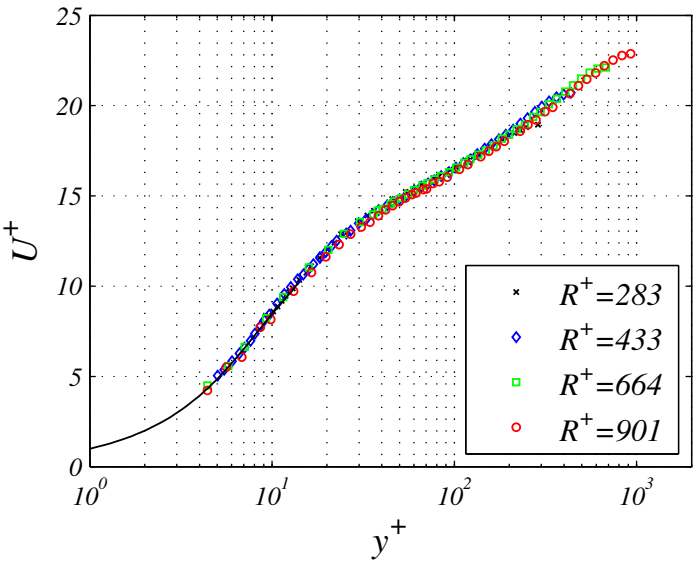

FIGURE A.2. Mean velocity profiles in inner scaling for different R^+ at fixed inner-scaled wire length, i.e. $L^+ \approx 15$. Solid lines depicts the extended linear profile to fifth order.

inner scaling for $R^+ \approx 420$ and $R^+ \approx 900$ are depicted in figures A.3 and A.4 respectively. For each R^+, the results of measuring with four different inner-scaled wire lengths, L^+, are illustrated, and it can be conjectured that spatial resolution, L^+, has no effects on mean velocity profiles within the accuracy of the measurements in the present study. Also these figures illustrate the repeatability of the performed measurements with four different hot-wire probes and lengths.

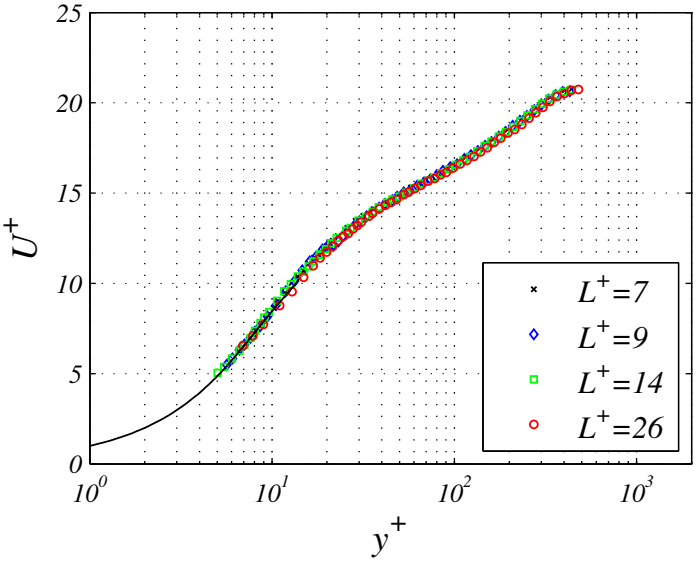

FIGURE A.3. Mean velocity profiles in inner scaling for different L^+ at $R^+ \approx 420$.

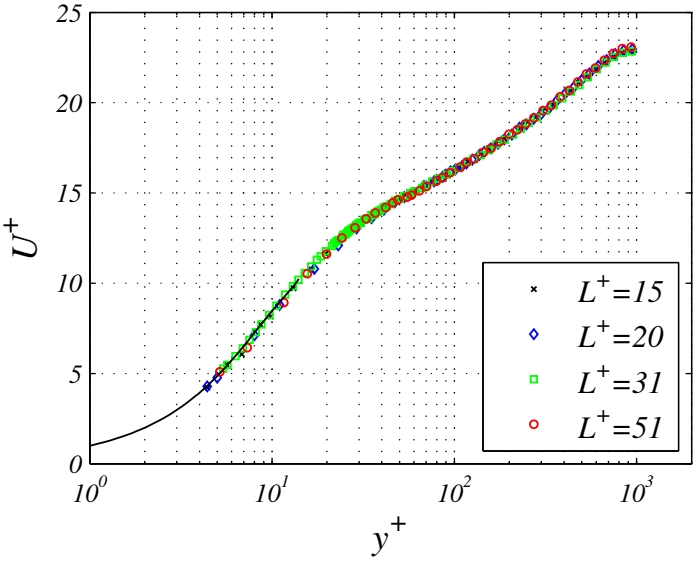

FIGURE A.4. Mean velocity profiles in inner scaling for different L^+ at $R^+ \approx 900$.

A.1.2. *Turbulence intensity profiles*

Figure A.5 illustrates the turbulence intensity profiles in inner scaling for all the measurements performed in the fully developed turbulent pipe flow. The affected measured data points due to additional heat losses that are excluded for fitting the mean velocity profiles to composite mean velocity profiles from DNS were investigated through depicted turbulence intensity profiles in figure A.5 and are denoted by the grey shaded data points in the inner region.

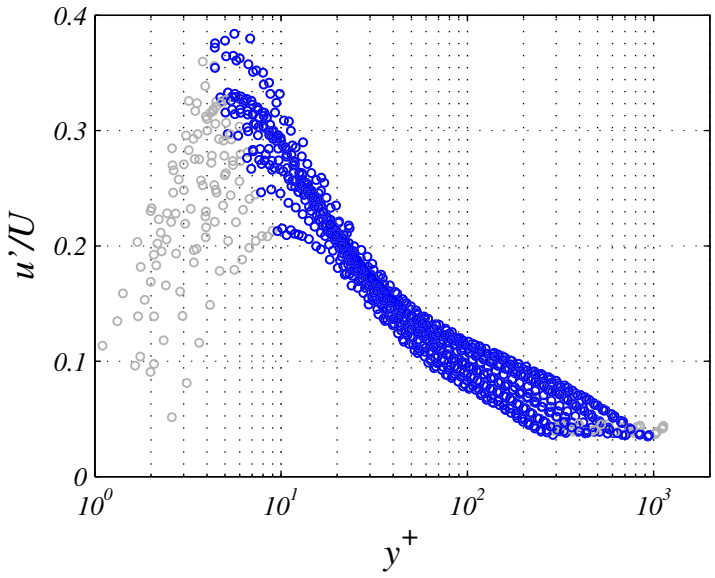

FIGURE A.5. Profiles of the turbulence intensity in inner scaling for all 17 measurements. Gray shaded data points denote those measurements that are affected by additional heat losses to the wall as well those that correspond to the other half of the pipe cross-section.

The turbulence intensity as a function of R^+ is depicted in figure A.6 for $L^+ \approx 15$. Since the mean velocity of the flow is expected to become zero by moving toward the wall, the value of the turbulence intensity is expected to increase by reaching the wall. But as can be observed from figure A.6 and A.5, depending on R^+, turbulence intensity increases up to a value and thereafter decreases. This imperfection is due to measurement limits according to wall interference factors and initiation of heat conduction between the hot-wire and the pipe wall. The L^+ effects on turbulence intensity profiles for four inner-scaled wire lengths are depicted in figures A.7 and A.8. It can be observed

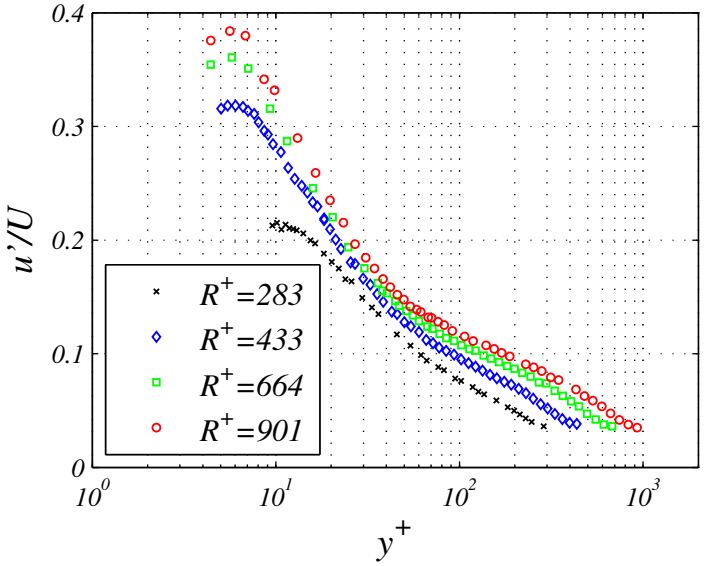

FIGURE A.6. Turbulence intensity profiles for different Re^+ at fixed inner-scaled wire length, i.e. $L^+ \approx 15$.

that in approximately constant R^+, the measured peak of turbulence intensity is affected by L^+, and increases for lower L^+. It can be inferred from figures A.6, A.7 and A.8 that the peak in the measured turbulence intensity is dependent on both R^+ and L^+ in the way that it is increasing by an increase in R^+ and a decrease in L^+. The Reynolds number dependent growth in the measured turbulence intensity peak is in agreement with Örlü & Schlatter (2011), and in contrary to Hultmark *et al.* (2010) where a decay in the turbulence intensity peak in the inner region is observed by an increase in the Reynolds number.

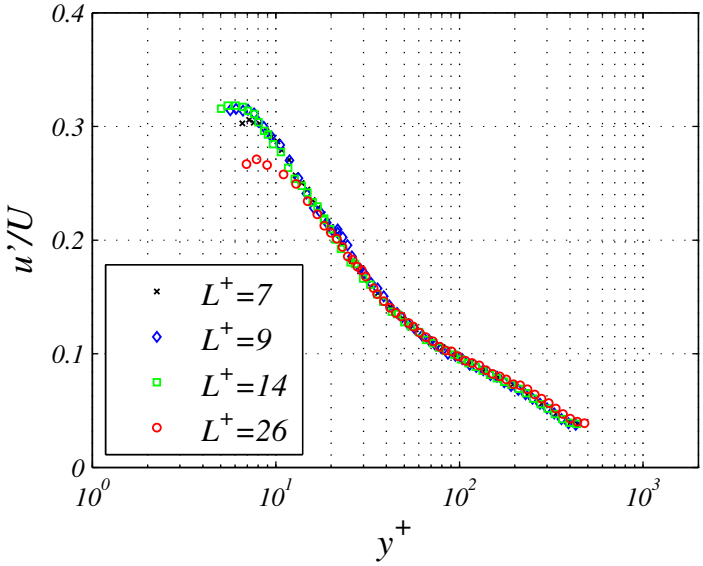

FIGURE A.7. Turbulence intensity profiles for different L^+ at $R^+ \approx 420$.

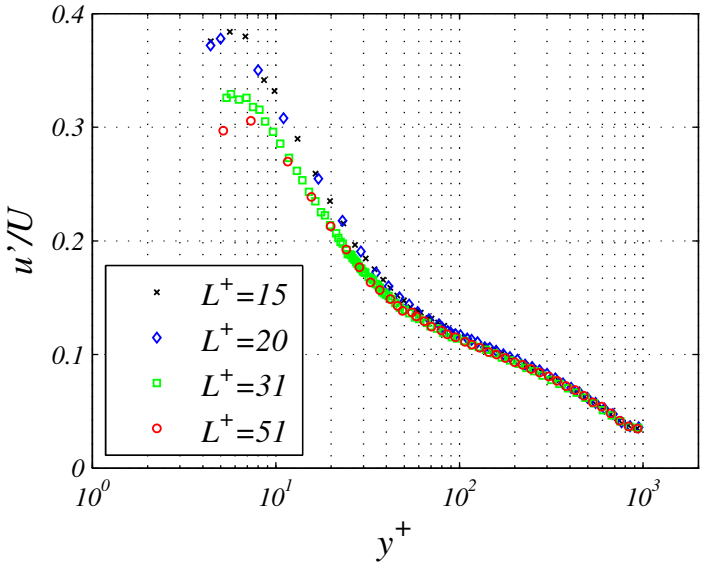

FIGURE A.8. Turbulence intensity profiles for different L^+ at $R^+ \approx 900$.

Figure A.9 illustrates the profiles of the root mean square of the velocity fluctuations, u', normalized by the friction velocity, u_τ, in inner scaling for all 17 measurements.

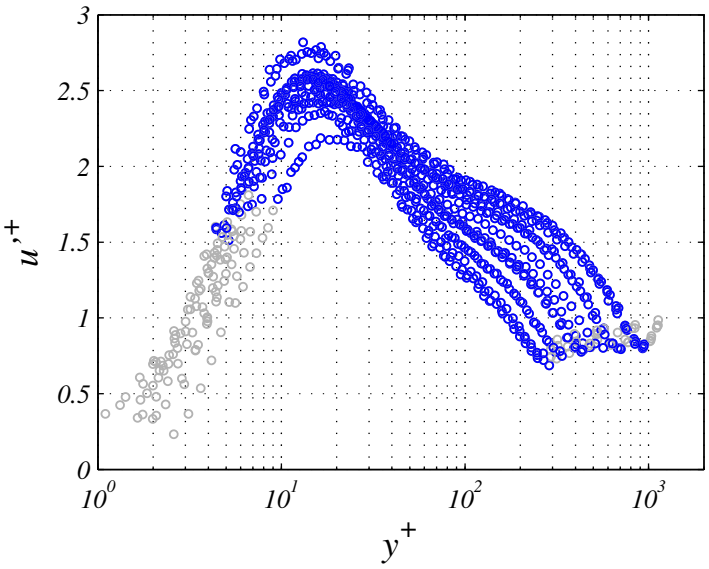

FIGURE A.9. Profiles of the root mean square of the velocity fluctuations, u', normalized by the friction velocity, u_τ, in inner scaling for all 17 measurements. Gray shaded data points denote those measurements that are affected by additional heat losses to the wall as well those that correspond to the other half of the pipe cross-section.

The Reynolds number effects on the profiles of the root mean square of the velocity fluctuations for $L^+ \approx 15$ is depicted in figure A.10. The maximum value of the velocity fluctuations increases with an increase in the Reynolds number as depicted in figure A.10. This result is similar to the fully developed turbulent pipe flow DNS results, and also both DNS and experimental results of the channel flows and turbulent boundary layer (TBL) flows. In contrary, the results reported by Hultmark *et al.* (2010) demonstrates a constant value for maximum of the velocity fluctuations in the inner region irrespective of the Reynolds number at fixed inner-scaled wire length of $L^+ \approx 20$. Spatial resolution effects on the profiles of the root mean square of the velocity fluctuations in inner scaling are also illustrated in figures A.11 and A.12 for $Re^+ \approx 420$ and $Re^+ \approx 900$ respectively. It can be observed that similar to turbulence intensity profiles, inner-scaled wire length, L^+, is affecting u'^+, and the u'^+_{max}

is increasing with a reduction in L^+, but it seems to be a threshold for the spatial resolution effects on the measured data. As depicted in figure A.11, for L^+ lower than 10 no apparent differences are observed.

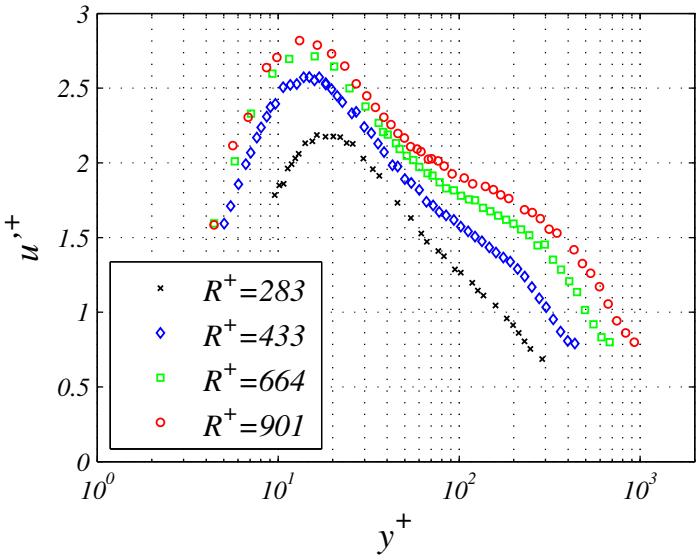

FIGURE A.10. Profiles of the root mean square of the velocity fluctuations, u', normalized by the friction velocity, u_τ, in inner scaling for different R^+ at fixed inner-scaled wire length, i.e. $L^+ \approx 15$.

In order to illustrate the different reported dependancy of the maximum root mean square of the velocity fluctuations in the inner region with respect to the Reynolds number changes, the maximum variance of the velocity fluctuations normalized by friction velocity, u'^{+2}_{max}, obtained from the earlier DNS and experimental studies as well the results from the present study are depicted in figure A.13 with respect to different Reynolds numbers. The growth in the maximum variance with an increase in the Reynolds number is clearly shown for the DNS data and the results from the present study while the results reported by Hultmark *et al.* (2010) are bounded within the area between the depicted dashed lines and show an independent behavior with respect to the Reynolds number changes.

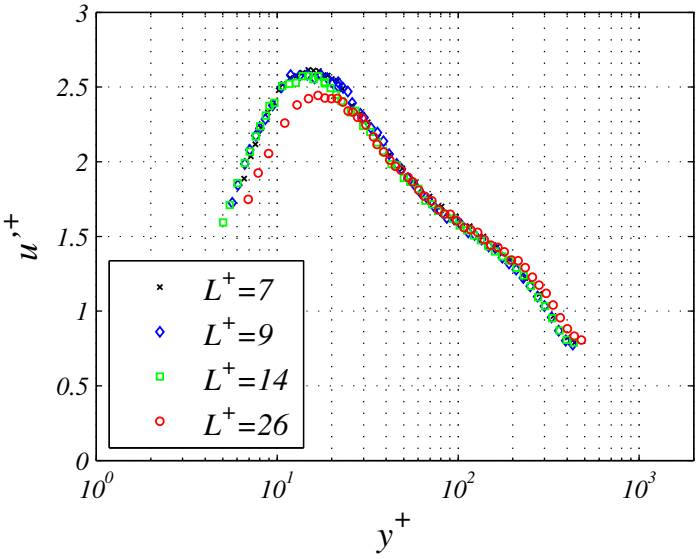

FIGURE A.11. Profiles of the r.m.s of the velocity fluctuations, u', normalized by the friction velocity, u_τ, at $R^+ \approx 420$.

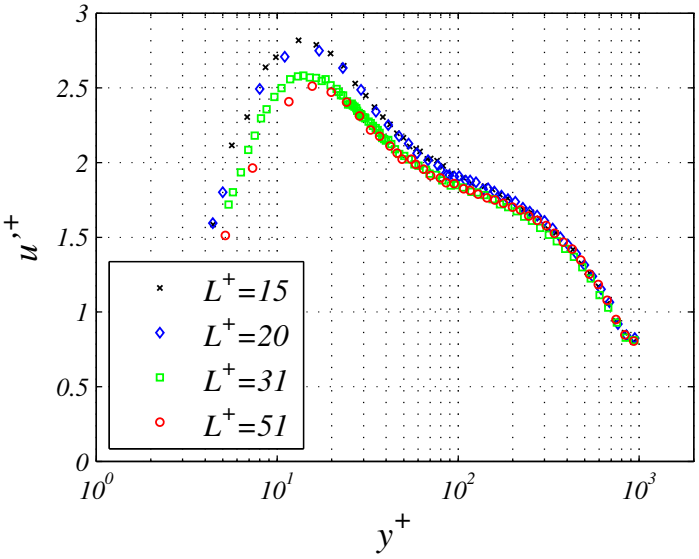

FIGURE A.12. Profiles of the r.m.s of the velocity fluctuations, u', normalized by the friction velocity, u_τ, at $R^+ \approx 900$.

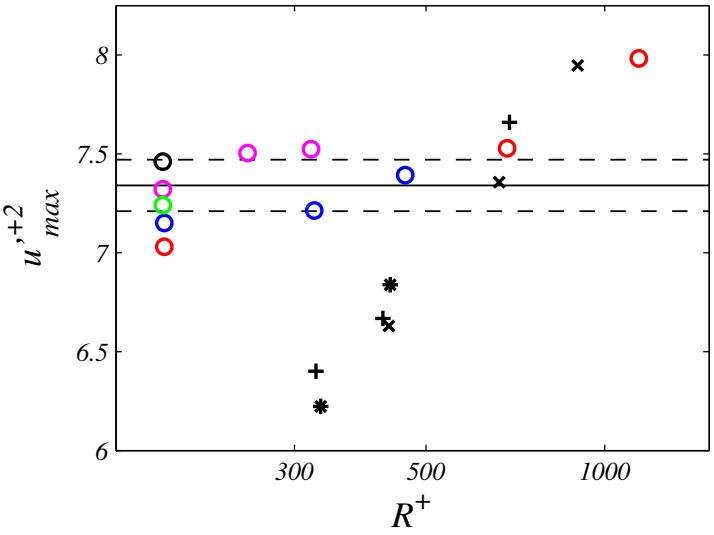

FIGURE A.13. The maximum variance, u'^2, normalized by the friction velocity with respect to different Re_τ for different turbulent pipe flow results from DNS and experiments. The solid line and the dashed lines illustrate the criteria obtained by experiments in Princeton University by Hultmark *et al.* (2010), and the open circles are from DNS data (black: Eggels *et al.* (1994), green: Fukagata (2001), Wagner *et al.* (2001), blue: Veenman (2004), red: Wu & Moin (2008)). The $'*'$, $'+'$ and $'\times'$ symbols are obtained from the present study with different fixed inner-scaled wire length.

A.1.3. *Higher order moments*

The profiles of the skewness and the flatness values are illustrated in the figures of this section in inner scaling. Figure A.14 illustrates the Reynolds number effect on the profiles of the skewness values measured at fixed inner-scaled wire length of $L^+ \approx 15$. Also, the spatial resolution effects on the measured skewness values are depicted in figures A.15 and A.16 for R^+ equal to approximately 420 and 900 respectively.

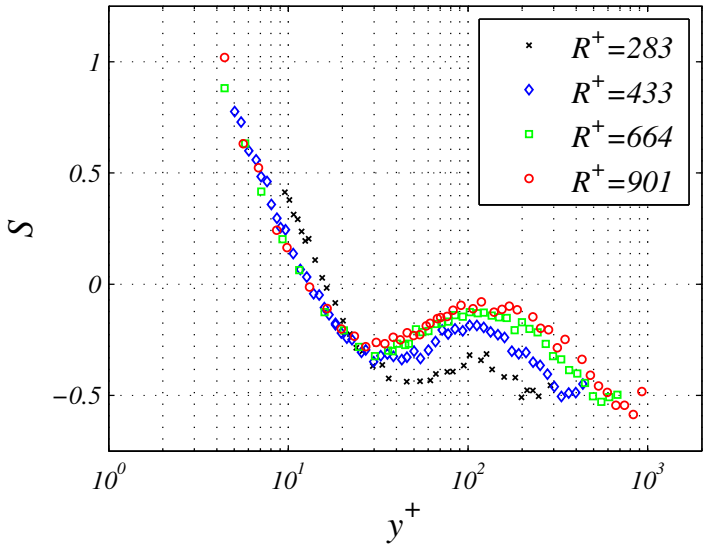

FIGURE A.14. Skewness values in inner scaling for different R^+ at fixed inner-scaled wire length, i.e. $L^+ \approx 15$.

Figure A.17 demonstrates the Reynolds number effects on the measured flatness values at the fixed inner-scaled wire length of $L^+ \approx 15$, and in addition the spatial resolution effects on the flatness profiles are also presented in figures A.18 and A.19 for R^+ equal to approximately 420 and 900 respectively.

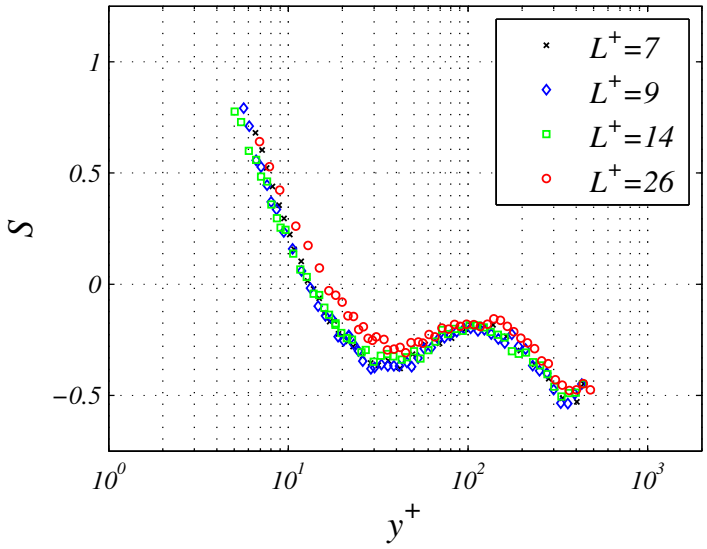

FIGURE A.15. Skewness values in inner scaling for different L^+ at $R^+ \approx 420$.

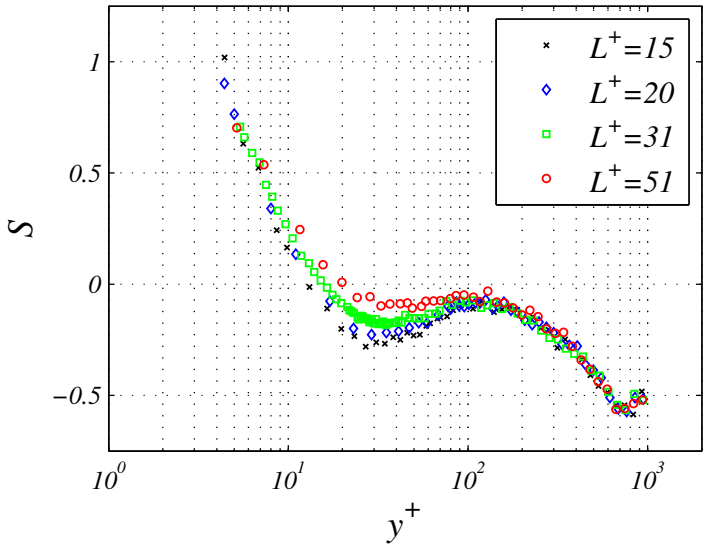

FIGURE A.16. Skewness values in inner scaling for different L^+ at $R^+ \approx 900$.

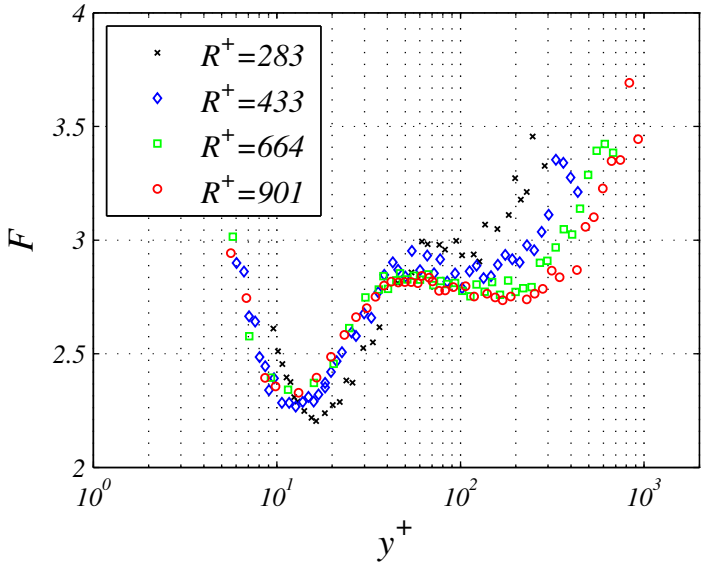

FIGURE A.17. Flatness values in inner scaling for different R^+ at fixed inner-scaled wire length, i.e. $L^+ \approx 15$.

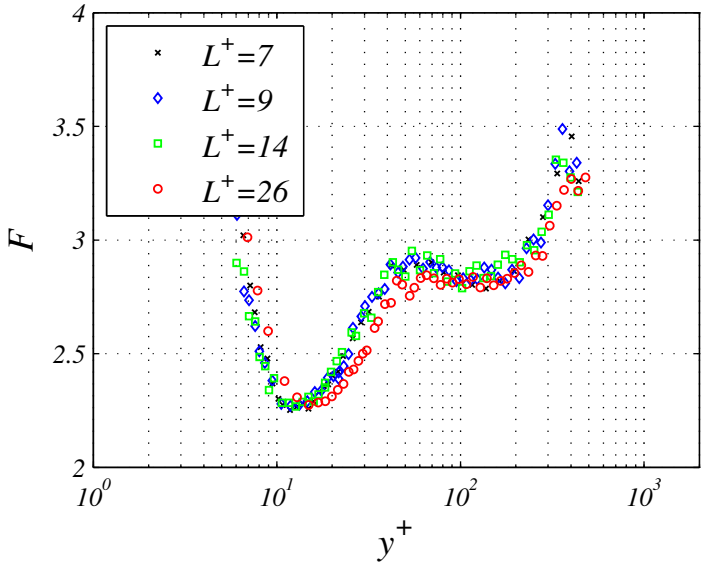

FIGURE A.18. Flatness values in inner scaling for different L^+ at $R^+ \approx 420$.

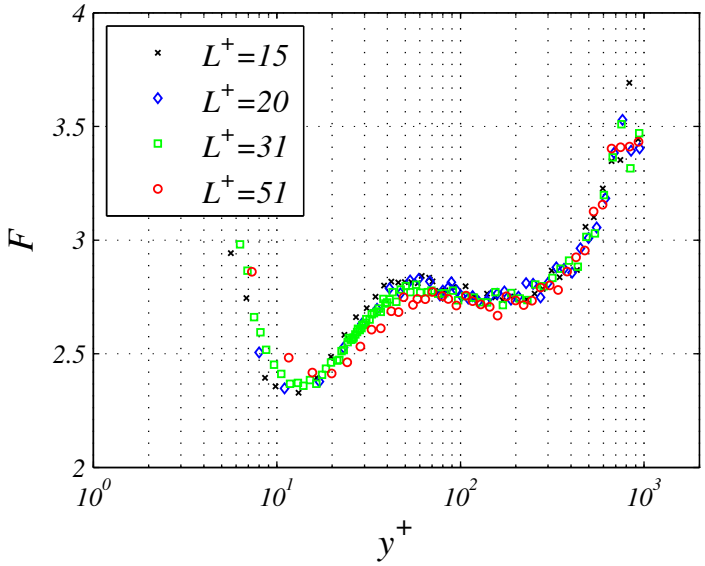

FIGURE A.19. Flatness values in inner scaling for different L^+ at $R^+ \approx 900$.

A.1.4. *Cumulative distribution function (CDF) maps*

Figure A.20 illustrates the maximum and the minimum of the velocity fluctuations (i.e. dashed lines), and also the contour plots of the cumulative distribution function (CDF) in the scaling of $U/U_\infty = (0.1 : 0.2 : 0.9)$ (i.e. solid lines) for different R^+ throughout the whole pipe radius. The Reynolds number dependancy of the velocity fluctuations are depicted in this figure (via. dashed lines) clearly for the whole pipe radius. For the results reported by Hultmark *et al.* (2010), the dashed lines in a similar plot are expected to merge in the inner region since the maximum r.m.s value in the inner region is not Reynolds number dependent according to their investigations. The observed Reynolds number dependancy in the present study is in agreement with the results reported by Alfredsson *et al.* (2011).

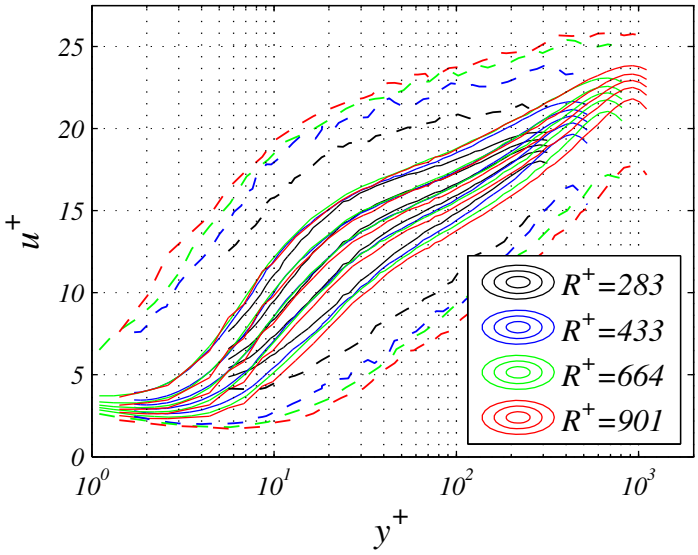

FIGURE A.20. Contours of Probability Density Function (PDF), dashed lines (i.e. the maximum and minimum of the velocity fluctuations), and Cumulative Distribution Function (CDF), solid lines, for different R^+.

The spatial resolution effects on the cumulative distribution function contour plots are depicted in figures A.21 and A.22. Note that the vertical axis, u^+, in figure A.22 is scaled logarithmically.

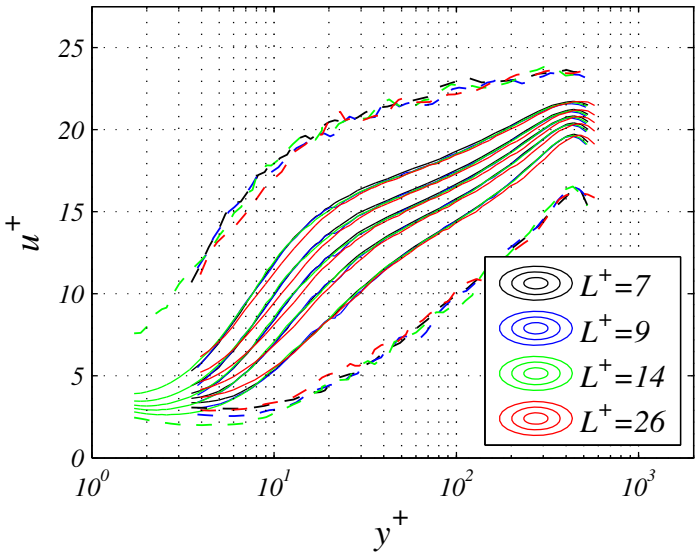

(a) at $R^+ \approx 420$.

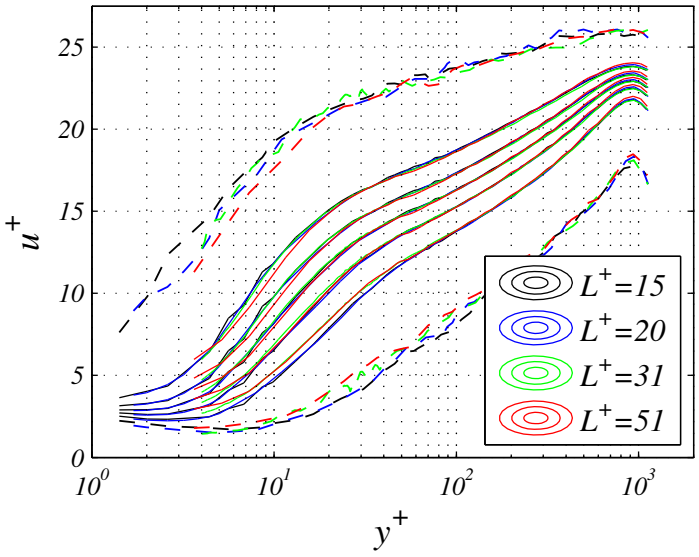

(b) at $R^+ \approx 900$.

FIGURE A.21. Contours of Probability Density Function (PDF), dashed lines (i.e. the maximum and minimum of the velocity fluctuations), and Cumulative Distribution Function (CDF), solid lines, for different L^+.

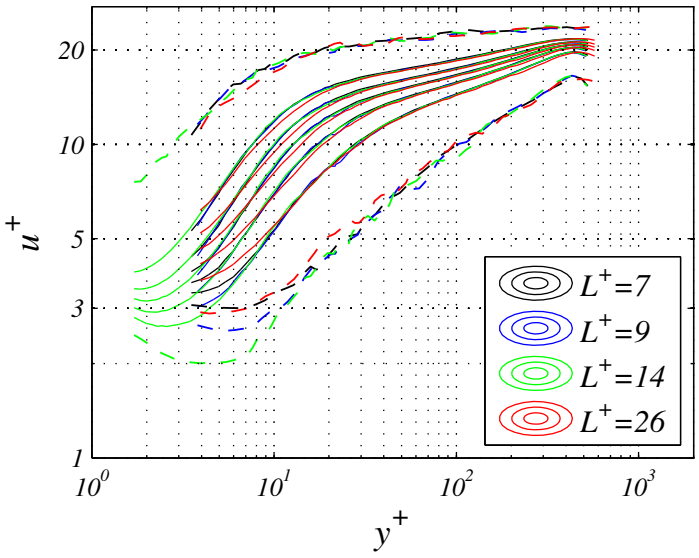

(a) at $R^+ \approx 420$.

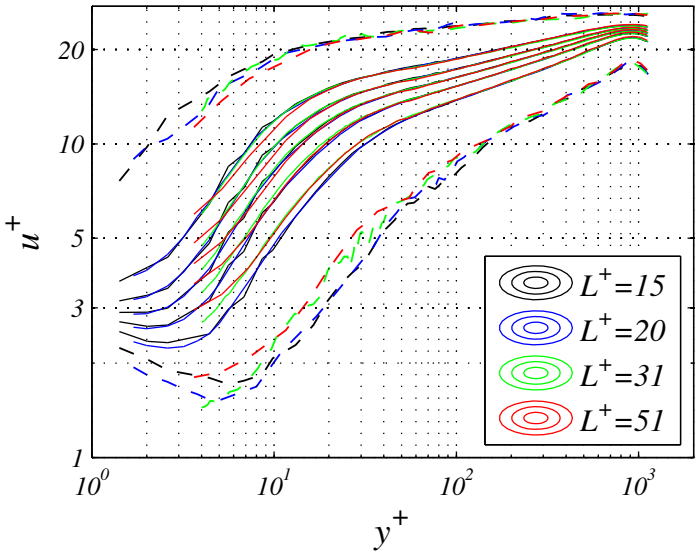

(b) at $R^+ \approx 900$.

FIGURE A.22. Contours of Probability Density Function (PDF), dashed lines (i.e. the maximum and minimum of the velocity fluctuations), and Cumulative Distribution Function (CDF), solid lines, for different L^+. The vertical axis is scaled logarithmically.

References

Alfredsson, P. H. & Örlü, R. 2010 The diagnostic plot a litmus test for wall bounded turbulence data. *European Journal of Mechanics - B/Fluids* .

Alfredsson, P. H. & Tillmark, N. 2005 *A beginers guide to fluid mechanics measurements*. Book manuscript.

Alfredsson, P. H., Örlü, R. & Schlatter, P. 2011 The viscous sublayer revisited-exploiting self-similarity to determine the wall position and friction velocity. *Experiments in Fluids* .

Anwer, M. & So, R. M. C. 1993 Swirling turbulent flow through a curved pipe. *Experiments in Fluids* **14**, 85–96.

Anwer, M., So, R. M. C. & Lai, Y. G. 1989 Perturbation by and recovery from bend curvature of a fully developed turbulent pipe flow. *Physics of Fluids* **1** (8).

Azzola, J., Humphrey, J. A. C., Iacovides, H. & Launder, B. E. 1986 Developing Turbulent Flow in a U-Bend of Circular Cross-Section: Measurement and Computation. *Journal of Fluid Mechanics* **108** (2), 214–221.

Benard, H. 1926 On the frequency law of alternate eddies behind an obstacle. *C.R. Acad. Sci.* **182**.

Berger, E. 1964 . *Z. Flugwiss* **12**, 41.

Berger, E. & Wille, R. 1972 Periodic Flow Phenomena. *Annual Review of Fluid Mechanics* **4**, 313–340.

Blasius, H. 1913 Das Ähnlichkeitsgesetz bei reibungsvorgängen in flüssigkeiten. *Mitt. Forschungsard* **131**.

Bruun, H. H. 1995 *Hot-wire anemometry: Principals and signal analysis.*. Oxford University Press Inc., New York, USA.

Chang, T. H. & Kim, H. Y. 2001 An investigation of swirling flow in a cylindrical tube. *Journal of Mechanical Science and Technology* **15** (12), 1892–1899.

Chang, T. H. & Lee, H. S. 2003 An Experimental Study on Swirling Flow in a 90 Degree Circular Tube by Using Particle Image Velocimetry. *Journal of Visualization* **6** (4), 343–352.

Dean, W. R. 1928 Fluid Motion in a Curved Channel. *Proceedings of the Royal Society of London. Series A, Containing Papers of a Mathematical and Physical Character* **121** (787), 402–420.

van Dijk, A. 1999 Aliasing in one-point turbulence measurements - Theory, DNS

and hotwire experiment. PhD thesis, Delft University of Technology, The Netherlands.

Eggels, J. G. M., Unger, A., Weiss, M. H., Westerweel, J., Adrian, R. J., Friedrich, R. & Nieuwstadt, F. T. M. 1994 Fully developed turbulent pipe flow: a comparison between direct numerical simulation and experiment. *Journal of Fluid Mechanics* **268**, 175–210.

Enayet, M. M., Gibson, M. M., Taylor, A. M. K. P. & Yianneskisa, M. 1982 Laser-Doppler measurements of laminar and turbulent flow in a pipe bend. *International Journal of Heat and Fluid Flow* **3** (4), 213–219.

Facciolo, L. 2006 A study on axially rotating pipe and swirling jet flows. PhD thesis, KTH Mechanics, Stockholm, Sweden.

Hultmark, M., Bailey, S. C. C. & Smits, A. J. 2010 Scaling of near-wall turbulence in pipe flow. *Journal of Fluid Mechanics* **649**, 103–113.

Imao, S., Motoyuki, I. & Takeyoshi, H. 1996 Turbulent characteristics of the flow in an axially rotating pipe. *International Journal of Heat and Fluid Flow* **17** (5), 444–451.

Johansson, A. V. & Alfredsson, P. H. 1982 On the structure of turbulent channel flow. *Journal of Fluid Mechanics* **122**, 295–314.

von Kárman, T. 1931 Mechanische Ähnlichkeit und turbulenz. In *AB Sveriges Lifografska Tryckenier*, , vol. 1, pp. 85–93.

Kikuyama, K., Murakami, M., Nishibori, K. & Maeda, K. 1983 Flow in an Axially Rotating Pipe : A calculation of flow in the saturated region. *Bulletin of JSME* **26**, 506–513.

King, L. V. 1914 On the Convection of Heat from Small Cylinders in a Stream of Fluid: Determination of the Convection Constants of Small Platinum Wires with Applications to Hot-Wire Anemometry. *Philosophical Transactions of the Royal Society of London. Series A, Containing Papers of a Mathematical or Physical Character* **214**, 373–432.

King, M. K., Rothfus, R. R. & Kermode, R. I. 1969 Static pressure and velocity profiles in swirling incompressible tube flow. *Journal of AICHE* **15** (6), 837–842.

Klewicki, J. C. & Falco, R. E. 1990 On accurately measuring statistics associated with small-scale structure in turbulent boundary layers using hot-wire probes. *Journal of Fluid Mechanics* **219**, 119–142.

Kohan, S. & Schwarz, W. H. 1973 Low speed calibration formula for vortex shedding from cylinders. *Physics of Fluids* **16** (9), 1528–9.

König, M., Eisenlohr, H. & Eckelmann, H. 1990 The fine structure in the StrouhalReynolds number relationship of the laminar wake of a circular cylinder. *Physics of Fluids* **2** (9), 1607–14.

Kundu, P. K. & Cohen, I. M. 2004 *Fluid Mechanics*, 3rd edn. Elsevier Academic Press.

Kurokawa, M., Cheng, K. C. & Shi, L. 1998 Flow visualization of relaminarization phenomena in curved pipes and the related measurements. *Journal of Visualization* **1** (1), 9–28.

Lanspeary, P. V. 1997 Establishing very low speed, disturbance-free flow for anemometry in turbulent boundary layers. PhD thesis, The University of Adelaide, Australia.

Lee, T. & Budwig, R. 1991 Two improved methods for low-speed hot-wire calibration. *Measurement Science and Technology* **2** (7), 643–646.

Lindgre, B. & Johansson, A. V. 2002 Evaluation of the Flow Quality in the MTL Wind-Tunnel. *Tech. Rep. TRITA-MEK 2002:13, KTH, Royal Institute of Technology, Stockholm, Sweden* .

Medwell, J. O., Chang, T. H. & Kown, S. S. 1989 A Study of Swirling Flow in a Cylindrical Tube. *Journal of SAREK* **4**, 256–275.

Millikan, C. B. 1938 A critical discussion of turbulent flows in channels and circular tubes. *International Congress of Applied Mechanics* **5**.

Monty, J. P., Stewart, J. A., Williams, R. C. & Chong, M. S. 2007 Large-scale features in turbulent pipe and channel flows. *J. Fluid Mech.* **589**, 147–156.

Murakami, M. & Kikuyana, K. 1980 Turbulent flow in axially rotating pipes. *Journal of Fluid Mechanics* **102** (1), 97–104.

Musker, A. J. 1979 Explicit expression for the smooth wall velocity distribution in a turbulent boundary layer. *AIAA Journal* **17**, 655–657.

Nagib, H. M. & Chauhan, K. A. 2008 Variations of von Kármán coefficient in canonical flows. *Physics of Fluids* **20**.

Norberg, C. 1994 An experimental investigation of the flow around a circular cylinder: influence of aspect ratio. *Journal of Fluid Mechanics* **258**, 287–316.

O'Neill, P. L., Nicolaides, D., Honnery, D. & Soria, J. 2004 Autocorrelation Functions and the Determination of Integral Length with Reference to Experimental and Numerical Data. *Australasian Fluid Mechanics Conference* **15**.

Örlü, R. 2006 Experimental studies in jet flows and zero pressure-gradient turbulent boundary layers. *Licentiate thesis, KTH Mechanics, Stockholm, Sweden* .

Örlü, R. 2009 Experimental studies in jet flows and zero pressure-gradient turbulent boundary layers. PhD thesis, KTH Mechanics, Stockholm, Sweden.

Örlü, R. & Alfredsson, P. H. 2010 On spatial resolution issues related to time-averaged quantities using hot-wire anemometry. *Experiments in Fluids* .

Örlü, R., Fransson, J. H. M. & Alfredsson, P. H. 2010 On near wall measurements of wall bounded flows-The necessity of an accurate determination of the wall position. *Progress in Aerospace Sciences* .

Örlü, R. & Schlatter, P. 2011 On the fluctuating wall-shear stress in zero pressure-gradient turbulent boundary layer flows. *Physics of Fluids* **23**.

Pope, S. B. 2000 *Turbulent flows*. Cambridge University Press, Cambridge, UK.

Prandtl, L. 1925 Report on investigation of developed turbulence. *NACA Report TM-1231* .

Pruvost, J., Legrand, J. & Legentilhomme 2004 Numerical Investigation of Bend and Torus Flows, Part I : Effect of Swirl Motion on Flow Structure in U-Bend. *Chemical Engineering Science* **59**, 3345–3357.

Rayleigh, L. 1896 *The theory of sound*, 3rd edn. MacMillan, London.

Reich, G. & Beer, H. 1989 Fluid flow and heat transfer in an axially rotating pipe–I. Effect of rotation on turbulent pipe flow. *International Journal of Heat and Mass Transfer* **32** (3), 551–562.

Roshko, A. 1954 On the Development of Turbulent Wakes from Vortex Streets. *NACA Report 1191 (formerly TN-2913)* .

Rowe, M. 1970 Measurements and computations of flow in pipe bends. *Journal of Fluid Mechanics* **43**, 771–783.

Shimizu, Y. & Sugino, K. 1980 Hydraulic Losses and Flow Patterns of a Swirling Flow in U-bends. *Bulletin of JSME* **23** (183), 1443–1450.

Strouhal, V. 1878 Ueber eine besondere Art der Tonerregung. *Ann. Phys. und Chemie* **241**, 216–251.

Sudo, K., Sumida, M. & Hibara, H. 1998 Experimental investigation on turbulent flow in a circular-sectioned 90-degree bend. *Experiments in Fluids* **25** (1), 42–49.

Sudo, K., Sumida, M. & Hibara, H. 2000 Experimental investigation on turbulent flow through a circular-sectioned 180 bend. *Experiments in Fluids* **28** (1), 51–57.

Tritton, D. J. 1959 Experiments on the flow past a circular cylinder at low Reynolds numbers. *Journal of Fluid Mechanics* **6** (4), 547–567.

Veenman, M. P. B. 2004 Statistical Analysis of Turbulent Pipe Flow: A Numerical Approach. PhD thesis, Eindhoven University Press. The Netherlands.

Wagner, C., Hüttl, T. J. & Friedrich, R. 2001 Low-Reynolds-number effects derived from direct numerical simulations of turbulent pipe flow. *Computers & Fluids* **30**, 581–590.

White, A. 1964 Flow of a fluid in an axially rotating pipe. *Journal of Mechanical Engineering Science* **6**, 47–52.

Williamson, C. H. K. 1988 Defining a universal and continuous Strouhal-Reynolds number relationship for the laminar vortex shedding of a circular cylinder. *Physics of Fluids* **31**, 2742–2745.

Williamson, C. H. K. 1989 Oblique and parallel modes of vortex shedding in the wake of a circular cylinder at low Reynolds numbers. *J. Fluid Mech.* **206**, 579–627.

Wu, X. & Moin, P. 2008 A direct numerical simulation study on the mean velocity characteristics in turbulent pipe flow. *Journal of Fluid Mechanics* **608**, 81–112.